

MASTER OF SCIENCE THESIS

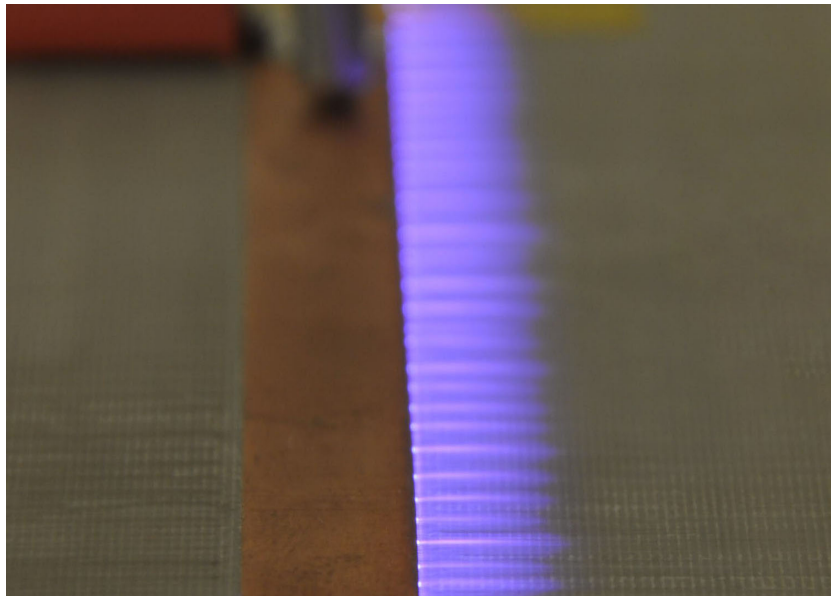
---

# Dielectric Barrier Discharge Plasma Actuators for Unsteady Aerodynamic Load Control

Robin Pul

---

October 31, 2013





# **Dielectric Barrier Discharge Plasma Actuators for Unsteady Aerodynamic Load Control**

MASTER OF SCIENCE THESIS

For obtaining the degree of Master of Science in Aerospace  
Engineering at Delft University of Technology

Robin Pul

October 31, 2013



Copyright © Aerospace Engineering, Delft University of Technology  
All rights reserved.

DELFT UNIVERSITY OF TECHNOLOGY  
DEPARTMENT OF  
AERODYNAMICS

The undersigned hereby certify that they have read and recommend to the Faculty of Aerospace Engineering for acceptance a thesis entitled “**Dielectric Barrier Discharge Plasma Actuators for Unsteady Aerodynamic Load Control**” by **Robin Pul** in fulfillment of the requirements for the degree of **Master of Science**.

Dated: October 31, 2013

Supervisor:

\_\_\_\_\_  
Prof.dr.ir. L.L.M. Veldhuis

Supervisor:

\_\_\_\_\_  
Dr.ir. M. Kotsonis

Reader:

\_\_\_\_\_  
Dr.ir. D. Ragni



---

# Preface

This thesis work is the last step towards graduation and finally becoming an aerospace engineer. Years of studying at the aerospace faculty passed by and I look back at an incredibly beautiful part of my life. The last year and a bit I had the privilege of working in the field of experimental aerodynamics, a long lasting dream that came true. I therefore would like to express my gratitude to those who helped me to reach the fulfilment of my thesis.

I would like to thank professor Leo Veldhuis for giving me the opportunity to perform the research on this interesting topic and for his insightful ideas regarding the problems encountered during the experiments. Furthermore, I am indebted to my daily supervisor Marios Kotsonis for his assistance and guidance during my thesis work and for answering all my questions during this process. His enthusiasm for research will instantly re-energize you when things are not going as planned and even a trip to the hospital won't discourage him from doing what he does, researching.

Many thanks to the technical staff of the Low Speed Laboratory and the staff at the Aerodynamics department. Special thanks go to Lee Molenwijk and Stefan Bernardy, for their assistance when I encountered any technical problems with the equipment and for their ideas in the design of the test set-ups.

In addition, I'd like to thank my fellow MSc students in the 'basement' for their interesting discussions and relaxing conversations during the lunch breaks.

I would like to thank all my friends that I met during my time in Delft. During these years we experienced some crazy stuff and the moments of distraction from my thesis are greatly appreciated. I hope that in the years to come we will encounter more of these moments together.

Last but not least I would like to thank my family for their encouragement and support during my entire study in Delft. Special thanks go to my girlfriend, for her endless support in good times and the bad.



---

# Abstract

Active load control for load alleviation has become more important in the wind energy industry in recent years. The continuously increasing size of wind turbines has eventually led to the point where efficient mitigation of the fatigue loads on the blades, due to unsteady wind or gusts, is becoming an important aspect in the design. Suppression of these unsteady loads by passive or active means would reduce the fatigue crack growth in the blade material and allow for thinner and cheaper blades.

An experimental study on the control of circulation around a modified symmetrical NACA64-2-A015 airfoil is presented. The modification implies the implementation of a rounded trailing edge on the airfoil. Circulation control is achieved by the use of Dielectric Barrier Discharge plasma actuators placed at the trailing edge of the airfoil. The body force acting on the flow, as produced by the plasma actuator is used to change the Kutta condition on the rounded trailing edge and with that the circulation and corresponding lift. Such a configuration reduces the weight and complexity issues typically associated with classical blowing circulation control concepts and many other concepts aiming at load control. A wind tunnel test campaign is performed in order to quantify the effect of the plasma actuators driven by the conventional sinusoidal high voltage signal. Direct aerodynamic force measurements are taken using sensitive load cells. Additionally a high speed 2-component Particle Image Velocimetry study is performed in the vicinity of the actuator in order to clarify the working principles of the concept. The effect of the plasma actuator position is investigated and compared to the well proven Gurney flap concept. Tested free stream velocities range from 10-20m/s at chord Reynolds number between  $1.5 \cdot 10^5$  and  $2.2 \cdot 10^5$  respectively.

Results indicate that the plasma actuator is indeed capable of changing the Kutta condition and therefore the circulation of the tested airfoil. Preliminary results indicate an average increase in lift coefficient of 0.1 for low Reynolds numbers. At high angles of attack the plasma actuators positioned on the lower side of the airfoil (pressure side) becomes more effective and changes up to  $\Delta c_l = 0.15$  were measured for an  $\alpha$  around  $8^\circ$ , corresponding to a 21% increase in  $c_l$ . The maximum lift augmentation coefficient corresponding to the maximum  $\Delta c_l$  was on average 110, for angles of attack close to stall and regardless of the Reynolds number. This means that the lift augmentations achieved are as high as 110 times the relative momentum input by the actuator itself. The best plasma actuator configuration is compared with the data obtained from Gurney flap experiments and the measured lift coefficient data at low Reynolds number suggests that at high pre-stall  $\alpha$  the plasma actuator can be compared to a Gurney flap with an effective height of  $h/c = 0.018$ . From the time-resolved Particle Image Velocimetry data it follows that the plasma

actuators interact with the vortex pair in the recirculation area behind the airfoil. The relative position of the actuator with respect to the rear stagnation point and the direction of the produced forcing on the flow are found to be important factors. The obtained wake deflection angles support the results from the force measurements and indicate that the Kutta condition is indeed altered, showing that the plasma actuator can be applied as load control device. Nevertheless, actuator upscaling is necessary for future applications.

---

# Contents

<b>Preface</b>	<b>v</b>
<b>Abstract</b>	<b>vii</b>
<b>List of Figures</b>	<b>xvii</b>
<b>List of Tables</b>	<b>xix</b>
<b>Nomenclature</b>	<b>xxi</b>
<b>1 Introduction</b>	<b>1</b>
1.1 Background and relevance . . . . .	1
1.2 Thesis objectives . . . . .	2
1.3 Outline of the thesis . . . . .	2
<b>2 Theory</b>	<b>5</b>
2.1 Active load control . . . . .	5
2.1.1 Active vs. passive control . . . . .	5
2.1.2 Classification . . . . .	6
2.1.3 Requirements . . . . .	8
2.2 Plasma actuators for load control . . . . .	9
2.2.1 Plasma . . . . .	9
2.2.2 Dielectric Barrier Discharge . . . . .	10
2.2.3 Plasma actuator physics . . . . .	10
2.2.4 Effect of actuator parameters . . . . .	14
2.2.5 Steady and unsteady actuation . . . . .	18
2.3 Plasma actuator applications . . . . .	18
2.3.1 Transition control . . . . .	19
2.3.2 Vortex shedding control . . . . .	19
2.3.3 Leading edge separation control . . . . .	20
2.3.4 Turbulent separation control . . . . .	22
2.3.5 DBD plasma actuators for load control . . . . .	25

<b>3</b>	<b>Measurement techniques</b>	<b>27</b>
3.1	Force sensors . . . . .	27
3.2	Particle image velocimetry . . . . .	28
3.2.1	Working principle . . . . .	28
3.2.2	Tracer particles . . . . .	29
3.2.3	Illumination . . . . .	33
3.2.4	Particle imaging . . . . .	33
3.2.5	Image analysis . . . . .	35
3.3	Power consumption . . . . .	38
3.3.1	Integrating capacitor method . . . . .	38
3.3.2	Data smoothing . . . . .	39
<b>4</b>	<b>Experimental set-up</b>	<b>41</b>
4.1	Model design . . . . .	41
4.2	Flow facility . . . . .	42
4.3	High voltage supply . . . . .	43
4.4	Force measurements . . . . .	43
4.4.1	Experimental set-up of the force balance . . . . .	43
4.4.2	Force calibration and calculation . . . . .	44
4.4.3	Wind tunnel corrections . . . . .	45
4.4.4	Experimental test matrix: Force . . . . .	47
4.5	Time-resolved PIV measurements . . . . .	51
4.5.1	Experimental set-up of the PIV . . . . .	52
4.5.2	Tracer particles and seeding generator . . . . .	52
4.5.3	Laser and laser sheet formation . . . . .	52
4.5.4	High-speed Camera . . . . .	53
4.5.5	Field of view . . . . .	53
4.5.6	PIV-software . . . . .	54
4.5.7	Image processing . . . . .	54
4.5.8	Experimental test matrix: PIV . . . . .	54
4.6	Power consumption measurements . . . . .	55
4.6.1	Oscilloscope and capacitor . . . . .	55
4.6.2	Experimental test matrix: Power consumption . . . . .	56
<b>5</b>	<b>Results</b>	<b>57</b>
5.1	Force measurements . . . . .	57
5.1.1	Rounded trailing edge model . . . . .	57
5.1.2	Gurney flap . . . . .	63
5.1.3	Trailing edge flap above chord line . . . . .	67
5.1.4	Trailing edge flap below chord line . . . . .	69
5.2	Lift augmentation . . . . .	70
5.3	PIV flow field measurements . . . . .	74
5.3.1	Mean velocity field . . . . .	74
5.3.2	Mean turbulent kinetic energy . . . . .	79
5.3.3	Mean Reynolds shear stress . . . . .	80
5.3.4	Wake analysis . . . . .	82
5.4	Power consumption . . . . .	85

---

<b>6</b>	<b>Conclusions and recommendations</b>	<b>89</b>
6.1	Conclusions . . . . .	89
6.2	Recommendations . . . . .	91
	<b>References</b>	<b>93</b>
<b>A</b>	<b>Electric field study</b>	<b>99</b>
<b>B</b>	<b>PIV data: more results</b>	<b>103</b>
<b>C</b>	<b>Wake details: more results</b>	<b>107</b>



---

# List of Figures

2.1	Aerodynamic effect of AFC devices on baseline lift curves: (a) lift/load control devices (b) flow separation control devices[5]. . . . .	7
2.2	Graph showing the benefits of using stall delay devices, based on[27]. . . . .	8
2.3	Schematic of a single DBD actuator[11]. . . . .	10
2.4	Schematic of the half-cycles. During the forward stroke the electrons emitted from the exposed electrode accumulate on the dielectric surface (on the left) and in the backward stroke return to the bare electrode (on the right)[17]. . . . .	11
2.5	Total discharge current and fast-imaging of the developing plasma layer for (top to bottom): sine, square, positive ramp, negative ramp waveforms (images are for a top view and opening gate of $100\mu\text{s}$ )[4]. . . . .	12
2.6	Actuated DBD plasma actuator showing the purple/blue glow[41]. . . . .	13
2.7	Evolution of the velocity and acceleration within the high voltage cycle for the a combined sine-square waveform (values probed at $x = 5\text{mm}$ , $y = 0.4\text{mm}$ from exposed electrode edge)[35]. . . . .	14
2.8	Schematic of a single DBD plasma actuator indicating the geometric parameters[11].	15
2.9	Asymptotic evolution of the maximum induced velocity with the grounded electrode width[20]. . . . .	15
2.10	Evolution of the maximum induced velocity with the electrode gap [20]. . . . .	15
2.11	Maximum extent of the plasma as function of $V_{app}$ [45]. . . . .	16
2.12	Maximum extent of the plasma as function of $f_{ac}$ [45]. . . . .	16
2.13	Typical velocity profiles measured with a glass Pitot tube for different voltages. ( $t = 4\text{mm}$ glass dielectric, $g = w_c = 5\text{mm}$ and $f_{ac} = 300\text{Hz}$ )[41]. . . . .	17
2.14	Maximum velocity induced in air by actuator approximately proportional to $V_{app}^{7/2}$ (triangular waveform, $f_{ac} = 5\text{kHz}$ )[17]. . . . .	17
2.15	Steady and unsteady actuation[60]. . . . .	18
2.16	Schematic of the test setup showing the effect of plasma actuator on the point of transition[21]. . . . .	19
2.17	Smoke flow visualization images with (a) plasma actuators off and (b) plasma actuators on (steady actuation)[60]. . . . .	20

2.18	Flow visualization of NACA-0015 airfoil at $\alpha = 12^\circ$ (a) with flow separation and (b) with flow re-attachment for $V_{app} = 10\text{kV}$ , $f_{ac} = 4.2\text{kHz}$ [50]. . . . .	21
2.19	(a) Lift coefficient versus angle of attack and (b) drag polar for airfoil at 21m/s with plasma actuator off (squares), and in steady (circles) and unsteady $f_p = 166\text{Hz}$ (triangles) operation[12]. . . . .	22
2.20	Schematic of the experimental setup for turbulent boundary layer measurements[23].	23
2.21	Schematics of (a) spanwise and (b) streamwise plasma actuators[23]. . . . .	24
2.22	Sketch for the jet CC airfoil (a) and the PCC airfoil (b)[66]. . . . .	24
3.1	An image of the KD40s force sensor. . . . .	27
3.2	Schematic overview of a planer PIV process. . . . .	29
3.3	The relative particle motion, from Melling[40]. . . . .	30
3.4	Electric potential distribution of the plasma actuator gap at the trailing edge and the maximum applied peak-to-peak voltage of 35kV. . . . .	31
3.5	Electric field strength of the plasma actuator gap at the trailing edge and the maximum applied peak-to-peak voltage of 35kV. . . . .	31
3.6	Scattered light intensity as a function of the scattering angle for a $1\mu\text{m}$ oil droplet.	32
3.7	Light sheet formation optics:a) side view showing the expansion of the laser beam and b) top view showing beam focus at measurement location[54]. . . . .	33
3.8	Airy diffraction pattern from a $1\mu\text{m}$ diameter particle, figure taken from Scarano[54].	34
3.9	PIV acquisition modes: a) single frame b) double frame, figure from Raffel[48] . .	36
3.10	Image interrogation windows and cross-correlation map, figure from Scarano[54] . .	37
3.11	Electric circuit diagram of the monitor capacitor method. . . . .	38
3.12	Overview of the smoothing algorithm . . . . .	40
4.1	Modified NACA64-2-A015 airfoil with a circular trailing edge. . . . .	41
4.2	Overview of the V-tunnel: 1) measuring room, 2) fan room, 3) fan, 4) settling chamber, 5) & 6) spike, 7) contraction, 8) sound damper. . . . .	42
4.3	A schematic view of the force balance set-up . . . . .	43
4.4	A schematic free body diagram of the test set-up used. . . . .	44
4.5	A schematic free body diagram of the test set-up used. . . . .	45
4.6	Airfoil and vortex image system used for derivation of 2D open jet streamline curvature correction . . . . .	47
4.7	Schematic view of the method used to determine the change in coefficients . . . . .	48
4.8	Geometric parameters that define the location of the plasma actuator electrodes. . .	49
4.9	Plasma actuator gap position for all tested configurations. . . . .	49
4.10	Schematic view of the two tested Gurney flap types. . . . .	50
4.11	Schematic representation of the flap position with respect to the main airfoil: a) flap above chord line, b) flap below the chord line. . . . .	51
4.12	A schematic view of the PIV test set-up. . . . .	53
4.13	Photograph of the laser sheet optics used in the experiment. . . . .	54
5.1	Variation of lift coefficient against carrier frequency for varying Reynolds number and angle of attack, plasma actuator position C. . . . .	58

5.2	Variation of lift coefficient against applied peak-to-peak voltage for varying Reynolds number and angle of attack, plasma actuator position C. . . . .	59
5.3	Plasma actuator gap position for all tested configurations. Copied from chapter 4. . . . .	59
5.4	Variation of lift coefficient against angle of attack for varying Reynolds number and all plasma actuator gap positions. . . . .	60
5.5	The change in lift coefficient against angle of attack for varying Reynolds number and all plasma actuator gap positions. . . . .	60
5.6	Variation of drag coefficient against angle of attack for varying Reynolds number and all plasma actuator gap positions. . . . .	61
5.7	Change in drag coefficient against angle of attack for varying Reynolds number and all plasma actuator gap positions. . . . .	61
5.8	Lift against drag coefficient for varying Reynolds number and all plasma actuator gap positions. . . . .	62
5.9	Change in lift coefficient against Reynolds number for three small angles of attack and all plasma actuator gap positions. . . . .	62
5.10	Change in lift coefficient against Reynolds number for three angles of attack near stall and all plasma actuator gap positions. . . . .	63
5.11	Schematic view of the two tested Gurney flap types. Copied from chapter 4. . . . .	63
5.12	Variation of lift coefficient against angle of attack for varying Reynolds number and all Gurney flap configurations + plasma actuator position D . . . . .	64
5.13	Change in lift coefficient against angle of attack for varying Reynolds number and all Gurney flap configurations + plasma actuator position D . . . . .	64
5.14	Variation of drag coefficient against angle of attack for varying Reynolds number and all Gurney flap configurations + plasma actuator position D . . . . .	65
5.15	Change in drag coefficient against angle of attack for varying Reynolds number and all Gurney flap configurations + plasma actuator position D . . . . .	66
5.16	Lift against drag coefficient for varying Reynolds numbers and all Gurney flap configurations + plasma actuator position D . . . . .	66
5.17	Change in lift coefficient against Reynolds number for three small angles of attack and Gurney flap configurations + plasma actuator position D. . . . .	67
5.18	Change in lift coefficient against Reynolds number for three angles of attack near stall and all Gurney flap configurations + plasma actuator position D. . . . .	67
5.19	Schematic representation of the flap position with respect to the main airfoil: a) flap above chord line, b) flap below the chord line. Copied from chapter 4. . . . .	68
5.20	Change in lift coefficient against carrier frequency for different angles of attack and Reynolds numbers (flap above chord line) . . . . .	68
5.21	Change in drag coefficient against carrier frequency for different angles of attack and Reynolds numbers (flap above chord line) . . . . .	69
5.22	Change in lift coefficient against carrier frequency for different angles of attack and Reynolds numbers (flap below chord line) . . . . .	70
5.23	Change in drag coefficient against carrier frequency for different angles of attack and Reynolds numbers (flap above chord line) . . . . .	70
5.24	Mean velocity fields induced by plasma actuators C and D at an angle of attack of $0^\circ$ and quiescent flow conditions. The + indicates the actuator gap position. The velocity is in m/s. . . . .	71
5.25	Mean velocity fields induced by plasma actuators C and D at an angle of attack of $7^\circ$ and quiescent flow conditions. The + indicates the actuator gap position. The velocity is in m/s. . . . .	71

5.26	Mean velocity fields produced by plasma actuators C and D (on and off) at an angle of attack of $0^\circ$ and Reynolds number $1.46 \cdot 10^5$ . The + indicates the actuator gap position, the x indicates the location of the saddle point. The velocity is in m/s.	75
5.27	Mean velocity fields produced by plasma actuators C and D (on and off) at an angle of attack of $7^\circ$ and Reynolds number $1.46 \cdot 10^5$ . The + indicates the actuator gap position, the x indicates the location of the saddle point. The velocity is in m/s.	75
5.28	Turbulent kinetic energy fields produced by plasma actuators C and D (on and off) at an angle of attack of $0^\circ$ and Reynolds number $1.46 \cdot 10^5$ . The + indicates the actuator gap position. Turbulent kinetic energy in $0.5(\overline{u'_x u'_x} + \overline{u'_y u'_y})/U_\infty^2$ .	79
5.29	Turbulent kinetic energy fields produced by plasma actuators C and D (on and off) at an angle of attack of $7^\circ$ and Reynolds number $1.46 \cdot 10^5$ . The + indicates the actuator gap position. Turbulent kinetic energy in $0.5(\overline{u'_x u'_x} + \overline{u'_y u'_y})/U_\infty^2$ .	80
5.30	Average Reynolds stress fields produced by plasma actuators C and D (on and off) at an angle of attack of $0^\circ$ and Reynolds number $1.46 \cdot 10^5$ . The + indicates the actuator gap position. Average Reynolds shear stress fields in $\overline{\rho u'_x u'_y}/U_\infty^2$ .	81
5.31	Average Reynolds stress fields produced by plasma actuators C and D (on and off) at an angle of attack of $7^\circ$ and Reynolds number $1.46 \cdot 10^5$ . The + indicates the actuator gap position. Average Reynolds shear stress fields in $\overline{\rho u'_x u'_y}/U_\infty^2$ .	81
5.32	Vertical distribution of the time-averaged streamwise velocity component ( $u_x$ ) produced by plasma actuators C and D (on and off) at an angle of attack of $0^\circ$ and Reynolds number $1.46 \cdot 10^5$ .	82
5.33	Vertical distribution of the time-averaged streamwise velocity component ( $u_x$ ) produced by plasma actuators C and D (on and off) at an angle of attack of $7^\circ$ and Reynolds number $1.46 \cdot 10^5$ .	83
5.34	Location of the maximum streamwise velocity deficit in the wake as produced by plasma actuators C and D (on and off) at an angle of attack of $0^\circ$ and Reynolds number $1.46 \cdot 10^5$ .	83
5.35	Location of the maximum streamwise velocity deficit in the wake as produced by plasma actuators C and D (on and off) at an angle of attack of $7^\circ$ and Reynolds number $1.46 \cdot 10^5$ .	84
5.36	Streamwise distribution of the wake half-width as produced by plasma actuators C and D (on and off) at an angle of attack of $0^\circ$ and Reynolds number $1.46 \cdot 10^5$ .	84
5.37	Streamwise distribution of the wake half-width as produced by plasma actuators C and D (on and off) at an angle of attack of $7^\circ$ and Reynolds number $1.46 \cdot 10^5$ .	85
5.38	Figures with signals of the measured voltage over the capacitor and the applied voltage over the electrodes of the plasma actuator and the corresponding Lissajous curves and the calculated power consumption for: a-b) $f_{ac}=1000\text{Hz}$ and $V_{app}=35\text{kV}$ , c-d) $f_{ac}=1500\text{Hz}$ and $V_{app}=25\text{kV}$ , e-f) $f_{ac}=1000\text{Hz}$ and $V_{app}=25\text{kV}$ , g-h) $f_{ac}=1000\text{Hz}$ and $V_{app}=25\text{kV}$ ,	86
5.39	Measured power consumption against actuation frequency, $f_{ac}$ , and the applied peak-to-peak voltage, $V_{app}$ .	87
A.1	Plasma actuator configuration, domain and boundary conditions for determination of the electric field.	100
A.2	Electric potential distribution of the plasma actuator with gap at position C for maximum applied peak-to-peak voltage of 35kV. Contour lines show constant electric potential lines.	101
A.3	Electric field strength of the plasma actuator with gap at position C for the maximum applied peak-to-peak voltage of 35kV. Contour lines show electric field strength varying from $5 \cdot 10^5$ to $2 \cdot 10^7 \text{V/m}$ in steps of $5 \cdot 10^5 \text{V/m}$	102

B.1	Mean velocity fields produced by plasma actuators C and D (on and off) at an angle of attack of $0^\circ$ and Reynolds number $2.19 \cdot 10^5$ . The + indicates the actuator gap position, the x indicates the location of the saddle point. The velocity is in m/s.	104
B.2	Mean velocity fields produced by plasma actuators C and D (on and off) at an angle of attack of $7^\circ$ and Reynolds number $2.19 \cdot 10^5$ . The + indicates the actuator gap position, the x indicates the location of the saddle point. The velocity is in m/s.	104
B.3	Turbulent kinetic energy fields produced by plasma actuators C and D (on and off) at an angle of attack of $0^\circ$ and Reynolds number $2.19 \cdot 10^5$ . The + indicates the actuator gap position. Turbulent kinetic energy in $0.5(\overline{u'_x u'_x} + \overline{u'_y u'_y})/U_\infty^2$	105
B.4	Turbulent kinetic energy fields produced by plasma actuators C and D (on and off) at an angle of attack of $7^\circ$ and Reynolds number $2.19 \cdot 10^5$ . The + indicates the actuator gap position. Turbulent kinetic energy in $0.5(\overline{u'_x u'_x} + \overline{u'_y u'_y})/U_\infty^2$	105
B.5	Average Reynolds stress fields produced by plasma actuators C and D (on and off) at an angle of attack of $0^\circ$ and Reynolds number $2.19 \cdot 10^5$ . The + indicates the actuator gap position. Average Reynolds shear stress fields in $\overline{\rho u'_x u'_y}/U_\infty^2$	106
B.6	Average Reynolds stress fields produced by plasma actuators C and D (on and off) at an angle of attack of $7^\circ$ and Reynolds number $2.19 \cdot 10^5$ . The + indicates the actuator gap position. Average Reynolds shear stress fields in $\overline{\rho u'_x u'_y}/U_\infty^2$	106
C.1	Vertical distribution of the time-averaged streamwise velocity component ( $u_x$ ) produced by plasma actuators C and D (on and off) at an angle of attack of $0^\circ$ and Reynolds number $2.19 \cdot 10^5$	108
C.2	Vertical distribution of the time-averaged streamwise velocity component ( $u_x$ ) produced by plasma actuators C and D (on and off) at an angle of attack of $7^\circ$ and Reynolds number $2.19 \cdot 10^5$	108
C.3	Location of the maximum streamwise velocity deficit in the wake as produced by plasma actuators C and D (on and off) at an angle of attack of $0^\circ$ and Reynolds number $2.19 \cdot 10^5$	108
C.4	Location of the maximum streamwise velocity deficit in the wake as produced by plasma actuators C and D (on and off) at an angle of attack of $7^\circ$ and Reynolds number $2.19 \cdot 10^5$	109
C.5	Streamwise distribution of the wake half-width as produced by plasma actuators C and D (on and off) at an angle of attack of $0^\circ$ and Reynolds number $2.19 \cdot 10^5$	109
C.6	Streamwise distribution of the wake half-width as produced by plasma actuators C and D (on and off) at an angle of attack of $7^\circ$ and Reynolds number $2.19 \cdot 10^5$	109



---

# List of Tables

4.1	Parameters used during the investigation on the effect of plasma actuator settings, for the actuator with the gap at position C . . . . .	48
4.2	Approximate values of the geometric parameters describing the electrode locations for all plasma actuators gap positions used. . . . .	49
4.3	Parameters used during the investigation on the effect of the plasma actuator position . . . . .	50
4.4	Parameters used during the investigation on the Gurney flaps . . . . .	51
4.5	Parameters used during the investigation on the effect of the flaps . . . . .	52
4.6	Constant recording parameters of the PIV set-up . . . . .	55
4.7	Parameters of the PIV set-up . . . . .	55
4.8	Parameters used during the investigation on the power consumption, for the actuator with the gap at position C . . . . .	56
5.1	Maximum and minimum $\Delta c_l$ and corresponding lift augmentation values at an angle of attack of approximately zero. . . . .	73
5.2	Maximum and minimum obtained $\Delta c_l$ and corresponding lift augmentation in the range of angle of attack where no stall occurs. . . . .	74
5.3	Maximum and minimum obtained average $\Delta c_l$ and corresponding lift augmentation values in the range of angle of attack where no stall occurs. . . . .	74
5.4	Table showing the coordinates of the saddle points, normalized by the airfoil chord length, and the difference between actuator on and off for both plasma actuators and both angles of attack and Reynolds numbers. . . . .	76
5.5	An overview of the calculated wake deflections $\theta_w$ for plasma off and on and the corresponding change $\Delta\theta_w$ , the angle is in degrees. Added are the $\Delta c_l$ values obtained by force measurements, extracted from figure 5.5. . . . .	84



---

# Nomenclature

## Latin Symbols

$A$	aspect ratio	[–]
$A_i$	weighting coefficients or convolution integers	[–]
$a_0$	lift curve slope of a 2D airfoil section	[–]
$b$	airfoil span	[ $m$ ]
$b$	wing span	[ $m$ ]
$b_e$	effective plasma actuator width	[ $m$ ]
$b_{1/2}$	wake half-width	[ $m$ ]
$C_L$	blade lift coefficient	[–]
$C_m$	capacitor capacitance	[ $F$ ]
$C_\mu$	blowing momentum coefficient	[–]
$c$	section chord length	[ $m$ ]
$c_d$	section drag coefficient	[–]
$c_{d,t}$	measured section drag coefficient	[–]
$c_l$	section lift coefficient	[–]
$c_{lmax}$	maximum section lift coefficient	[–]
$c_{l,t}$	measured section lift coefficient	[–]
$c_{mc/4}$	section pitching moment at $c/4$	[–]
$c_{mc/4,t}$	measured section pitching moment at $c/4$	[–]
$D$	length separated flow region	[ $m$ ]
$D$	aperture diameter	[ $m$ ]
$D$	drag force	[ $N$ ]
$d$	downstream distance from nozzle	[ $m$ ]
$d_{blur}$	defocused particle size	[ $m$ ]
$d_{diff}$	diffracted particle size	[ $m$ ]

$d_i$	image distance	[m]
$d_o$	object distance	[m]
$d_p$	particle diameter	[m]
$E$	dielectric strength	[V/m]
$E_0$	electric field strength	[V/m]
$E_b$	breakdown electric field	[V/m]
$e$	Oswald efficiency number	[-]
$F_{el}$	electrostatic force	[N]
$F_f$	resistance of fluid to particle acceleration	[N]
$F_p$	pressure gradient force	[N]
$F_{st}$	viscous drag by Stokes law	[N]
$F_u$	drag force of unsteady motion	[N]
$f_2$	focal length of lens 2	[m]
$f$	focal length	[m]
$f_{ac}$	actuation frequency	[Hz]
$f_p$	pulse frequency	[Hz]
$f^+$	reduced frequency	[Hz]
$f_{\#}$	aperture	[-]
$g$	electrode gap	[m]
$H1$	output horizontal force sensor 1	[N]
$h$	nozzle width	[m]
$I_a$	current through the actuator	[A]
$I_m$	current through the capacitor	[A]
$L$	distance between lens and object	[m]
$L$	lift force	[N]
$M$	image magnification	[-]
$M$	pitching moment	[Nm]
$M_{c/4}$	pitching moment at $c/4$	[Nm]
$M'_{c/4}$	corrected pitching moment at $c/4$	[Nm]
$\bar{n}$	wall normal unit vector	[-]
$n$	number of cycles	[-]
$o_c$	covered electrode offset	[m]
$o_e$	exposed electrode offset	[m]
$P$	measured power consumption	[W/m]
$p$	pressure	[Pa]
$q_{\infty}$	free stream dynamic pressure	[N/m <sup>2</sup> ]
$Q_m$	charge on the capacitor	[C]
$q_n$	net charge	[C]
$Re$	Reynolds number	[-]
$Re_{xy}$	Reynolds shear stress component	[m <sup>2</sup> /s <sup>2</sup> ]
$R_{II}$	cross-correlation coefficient	[-]
$r_{lx}$	normalized x-coordinate of saddle point	[-]
$r_{ly}$	normalized y-coordinate of saddle point	[-]

$S$	wing area	$[m^2]$
$St_D$	Strouhal number based on length D	$[-]$
$s$	length of plasma jet parallel to airfoil surface	$[m]$
$\bar{T}$	integrated thrust force	$[-]$
$T$	thrust force	$[N]$
$T$	time period	$[s]$
$T_1$	time period for pulse frequency	$[s]$
$T_2$	time period active actuator	$[s]$
$T_m$	thrust per unit span	$[N/m]$
$T^p$	thrust component due to plasma forcing	$[N]$
$T^s$	thrust component due to shear and pressure	$[N]$
$T_x$	thrust component in x-direction	$[N]$
$T_y$	thrust component in y-direction	$[N]$
$t$	height of plasma jet perpendicular to airfoil surface	$[m]$
$t_d$	dielectric thickness	$[m]$
$t_e$	exposed electrode thickness	$[m]$
$\bar{U}_f$	fluid velocity vector	$[m/s]$
$U_p$	particle velocity	$[m/s]$
$U_\infty$	free stream velocity	$[m]$
$\bar{u}_i$	mean component of the velocity	$[m/s]$
$u'_i$	fluctuating component of the velocity	$[m/s]$
$u_{min}$	maximum velocity deficit or minimum velocity in the wake	$[m/s]$
$u_x$	velocity component in x-direction	$[m/s]$
$u_y$	velocity component in y-direction	$[m/s]$
$u_{  }$	velocity parallel to integration surface	$[m/s]$
$u_{\perp}$	velocity perpendicular to integration surface	$[m/s]$
$V1$	output vertical force sensor 1	$[N]$
$V2$	output vertical force sensor 2	$[N]$
$V3$	output vertical force sensor 3	$[N]$
$V_a$	voltage across the plasma actuator electrodes	$[V]$
$V_{app}$	applied peak-to-peak voltage	$[V]$
$V_m$	voltage across the capacitor	$[V]$
$\hat{V}$	slipping velocity vector	$[m/s]$
$w_c$	covered electrode width	$[m]$
$w_e$	exposed electrode width	$[m]$
$(y_k)_s$	smoothed data point value	$[-]$

## Greek Symbols

$\alpha$	angle of attack	$[^\circ]$
$\alpha_t$	measured angle of attack	$[^\circ]$
$\Gamma$	circulation	$[m^2/s]$

$\Delta$	symbol indicating a change w.r.t. reference value	[–]
$\delta_z$	depth of focus	[m]
$\epsilon_0$	permittivity of vacuum	[F/m]
$\epsilon_r$	dielectric constant/relative permittivity	[–]
$\theta_w$	deflection angle of the wake	[°]
$\lambda$	wavelength	[m]
$\mu$	mean	[–]
$\mu$	dynamic viscosity	[kg/m/s]
$\rho_p$	particle material density	[kg/m <sup>3</sup> ]
$\sigma$	standard deviation	[–]
$\sigma$	wind tunnel correction factor	[–]
$\phi$	electric potential	[V]

## Abbreviations

<b>AC</b>	Alternating Current
<b>AFC</b>	Active Flow Control
<b>APS</b>	Active Pixel Sensor
<b>CCD</b>	Charge Couple Device
<b>CMOS</b>	Complementary Metal Oxide Semiconductor
<b>DAQ</b>	Data Acquisition
<b>DBD</b>	Dielectric Barrier Discharge
<b>DC</b>	Duty Cycle
<b>FBD</b>	Free Body Diagram
<b>FOV</b>	Field Of View
<b>HWA</b>	Hot Wire Anemometry
<b>IW</b>	Interrogation Window
<b>LabVIEW</b>	Laboratory Virtual Instrument Engineering Workbench
<b>LDA</b>	Laser Doppler Anemometry
<b>LDV</b>	Laser Doppler Velocimetry
<b>LE</b>	Leading Edge
<b>MATLAB</b>	MATrix LABoratory
<b>MC</b>	Mid Chord
<b>NACA</b>	National Advisory Committee for Aeronautics
<b>Nd:YLF</b>	Neodymium-doped Yttrium Lithium Fluoride
<b>NI</b>	National Instruments
<b>PA</b>	Plasma Actuators
<b>PCC</b>	Plasma Circulation Control
<b>PIV</b>	Particle Image Velocimetry
<b>PMMA</b>	PolyMethylMethAcrylaat (Plexiglas)
<b>PMT</b>	Photo Multiplier Tube
<b>POM</b>	Polyoxymethylene

<b>PSVG</b>	Plasma Streamwise Vortex Generators
<b>RANS</b>	Reynolds-Averaged Navier-Stokes
<b>TE</b>	Trailing Edge
<b>TR-PIV</b>	Time Resolved Particle Image Velocimetry
<b>TS</b>	Tollmien-Schlichting
<b>UAV</b>	Unmanned Aerial Vehicles
<b>US</b>	United States



---

# Chapter 1

---

## Introduction

This experimental research work attempts to address a potential application of the Dielectric Barrier Discharge (DBD) plasma actuator. More specifically, the DBD plasma actuator is examined for its use in active load control. This introductory chapter will give a brief overview of the background and relevance of the topic and working principle of this concept. Additionally, it will enlighten the main aspects of this study and present the general outline of the thesis.

### 1.1 Background and relevance

Active load control for load alleviation has become more important in the wind energy industry in recent years. The continuously increasing size of wind turbines has eventually led to the point where efficient mitigation of the fatigue loads on the blades, due to unsteady wind or gusts, is becoming an important aspect in the design. Suppression of these unsteady loads by passive or active means would reduce the fatigue crack growth in the blade material and allow for thinner and cheaper blades.

Active flow control involves the control of local airflow around a lift generating body in order to achieve variations in the aerodynamic force components. In active load control the emphasis is put on the lift force. Ideally, the control and the produced change in lift needs to be applied with short response times, corresponding to the unsteady atmospheric conditions such as wind gusts. Many studies have been performed on concepts of active load control, including morphing trailing edge flaps[34], microtabs[42], microjets[6] and classical circulation control with slot blowing[61].

It is clear from the already published studies that an ideal actuator for aerodynamic load control combines efficient operation with robustness, mechanical reliability (no moving parts), low mass, compactness, low power consumption and a fast response time. A recent technology that seems to combine these properties is the plasma actuator. There are several implementations of the actuators, all based on the same physical principle. The most popular being the Dielectric Barrier Discharge type of actuator. These are based on the ionization of air via an alternating current (AC) high voltage signal. The typical configuration consists of two electrodes, one being grounded and one that carries the high voltage signal. The two electrodes are separated by a dielectric material which prohibits arc forming and allows the ionized gasses to accumulated on

the dielectric surface. The mechanism of the interaction between the weakly ionized air, accelerated by the strong electric field, and the neutral air is dominated by collisions between the heavy plasma species (mostly ions) and neutral air. This collisional behaviour is responsible for the net momentum transfer. In a macroscopic scale, usually the scale of the flow to be controlled, the model of a body force on the fluid seems to describe the effect reasonably. This body force can be translated to the production of a tangential wall jet of several m/s.

DBD plasma actuators have already been successfully applied for a wide variety of flow control applications, such as transition delay[21], lift enhancement on airfoils[12], turbulent skin-friction drag reduction[23], near-wake flow control[39], landing gear noise reduction[60] and have also proven to be effective in boundary layer separation control in low and moderate high Reynolds number flows[50, 47, 12].

Fewer studies have focussed on load control using plasma actuators. A recent study by Zhang et al.[66] involved the numerical simulation of plasma circulation control airfoil. The tangential jet blowing mechanism from classical circulation control was directly replaced by a plasma actuator while the geometry of the airfoil stayed the same. Results indicated an increase in lift coefficient up to 1.35. A second study has been published by Feng et al.[18], where a NACA0012 airfoil equipped with a Gurney flap is carrying an additional plasma actuator on the rear side of the flap with the plasma jet directed downwards. It was experimentally shown that the plasma actuator can further augment the lift enhancement capabilities of the Gurney flap, albeit for low Reynolds numbers.

## 1.2 Thesis objectives

In this thesis an experimental investigation on the use of plasma actuators for circulation control is presented. The actuators are placed on a specially modified symmetric airfoil with a rounded trailing edge. The idea behind this approach comes from the already discovered abilities of the plasma actuator. By the use of its discovered forcing on the flow, the actuator is expected to displace the stagnation point (Kutta condition), which is possible on a rounded trailing edge (fixed on a sharp trailing edge). This is similar to classical circulation control with slot blowing. Displacement of the stagnation point to the suction side of the airfoil (up) produces a decrease in lift, while displacement to the pressure side (down) produces an increase in lift. This principle, coupled with the proven fast response time of the plasma actuator could potentially lead to an efficient and robust system of active load control. This thesis includes a fundamental study on the feasibility of the plasma actuator for circulation control. The actuator is operated in continuous mode and the effect on the lift is directly measured with a force balance. Additionally, a parametric study on several actuator related properties is performed, focussing on the goal to maximize the change in lift. A flowfield study based on Particle Image Velocimetry (PIV) is performed in order to visualize and explain the fundamental features of the physical mechanisms present when the plasma actuator interacts with the flowfield.

## 1.3 Outline of the thesis

The structure of this thesis will be as follows. In chapter two the theory on active load control, the working principle of the DBD plasma actuator and the applications of flow control with plasma actuators will be discussed in more detail. The measurement techniques used to verify the effectiveness of the plasma actuator in changing the lift are presented in the third chapter. Chapter four gives an overview of the performed experiments, showing the plasma actuator configurations

and experimental test set-ups used. Chapter five presents and discusses the experimental results. The conclusion of this research is presented in chapter six together with recommendations for future work.



---

# Chapter 2

---

## Theory

This chapter will give an introduction into active load control, discussing the different classifications of actuators that have been developed over time and stating the most important requirements necessary for an actuator to be successful. After this the Dielectric Barrier Discharge (DBD) plasma actuators (PA) are introduced and an attempt is made to give a general review on the working principles of the technique and to discuss the applications for which the DBD plasma actuator shows promising results.

### 2.1 Active load control

Active flow control involves the control of local airflow around a body in order to alter the aerodynamic forces acting on it. The purpose of flow control is often to improve the aerodynamic performance of an airfoil or lifting surface. However, for the application on wind turbines the main focus is to reduce the extreme loads at high wind speeds and to mitigate fatigue loads occurring randomly. In general, the intent of flow control devices is to delay/advance transition, to suppress/enhance turbulence or to prevent/promote separation. The effects can include drag reduction, lift enhancement, mixing augmentation or aeroacoustic noise reduction. It should be noted that these effects are not mutually exclusive and changing one effect can have adverse results in other areas.

#### 2.1.1 Active vs. passive control

Devices that are used for active flow control are characterized by the need of an external energy source, or auxiliary power. Flow control devices that do not require an external energy source are called passive. Examples of passive flow control devices are fixed vortex generators for separation control and trailing edge Gurney flaps for lift enhancement. A disadvantage of most passive devices is that they influence the flow at all times, which can lead to detrimental effects at certain flow conditions. Active flow devices are commonly implemented with a control system in order to reduce its energy consumption, to increase its efficiency by activating it at the right moments and to control the magnitude of the effects generated. The control system usually consists of the active flow control actuator and incoming flow condition sensors. A control system analyses the input from the sensors and uses a predetermined algorithm to command the actuators. It is also possible that another sensor is used to measure the effect of the actuator on the flow. This data

is then used as feedback to compare the actual output with a desired output. The controller can change the commands sent to the actuator accordingly, such that flow control is optimized. A fast response of the whole system is important in order to counteract the variations in local flow conditions. In this work the focus lies with the discussion of different active flow control actuators. It does not go into detail on controllers and sensors. However, it is important to keep in mind the complete system, since a chain is only as strong as its weakest link.

In the past decades many flow control actuators have been invented. All of the actuators function in a different way and can be used to control different flow phenomena. Many of the techniques are developed in other fields than wind turbine control, such as helicopters and unmanned aerial vehicles (UAVs), and every actuator is in another stage in its development. This makes it difficult to directly compare them with each other. The focus in this work will be on the DBD plasma actuator, which is still in full development but shows potential for active load control. An attempt is made to describe the mechanical and aerodynamic working principles and the possibilities of the actuator.

### 2.1.2 Classification

There are several characteristics of active control actuators that can be used to classify each technique. Classifications made here are based on how they interact with the flow, the location where they are applied on an airfoil, the aerodynamic effect they produce and how the actuator operates in time. This method is based on the labelling scheme as defined in a paper on flow control on UAVs by Wood[64].

#### Interaction

The active control technique can either work as a geometrical, fluidic or plasma actuator. Geometrical actuators change the effective shape of an airfoil, thereby changing the airflow around it and thus the aerodynamic forces acting on it. Fluidic actuators change the airflow around an airfoil by either adding air into or subtracting air from the external flow. Plasma actuators use an electric field to generate a body force on the surrounding airflow, resulting in a local momentum addition to the flow.

#### Location

Actuators can be placed anywhere on the airfoil surface, depending on their working principle. A distinction is made between the leading edge (LE), mid chord (MC) and trailing edge (TE).

#### Aerodynamic effect

The aerodynamic effect that an actuator produces is divided into two groups. The first group holds all actuators that increase/decrease the lift/load with an approximately constant amount over a wide range of angles of attack in the linear part of the lift curve, see figure 2.1. This happens when the effective camber of an airfoil is changed by the action of the actuator. By actuation the actuators can directly influence the produced lift/load and are therefore capable of damping the oscillating loads generated by unsteady inflow conditions. In most cases these actuators can be used to increase and decrease the lift by simply mounting them on both the upper and lower side of an airfoil. This has already been demonstrated by the use of the well known ailerons for flow control.

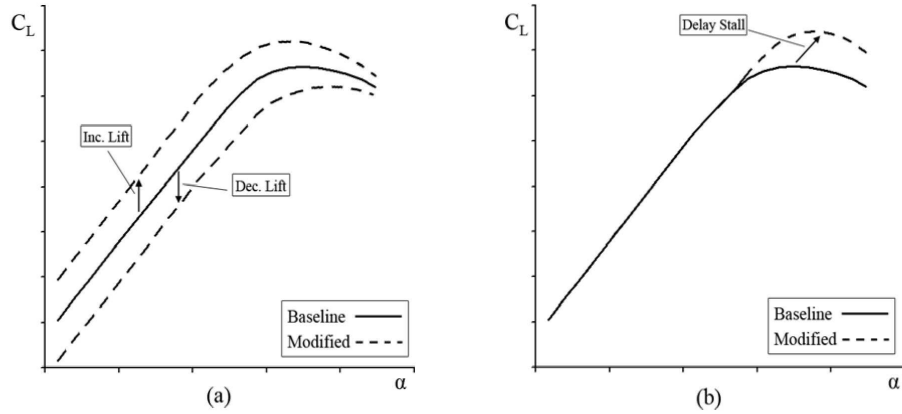


**Figure 2.1:** Aerodynamic effect of AFC devices on baseline lift curves: (a) lift/load control devices (b) flow separation control devices[5].

A second effect that can be achieved by flow control actuators is the delay of stall, meaning that the flow over an airfoil separates at a higher angle of attack. This results in a considerable increase in lift at high angles of attack. However, these devices are not directly capable of increasing and decreasing the loads on an airfoil in a short amount of time, therefore it seems that increasing the stall angle of attack is not effective for load control. Although, there is an alternative method that involves the redesign of an existing blade with stall delay devices. As was said before, implementing actuators on an existing design can delay the stall angle of attack, or in other words, can increase the maximum section lift coefficient  $c_{lmax}$ . Rewriting the equation for the section lift coefficient results in the following expression for the lift generated:

$$l_{max} = c_{lmax} \cdot q_{\infty} \cdot c \quad (2.1)$$

Where  $q_{\infty}$  is the dynamic pressure of the free stream and  $c$  is the chord length. When  $c_{lmax}$  is increased, then  $c$  can be reduced so that the lift generated by the airfoil stays the same. Applying this modification to the whole blade, with blade lift coefficient  $C_L$ , results in a lift curve slope according to:

$$\frac{dL}{d\alpha} = \frac{dC_L}{d\alpha} \cdot q_{\infty} \cdot S \quad (2.2)$$

Where  $S$  is the wing area, equal to the wing span  $b$  times the chord  $c$ . The variation of  $C_L$  with angle of attack  $\alpha$  is generally given by the expression for the lift curve slope of a low speed high aspect ratio 3D wing:

$$\frac{dC_L}{d\alpha} = \frac{a_0}{1 + \frac{a_0}{\pi \cdot A \cdot e}} \quad (2.3)$$

In which  $a_0$  is the lift curve slope for a 2D airfoil section, equal to  $2\pi$  for symmetric airfoil with infinite wingspan and  $e$  is the Oswald efficiency number, representing a correction factor for a non-elliptical lift distribution. The  $A$  is the aspect ratio of the wing equal to:

$$A = \frac{b^2}{S} = \frac{b}{c} \quad (2.4)$$

Substituting equation 2.3 in 2.2 and using 2.4, the variation of the lift force with angle of attack becomes:

$$\frac{dL}{d\alpha} = \frac{a_0}{1 + \frac{a_0 \cdot c}{\pi \cdot b \cdot e}} \cdot q_\infty \cdot b \cdot c \quad (2.5)$$

Making the assumptions that the 2D lift curve slope and the Oswald factor stay the same for the modified airfoil, the smaller chord will result in a decrease in  $dL/d\alpha$ . This effect is illustrated in figure 2.2. The maximum lift of the original blade and the modified blade with a smaller chord are the same, but the slope of the linear part,  $dL/d\alpha$ , is reduced.

Oscillating loads are caused by changes in lift. These changes in lift can for example be caused by turbulence, i.e. changes in flow velocity (indirectly influencing the angle of attack) and/or small changes in angle of attack. As can be seen from figure 2.2, the same variation in angle of attack will lead to a smaller variation in lift when the lift curve slope is reduced. At the same time the maximum occurring lift value for the same variation in angle of attack is reduced. This indicates that stall delaying actuators are capable of reducing the oscillating loads. Additionally, the reduction in chord length leads to smaller blades and consequently a reduction in required materials. This will further decrease the wind energy costs.

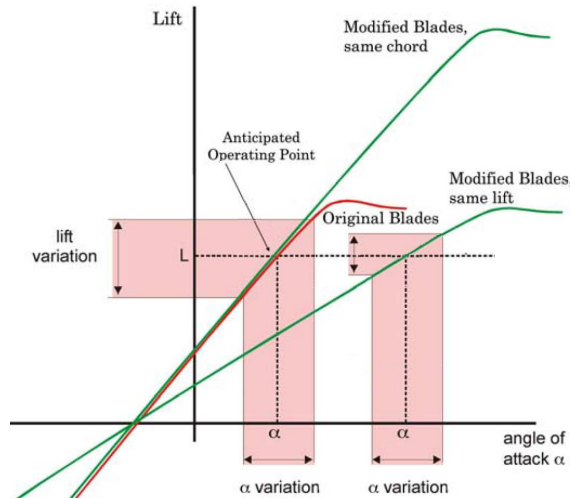


Figure 2.2: Graph showing the benefits of using stall delay devices, based on[27].

## Operation in time

The final classification makes a division between a steady and unsteady operation. The main difference is that an unsteady actuator oscillates around a nominal value with a certain frequency. For example, a trailing edge flap can be set to a range of deflection angles and therefore generate a range of aerodynamic forces. However, when the flap deflection is directly related to the incoming flow conditions, the lift variation is considered to be a series of steady state conditions and the actuation is called steady. Only when the flap oscillates around a nominal value and can be assigned a certain frequency the actuator is marked as unsteady. Most of the devices that can perform unsteady actuation are also capable of steady operation.

### 2.1.3 Requirements

Although each active flow control (AFC) actuator operates differently, there are certain requirements for an actuator to be successful[27]. The most important requirements are listed here:

- The actuator should be small such that multiple actuators can be distributed along the span to provide sectional flow control.
- The actuator should be scalable, meaning that it is effective for a range of chord lengths and Reynolds number.
- In order to control the randomly oscillating loads the actuator should have a fast time response.
- For control purposes a linear behaviour in actuation is beneficial.
- It is necessary for the actuator to be durable and robust in order to withstand harsh environments (rain, corrosion, humidity, salt, lightning, etc.).
- The AFC actuator should be reliable and not affect the wind turbine operation when it fails.
- The actuator should be replaceable and inexpensive in case of failure.
- The addition of the AFC actuator should not increase the maintenance costs and the lifetime of the wind turbine should not change (no reduced performance).
- The actuator should not considerably increase the weight of the blades such that additional gravitational loads are limited and the aerodynamic stability, the position of blade centre of gravity with respect to the aerodynamic centre and the elastic axis, is not considerably affected.
- The implementation of the actuator should not significantly increase the complexity of the manufacturing process.
- The power consumption by the actuator must be as low as possible so that the energy to operate the AFC actuator does not reduce the overall energy capture of the wind turbine.
- And most important, the AFC actuator should decrease the cost of energy of a wind turbine.

## 2.2 Plasma actuators for load control

In this section an attempt is made to give a general review on the working principle of Dielectric Barrier Discharge plasma actuators. During the last 10 years the use of plasma actuators has become very popular in a wide range of applications and the amount of research papers on the subject is big and still growing. It is therefore difficult to fully cover the subject in this literature survey. The review presented here is especially based on the extensive reviews on plasma actuators recently published[41, 13, 11].

### 2.2.1 Plasma

The term plasma was introduced in 1928 by Langmuir[37] to describe a region of gas discharge containing balanced charges of ions and electrons. This effectively means that an approximately equal number of positively and negatively charged species exist in the plasma region. Plasma is created by providing sufficient energy to molecules or atoms, so that the gas becomes ionized. Hence resulting in a gas with electrons, positive and negative ions, free radicals, gas atoms and molecules in the ground or any higher state (excited). It can exist in an extremely wide range of temperatures and pressures. It can be produced at low pressure or atmospheric pressure by coupling energy to a gaseous medium by several means such as mechanical, thermal, chemical, radiant, nuclear, electric or electromagnetic or by a combination of these[43]. In the case of an electrical source a gas discharge is created when an electric field of sufficient amplitude is applied

to a volume of gas to generate electron-ion pairs through electron impact, provided that initial free electrons are present[13]. Based on the degree of ionization a plasma is either called hot, if the gas is almost entirely ionized, or cold, if only weakly ionized.

After plasma is produced, it can be manipulated with electric and magnetic fields. In the presence of an electric field, the ionized air induces a body force vector field through collisions with the surrounding non-ionized air. This property of the plasma is of high importance in the working principle of the Dielectric Barrier Discharge plasma actuators, as will be shown later.

## 2.2.2 Dielectric Barrier Discharge

Over the years several types of plasma actuators have been developed, of which the atmospheric pressure DBD is most commonly applied for flow control. The DBD plasma actuator consists of at least two electrodes mounted on opposite side of a dielectric material and arranged in an asymmetric configuration, such as shown in figure 2.3.

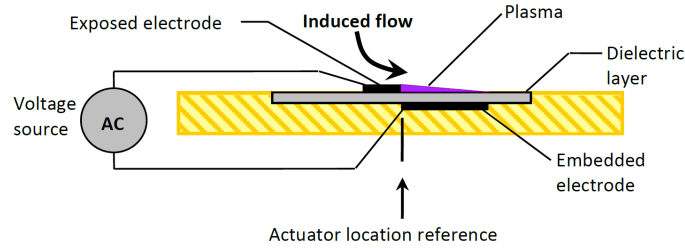


Figure 2.3: Schematic of a single DBD actuator[11].

Due to the existence of the dielectric layer the exposed electrode needs to be connected to an alternating current (AC) high voltage supply while the covered electrode is grounded. This configuration is referred to as a single DBD. Common dielectric materials used are Teflon, Kapton, glass, ceramic or PMMA (Plexiglas)[51]. The thickness is usually between 0.1mm and a few mm. Depending on the dielectric material and thickness, typical values of applied peak-to-peak voltage  $V_{app}$  and actuation frequency  $f_{ac}$  are 5-40kV and 0.1-30kHz[35], respectively. Although the applied voltage is very high, this configuration has a relatively low power consumption due to the dielectric material blocking the current flow between the electrodes. As a result of the AC high voltage a weakly ionized plasma region is created between the two electrodes, which by interaction with the electric field induces a body force field by ion-neutral collisions adding momentum in the near-wall region.

## 2.2.3 Plasma actuator physics

In the following section the plasma actuator physics will be discussed. Important parts are the plasma actuator discharge cycle, where the physics of the discharge during a AC high voltage wave are given, the forcing mechanisms of the plasma on the neutral air and the resulting induced electric wind.

### Plasma actuator discharge cycle

The electrode configuration in a DBD actuator creates an asymmetry in the discharge between the two AC half-cycles. During the first half-cycle the exposed electrode is negative (cathode), referred to as the forward stroke, while for the second half cycle the exposed electrode is positive (anode),

referred to as the backward stroke. When the absolute voltage is increased above the breakdown electric field,  $E_b$ , which is the value required to sustain electron-ion pairs in the gas in the absence of a space-charge field[13], the air between the exposed and covered electrode becomes weakly ionized and plasma is created. The plasma discharge consists of a large number of consecutive micro-discharges across the gap between the exposed and the covered electrode[33]. The discharge can be divided into two regimes depending on the polarity of the exposed electrode[4, 35]. During the forward stroke the exposed negative electrode emits electrons as it is a bare metal. The electrons are accelerated towards the dielectric surface due to the Coulombian forces exerted by the electric field. See figure 2.4 for a schematic of electron behavior during the half-cycles.

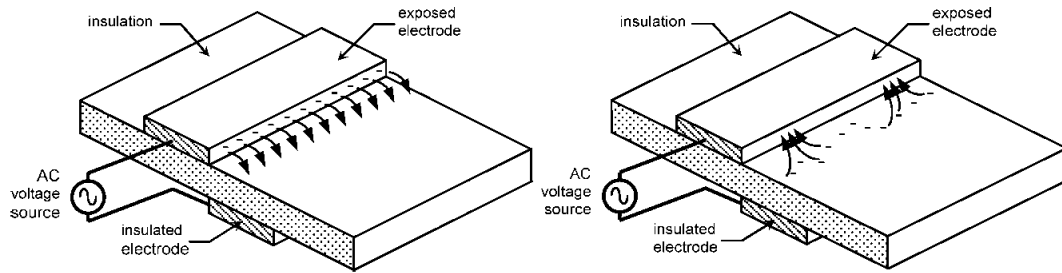


**Figure 2.4:** Schematic of the half-cycles. During the forward stroke the electrons emitted from the exposed electrode accumulate on the dielectric surface (on the left) and in the backward stroke return to the bare electrode (on the right)[17].

Since the bare electrode is an infinite source of electrons this will result in a multitude of small micro-discharges. This is named the glow regime. On the other hand, during the backward stroke the exposed electrode is positive and the electrons that were accumulated on the dielectric are now drawn towards the exposed electrode. At this point however, the electrons are provided by the accumulated species on the dielectric and thus not so readily available as during the forward stroke. This results in fewer larger micro-discharges, which is called the streamer regime. In the glow regime the micro-discharges can be seen as electron avalanches while in the streamer regime the electrons are packed in bundles, i.e. filaments. Figure 2.5 clearly shows the difference between the two discharge regimes in relation to the waveform shape (which will be discussed later).

In both regimes, when the (kinetic) energy of the electrodes is high enough, positive ions ( $O^+$ ,  $N^+$ ) and negative ions ( $O^-$ ) are formed through ionization and attachment processes (inelastic collisions), respectively. The ions also move between the exposed electrode and dielectric surface in the direction of opposite polarity, causing similar reactions. In the glow regime the micro-discharges ignite when the breakdown electric field is reached and extinguish due to the charge build up on the dielectric. Due to this charge build up the local electric field strength drops below the breakdown value and thus terminates the current flow. This indicates the necessity of AC voltage supply. The duration of a micro-discharge is about 1-10ns and they happen in rapid succession and at different locations along the exposed electrode.

By eye the plasma looks like a uniform purple/blue glowing sheet as seen in figure 2.6 and can be observed when a room is dark enough. The glow is created by de-excitation of excited species (atoms and molecules). As long as the charge build-up on the dielectric is overcome by a continuous increase in voltage (negative or positive) the micro-discharges continue to happen. Increasing the peak-to-peak voltage or the actuation frequency will allow the build-up of higher charges on the dielectric, which will eventually lead to an arc across the dielectric, destroying the dielectric layer[20].

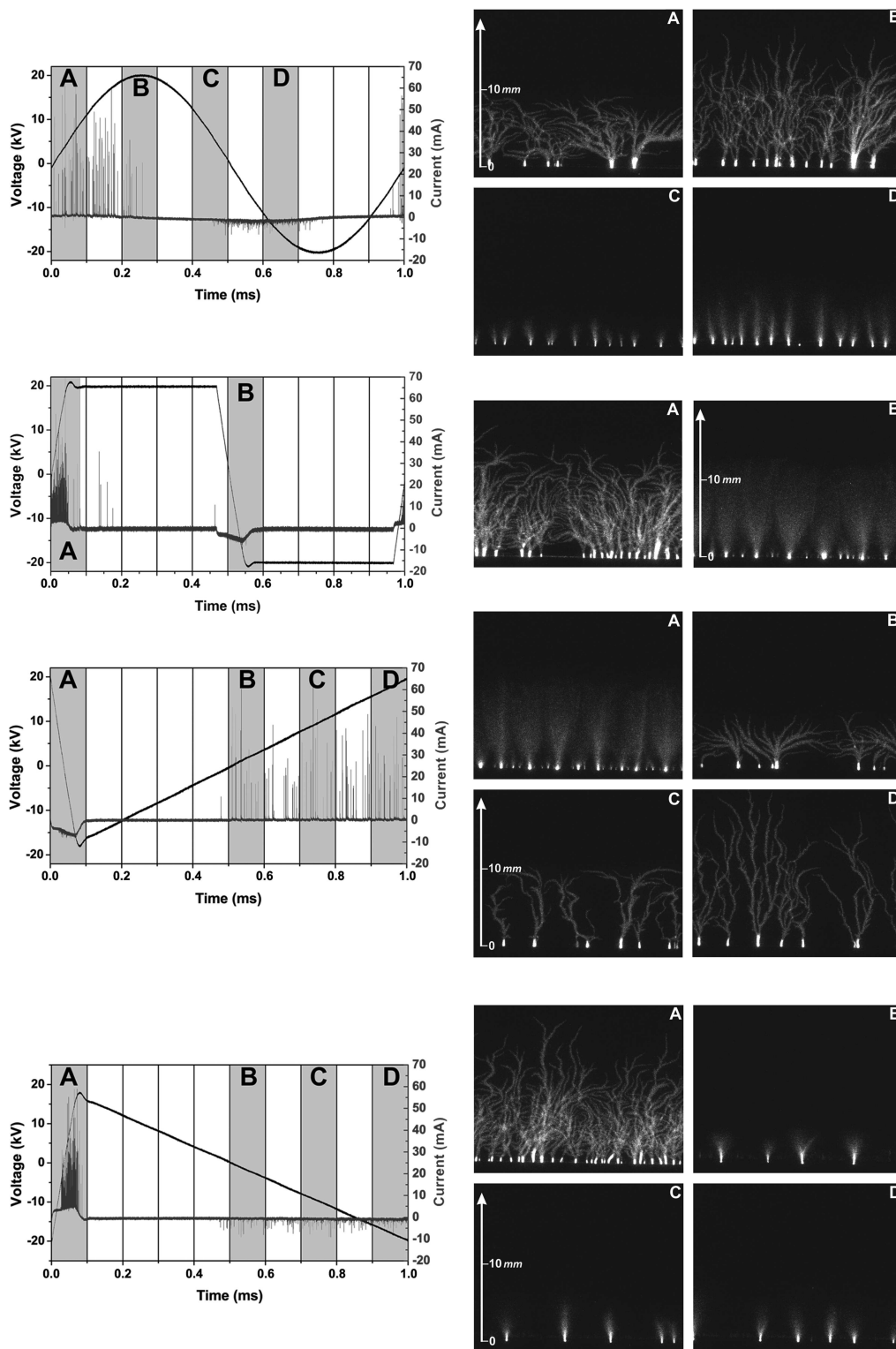


**Figure 2.5:** Total discharge current and fast-imaging of the developing plasma layer for (top to bottom): sine, square, positive ramp, negative ramp waveforms (images are for a fop view and opening gate of  $100\mu\text{s}$ ) [4].

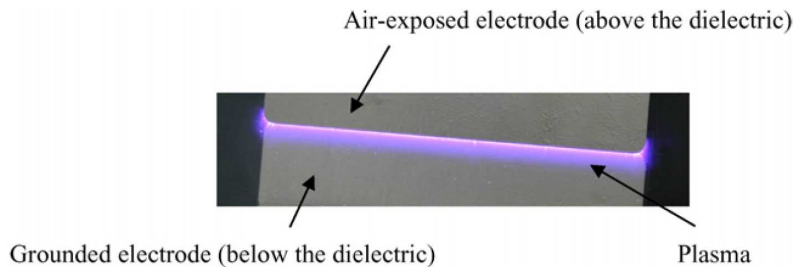
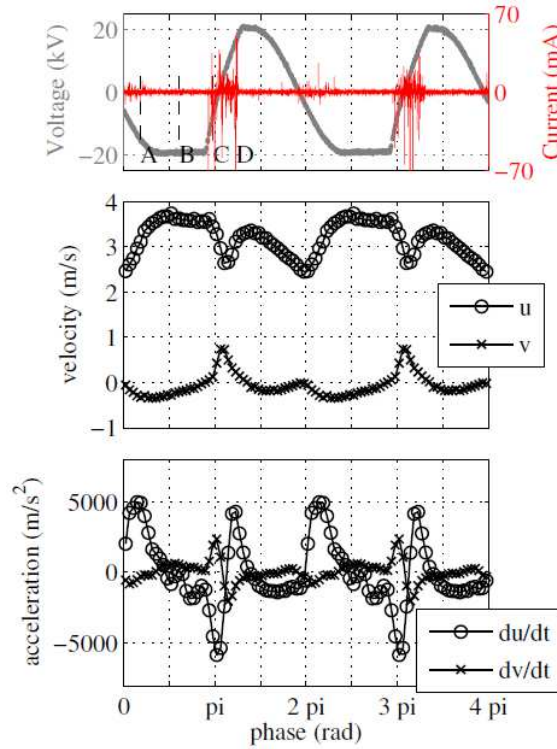


Figure 2.6: Actuated DBD plasma actuator showing the purple/blue glow[41].

### Forcing mechanisms

Due to the asymmetry of the discharge during the two half-cycles, the ion-neutral momentum coupling, which results in a thrust force acting on the flow, is also asymmetric. Although this is of fundamental importance to the understanding of the DBD forcing mechanisms it has been controversial in the past. It is widely regarded that collisional processes drive the momentum transfer and since the electric field oscillates during the AC high voltage period, the induced forcing on the charged species is expected to be unsteady. This states that the frequency of charged species-neutral particles collisions within the plasma region is of the same or larger order as the plasma actuation frequency[7]. The problem lies at experimental and numerical information on the influence of each half-cycle and more specifically the applied forcing at each stroke is controversial. There has been a limited number of experimental investigations on the forcing mechanisms of the actuators. Time-resolved Laser Doppler Anemometry (LDA) measurements were conducted in quiescent air where the asymmetry in the two half-cycles was evident[20]. Large momentum transfer during the negative half-cycle was recorded which corresponds with the recent modelling efforts. In another study, phase locked Particle Image Velocimetry (PIV) measurements also indicated the dominance of the negative cycle in the momentum transfer[32]. With a different technique, using a Photo Multiplier Tube (PMT), Enloe et al.[15] and Font et al.[19] showed positive momentum transfer during both half-cycles. Further research by Boucinha et al.[8] suggests that the cycle can be separated into four parts. In the first part of the forward stroke they observe a clear positive momentum input followed by a mild deceleration in the second part. During both parts of the backward stroke a small deceleration is exerted on the flow, thereby keeping the induced flow velocity of one cycle constant. These experiments on the temporal evolution of the net force production indicate multiple interpretations for the half-cycles. Additionally, it is found that the effect of the waveform shape has a major influence on the performance of the DBD actuator[62, 8, 4].

A recent study performed by Kotsonis[35] investigated the effect of the high voltage waveform on the produced body force and consumed power, see figure 2.7 for a typical forcing diagram. Results showed that the time gradient of the voltage plays a significant role. A steep voltage drop at the beginning of the forward stroke produces significantly less thrust while a steep voltage rise at the start of the backward stroke increases thrust with respect to the common sinusoidal rise. Smooth voltage changes seem to decrease the number and intensity of the current peaks, thus reducing the power consumption. This especially holds for the glow regime whereas the streamer regime is more insensitive due to its filamentary nature. Again a four stage cycle is suggested, with positive momentum input at the beginning of each voltage reversal and a deceleration for the remainders due to hydrodynamic stresses and pressure effects. An interesting observation was the deceleration at the beginning of the backward stroke, which can be reduced by using a sharp voltage rise. It was found that a combination of a sine and square voltage waveform made the best use of these findings. The corresponding voltage, current, velocity and accelerations are displayed in figure 2.7. The produced thrust increased by 30% and the induced velocity by 40% compared to the



**Figure 2.7:** Evolution of the velocity and acceleration within the high voltage cycle for the a combined sine-square waveform (values probed at  $x = 5\text{mm}$ ,  $y = 0.4\text{mm}$  from exposed electrode edge)[35].

conventional sine shape waveform. The power consumption only increased marginally, resulting in a relative thrust efficiency increase of 25%.

### Induced electric wind

As the charged particles in the plasma move under the Coulombian forces of the electric field between the exposed electrode and the dielectric surface, they collide with neutral gas particles transferring momentum to the gas. The overall momentum flux will be in the direction of the ion movement, since the contribution of the electrons can be neglected. These collisions are called Lorentzian collisions[26]. Every collision contributes to the body force exerted on the gas and thereby induces flow velocities above the surface of the electrodes. The induced flow is characterized by a depression of the flow towards the wall above the exposed electrode and a tangential to the wall velocity from the exposed to the covered electrode. The induced movement of the gas, created by Coulombian forces acting on the ions and electrodes and the Lorentzian collisions, is called the electric wind[49].

#### 2.2.4 Effect of actuator parameters

For flow control purposes the maximum induced velocity and the induced velocity profiles are of importance. The velocity induced by the electric wind depends on electric and geometric design parameters. Electric parameters are the actuation frequency ( $f_{ac}$ ), applied peak-to-peak voltage ( $V_{app}$ ), waveform and the capacitance of the actuator depending on the dielectric thickness ( $t_d$ ) and the dielectric properties (dielectric constant/relative permittivity  $\epsilon_r$  and dielectric strength  $E$ [51]). The geometric important parameters are the exposed electrode thickness ( $t_e$ ), covered electrode width ( $w_c$ ) and electrode gap ( $g$ ), see figure 2.8.

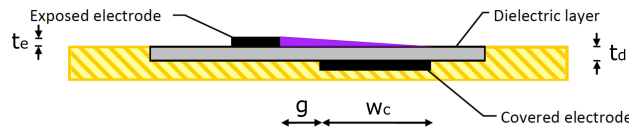


Figure 2.8: Schematic of a single DBD plasma actuator indicating the geometric parameters[11].

### Geometric effects

The thickness of the bare electrode,  $t_e$  has a considerable effects on the induced flow, as has been shown by Enloe et al.[17]. They compared flat copper electrodes of different thicknesses and concluded that the thrust production is larger for thinner electrodes. An explanation for this is that a sharper edge concentrates the electric field lines, thereby locally increasing the electric field and hence generate an earlier onset of plasma.

The effect of the covered electrode width,  $w_c$ , and gap spacing,  $g$ , on the maximum induced velocity for a single DBD actuator has been investigated by Forte et al.[20]. They observed that the induced velocity increases with the covered electrode width until an asymptote is reached, as displayed in figure 2.9. The larger  $w_c$  the further the plasma can extend. However, when the distance between the edges of the electrodes has become too large an asymptote is reached. Only increasing the voltage could yield further extension of the plasma in that situation.

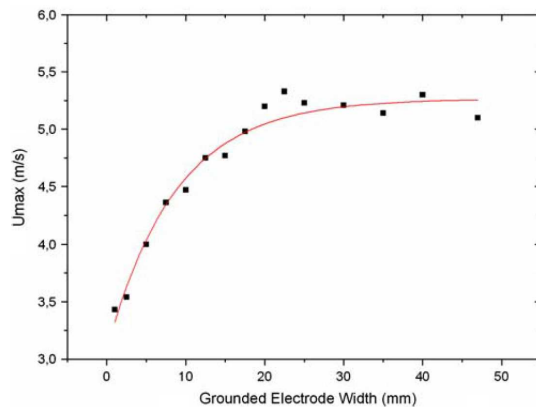


Figure 2.9: Asymptotic evolution of the maximum induced velocity with the grounded electrode width[20].

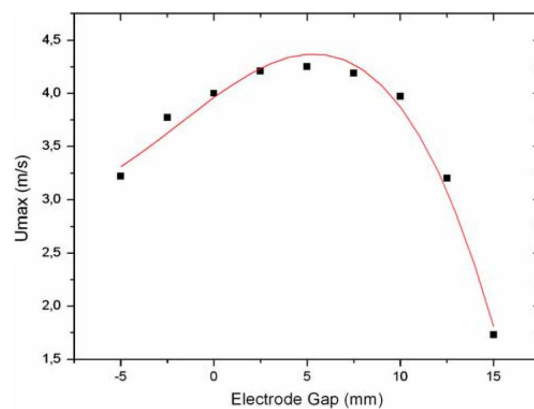


Figure 2.10: Evolution of the maximum induced velocity with the electrode gap [20].

The gap spacing,  $g$ , is specified as positive when there is no overlap between electrodes. The covered electrode width is a significant factor for the gap spacing, thus the gap is to be normalized with  $w_c$  for non-dimensionality. Figure 2.10 displays the maximum induced velocity against gap spacing for a covered electrode width of 5mm. From the figure Forte et al.[20] concluded that for  $0 \leq g/w_c \leq 2$  there is little effect on the maximum velocity, while for  $g/w_c \geq 2$  and  $g/w_c \leq 0$  the induced velocity drops off rapidly. Negative gap spacings are discouraged due to faster degradation of the dielectric material, resulting in a limited lifetime of the plasma actuator, and due to an increased power consumption.

### Electric effects

The effects of voltage and actuation frequency on the velocity induced by the electric wind and the extent of the plasma has been investigated by Orlov[45]. It was found that the maximum

extent increased linearly for increasing peak-to-peak voltage ( $V_{app}$ ), and that it was independent of the actuation frequency ( $f_{ac}$ ). This effect is shown in figures 2.11 and 2.12, respectively. Furthermore, the maximum velocity of the electric wind increased with the applied voltage, but also with the AC frequency. The effect of the voltage can be linked to the strength of the electric field. Increasing the applied voltage will first of all increase the region where the breakdown electric field is reached and thus increase the extend of the plasma region. Secondly, the stronger field will exert larger Coulombian forces on the charged particles leading to higher energy transfer during the Lorentzian collisions. The effect of the actuation frequency can be linked to the frequency at which the Lorentzian collisions occur. A higher actuation frequency results in more collisions and therefore more occasions of momentum transfer. This will create higher velocities without increasing the plasma extent.

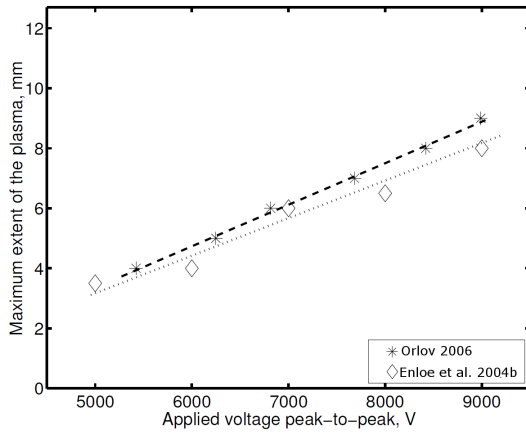


**Figure 2.11:** Maximum extent of the plasma as function of  $V_{app}$ [45].

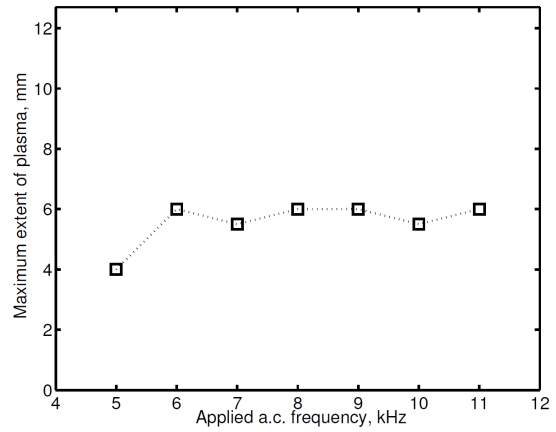


**Figure 2.12:** Maximum extent of the plasma as function of  $f_{ac}$ [45].

Enloe et al.[17], Roth and Dai[51] and Forte et al.[20] found that the behaviour of the velocity profiles at various voltages and frequencies are entirely different. An example illustrating the behaviour of induced velocity profiles with voltage is presented in figure 2.13. As can be seen, the location of the maximum velocity drops from around a height of 1mm at 12kV to approximately 0.5mm at 20kV. For voltages up to 20kV and at low frequencies of 300-700Hz Pons et al.[29] and Forte et al.[20] indicate that the location of the maximum induced velocity is located at approximately 0.5mm from the wall. The last group optimized the performance of the single DBD actuator and reached induced velocities up to 8m/s.

Measurements of Enloe et al.[17] indicated that the maximum induced velocity produced by the actuator is proportional to  $V_{app}^{7/2}$ , see figure 2.14. They described that for increasing  $V_{app}$  the maximum induced velocity was limited by the spanwise extent of the covered electrode. Hence, the area required to store the charge can be too small to gain the maximum effect of the applied voltage.

The simulations of Orlov[45] and Orlov et al.[46] have indicated that for a specific actuator geometry there is an optimum AC frequency that depends on the actuator capacitance, at which the induced thrust is largest. However, the power consumption continues to increase monotonically with AC frequency. This implies that the selection of the AC frequency is of importance for an optimum performance of the actuator. If the frequency is chosen too high (past the optimum), a lot of the power will be dissipated by heating of the air. The optimum  $f_{ac}$  depends on the capacitance of the actuator, which is determined by the properties of the dielectric material. The

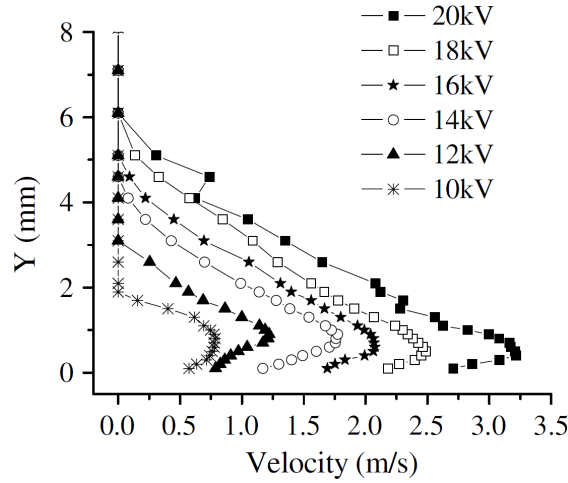


**Figure 2.13:** Typical velocity profiles measured with a glass Pitot tube for different voltages. ( $t = 4\text{mm}$  glass dielectric,  $g = w_c = 5\text{mm}$  and  $f_{ac} = 300\text{Hz}$ )[41].

capacitance is proportional to  $\epsilon_r/t_d$ , where  $\epsilon_r$  is the dielectric constant or relative permittivity and  $t_d$  the dielectric thickness. The power loss through the dielectric is proportional to  $f_{ac}\epsilon/t_d$ , hence lowering the capacitance also reduces the power loss. A reduction of the capacitance would also allow the maximum body force to be produced at higher frequencies, and thereby increasing the maximum induced velocity. Hence, the general objective is to lower the capacitance[13]. This is also confirmed by Thomas et al.[59] stating that a lower capacitance (i.e. lower dielectric constant and/or increased thickness) allows for higher sustainable applied AC voltage without arcing or entering a less favourable plasma regime. The ability to form uniform glow plasma at higher voltages results in an increase in the maximum achievable body force (i.e. thrust).

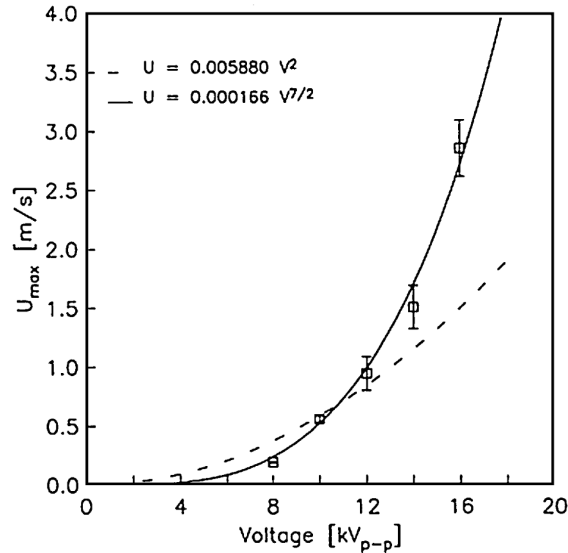


**Figure 2.14:** Maximum velocity induced in air by actuator approximately proportional to  $V_{app}^{7/2}$  (triangular waveform,  $f_{ac} = 5\text{kHz}$ )[17].

Aside from the capacitance and the dielectric coefficient, the dielectric material has another significant property namely the breakdown voltage per thickness  $E$ [51]. This is an important property,

since the minimum thickness of the dielectric needs to be enough to avoid breakdown at the applied voltage. Depending on the material this could be achieved within a fraction of a millimetre (0.05mm is typical for Kapton)[11].

Finally, as discussed in section 2.2.3, the AC waveform has a significant effect on the performance of the SDBD plasma actuator. It can reduce the power consumption and enhance the induced electric wind. From Kotsonis[35] it is found that a smooth voltage drop (begin of forward stroke) is important for a higher thrust and lower power consumption whereas a steep voltage rise (begin of backward stroke) minimizes the negative momentum input, resulting in higher thrust without a significant effect on power consumption (since no electrons are emitted from the covered electrode).

### 2.2.5 Steady and unsteady actuation

The induced velocity of the plasma actuator follows the high frequency AC input signal. However, these time scales are generally much smaller than those present in the flow. Therefore the electric wind and the body force generated by the actuator appear steady. However, an unsteady actuation can also be applied using a signal generator, such that in a time interval  $T_1$  the actuator could be active only during sub interval  $T_2$ , see figure 2.15. The frequency of this pulsed actuation is then  $1/T_1$  and is called the pulse frequency  $f_p$ . The pulse frequency can be much lower than the actuation frequency such that the time scale of the actuator induced quantities can be much larger. This way the actuator could interact with the fluctuating flow quantities and use the high response time of the actuator to full extend. The ratio  $T_2/T_1$  is called the duty cycle (DC) and indicates the time fraction that the plasma actuator is active. The ability to apply pulsed actuation and reducing the duty cycle can reduce the power consumption of the plasma actuator considerably.

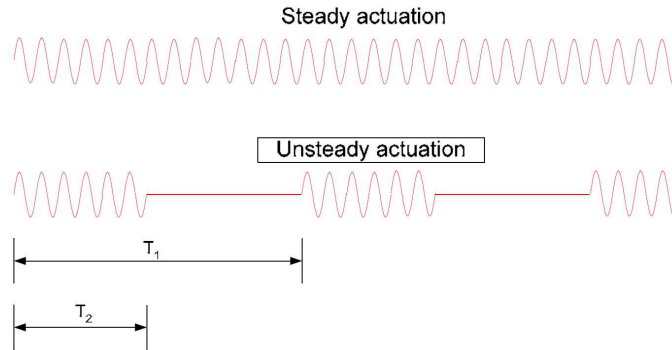


Figure 2.15: Steady and unsteady actuation[60].

## 2.3 Plasma actuator applications

Today there are many actuators that are classified as plasma actuators. Different configurations are researched and developed every year since their introduction into active flow control in the late 90's. The initial research on surface plasma and the development of these simple actuators allowed many researchers in aerodynamics to study the effects of plasma actuators without being a specialist in plasma generation. This led to a considerable growth in the field since 2000 and therefore the DBD plasma actuator is used in multiple areas of active flow control. In this section a brief overview is given of the different applications in which the DBD plasma actuator is used for active flow control. DBD plasma actuators are most commonly applied in transition control on

flat plates, vortex shedding control on circular cylinders and laminar/turbulent separation control on airfoils[41].

### 2.3.1 Transition control

DBD plasma actuators can be used for laminar flow control by manipulation of the mean flow and consequently delay or advance transition. The delay of transition has only been reported for low free stream velocities, below 10m/s[21]. Figure 2.16 shows an experimental setup used for transition control. During this experiment the laminar boundary layer, under influence of an adverse pressure gradient, was artificially perturbed in order to introduce Tollmien-Schlichting (TS) waves. Downstream, two steady operating DBD plasma actuators were used to accelerate the flow and re-energize the laminar boundary layer, making the velocity profile more full and therefore more stable. As a result the TS waves were damped and transition was delayed for about 10cm, measured between base and actuated flows. In later experimental studies, with the same set-up, the use of plasma actuators in pulsed mode resulted in similar transition delays with considerable less power consumption[21, 22].

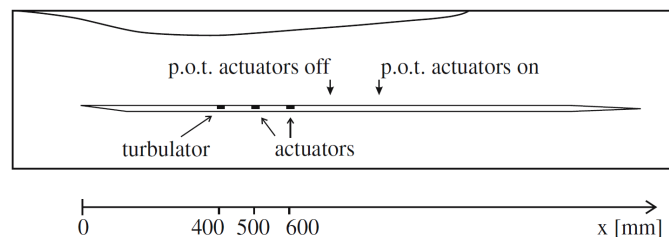


**Figure 2.16:** Schematic of the test setup showing the effect of plasma actuator on the point of transition[21].

In cases where the free stream velocity was higher than 10m/s the application of DBD plasma actuators tend to promoted transition instead of delaying it. Flat plate experiments on natural developed boundary layers at 15m/s and 22m/s were performed by Magnier[38]. Multiple DBD plasma actuators were placed at different locations in streamwise direction. Individual actuation showed that the actuators worked as turbulators, tripping the flow at their location and therefore moved the transition point upstream. The same effect was found by Séraudie[57], who also performed experiments on a flat plate at zero angle of attack. Although the jet created by the DBD actuator was directed downstream in order to add momentum to the flow in the near-wall region, the transition was promoted. These experiments were performed at high free stream velocities up to 50m/s and it was suggested that the effect of DBD actuators is limited at higher speeds due to the limited momentum input.

### 2.3.2 Vortex shedding control

Flow control experiments utilizing single DBD plasma actuators to control flow separation and unsteady vortex shedding from a circular cylinder in cross-flow are extensively studied, at low to moderate Reynolds numbers, by Thomas et al.[60] and Jukes et al[30]. Thomas et al. performed experiments at a Reynolds number of  $3.3 \cdot 10^4$ , based on the cylinder diameter. They clearly demonstrate that the use of four DBD plasma actuators effectively streamlines the circular cylinder, drastically reducing flow separation and eliminating the associated Kármán vortex shedding, see figure 2.17. The peak turbulence intensity in the wake was reduced by 50%. Additionally, the use of unsteady actuation proved to be very effective and reduced the turbulence intensity by 66%. The pulsed frequency was based on the Strouhal number defined as:

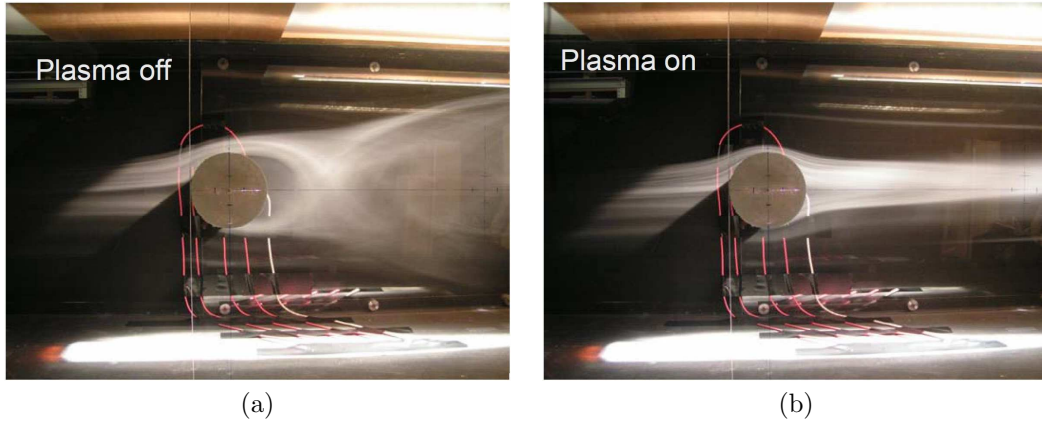


**Figure 2.17:** Smoke flow visualization images with (a) plasma actuators off and (b) plasma actuators on (steady actuation)[60].

$$St_D = f^+ = \frac{f_p \cdot D}{U_\infty} \quad (2.6)$$

The Strouhal number  $St_D$  or reduced frequency  $f^+$  may be thought of as a ratio between the characteristic time scale of the separated flow region,  $D/U_\infty$ , and the time scale for actuation,  $1/f_p$ . The separation control is in general found to be most effective at the value  $f^+ = 1$ , which indicates that the time scale of actuation should match with the separated flow region. The higher efficiency of pulsed actuation was achieved in combination with a DC of 25%, meaning that the power consumption is reduced by 75%. The same experiments were performed by Jukes et al.[30] at lower Reynolds number of  $6.5 \cdot 10^3$  and they confirm the findings by Thomas et al.[60].

Another approach for the use of DBD plasma actuators was presented by McLaughlin et al.[39]. Instead of delaying the flow separation around a cylinder the focus was put on controlling the Kármán vortex shedding. By placing two DBD actuators at  $\pm 90^\circ$ , such that they produced a downstream flow, the vortex shedding frequency was controlled by the pulsed actuation frequency. Locking of the frequencies occurred up to tested frequencies of 500Hz and flow velocities of 100m/s ( $Re = 3 \cdot 10^5$ ) with duty cycles as low as 5%. It was suggested that the short energy additions by the actuators is triggering flow instabilities that initiate the shedding of vortices. Another experiment was performed at a lower velocity of 7.5m/s ( $Re = 2.2 \cdot 10^4$ ) where the cylinder is covered by six actuators. Three on the top side acting upstream and three on the bottom side acting downstream at  $\pm 60^\circ$ ,  $90^\circ$  and  $120^\circ$ . When the actuators were operated in steady mode (DC = 100%) an upward movement of the rear stagnation point is observed together with a significant reduction of the recirculation zone. This could result in a net lift directed downwards, as would happen in case of a counterclockwise rotating cylinder. In this case continuous operation was most effective, although at higher free stream velocities the effect is diminished due to the lower momentum input of the actuator with respect to the free stream momentum[39].

### 2.3.3 Leading edge separation control

In most cases the single DBD plasma actuators are used for leading edge separation control on airfoils or wings. For example, Roth[50] studied the effect of single and multiple DBDs on the LE separation at high  $\alpha$  by flow visualizations at low velocities. Figure 2.18 shows a visualization of flow re-attachment over a NACA-0015 airfoil at  $\alpha = 12^\circ$ . The chord is 12.7cm and the free stream velocity is 2.85m/s, resulting in a Reynolds number of about  $2.4 \cdot 10^4$ . Although the flow

seems perturbed by the smoke (since the flow tends to separated at  $4^\circ$  in this study, whereas the separation usually occurs at  $12^\circ$  for the airfoil under investigation) it is clearly shown that plasma actuator is able to reattach the flow at higher  $\alpha$ . This result was reached by continuous actuation of 8 DBD actuators on the suction side of the airfoil. The actuators were positioned on the airfoil from approximately  $0.14x/c$  until  $0.77x/c$ .

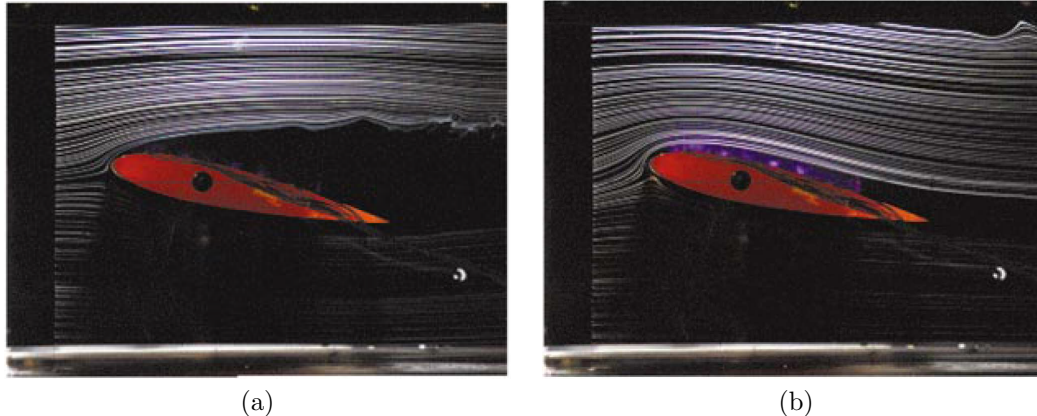


**Figure 2.18:** Flow visualization of NACA-0015 airfoil at  $\alpha = 12^\circ$  (a) with flow separation and (b) with flow re-attachment for  $V_{app} = 10\text{kV}$ ,  $f_{ac} = 4.2\text{kHz}$ [50].

At the University of Notre-Dame (US) researchers started working on DBD actuators more than 11 years ago[41]. In 2004[47] they published a paper in which two methods of flow control were compared: a passive method using vortex generators and an active method using DBD plasma actuators. The airfoil was a NACA-66<sub>3</sub>-018 with a chord of 12.7cm. Actuators were placed on the airfoil at  $x/c = 0$  and  $x/c = 0.5$ . The airfoil was instrumented for surface pressure measurements in order to calculate lift coefficients. Mean velocity profiles downstream of the airfoil were used to determine drag coefficients. Measurements were performed at velocities ranging from 10m/s to 30m/s, resulting in Reynolds numbers  $7.9 \cdot 10^4 \leq Re \leq 3.33 \cdot 10^5$ . The results showed that the actuators were capable to reattach the flow up to  $8^\circ$  past the baseline stall angle of attack. This was accompanied by a full pressure recovery and up to a 400% increase in the lift-to-drag ratio. The drag was calculated from the wake velocity profile, which showed an increase in the minimum peak deficit velocity and a reduction of the wake width, resulting in a drag reduction. Moreover, they demonstrated that the most effective actuator location to reattach the leading-edge flow separation was at the exact leading edge. This last point is important but leads to a question: is this effect only due to the velocity addition at the wall of the leading edge or might it be due to the laminar-to-turbulent transition induced by the pulse electric wind of such a surface DBD actuator.

In the same year Corke et al.[12] mounted a NACA-0015 airfoil on a force balance and studied more accurately the influence of the actuator position and the effect of unsteady actuation instead of steady actuation. They mounted one DBD at the leading edge and one at the trailing edge. The goal was to mimic the effects of a leading edge slat and a trailing edge flap. The chord was 12.7cm and the tests were performed at 21 and 30m/s, resulting in Reynolds numbers of  $2.17 \cdot 10^5$  and  $3.07 \cdot 10^5$  (corrected for blockage). Although the steady actuation was able to reattach the flow up to  $19^\circ$ , corresponding to  $4^\circ$  past normal stall angle, the unsteady actuation case was able to postpone stall by  $9^\circ$ . The pulse frequency used corresponded to a Strouhal number equal to one and separated flow region equal to the chord length, see equation 2.6. The duty cycle was only 10%, meaning that the power consumption was reduced by 90%. See figure 2.19 for lift and drag coefficients at 21m/s. Unsteady actuation at this velocity is capable of a lift coefficient recovery of  $\Delta c_l = 0.6$  beyond the normal stall angle of the plain airfoil.

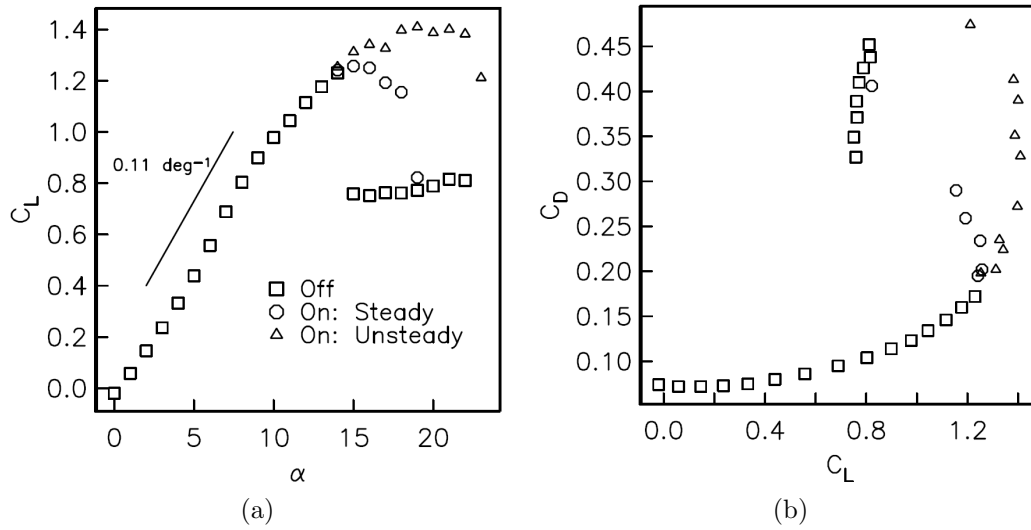


**Figure 2.19:** (a) Lift coefficient versus angle of attack and (b) drag polar for airfoil at 21m/s with plasma actuator off (squares), and in steady (circles) and unsteady  $f_p = 166 \text{ Hz}$  (triangles) operation[12].

All these studies are very interesting to understand the working principles of plasma actuators and to characterize the capability of the DBD plasma actuators. However, the Reynolds number is still much smaller than that in aircraft cruise conditions. Studies published in by Opaits et al.[44] and Zavyalov et al.[65] investigated the pressure distribution on the suction side of a 9cm chord NACA-0015 airfoil for velocities up to 110m/s corresponding to a Reynolds number of about  $6.6 \cdot 10^5$ . Although the test setup is not clearly described in this experiment, the results were promising. At 110m/s the plasma actuator had no effect until  $12^\circ$ , since there was no separation. Between  $12^\circ$  and  $20^\circ$ , the actuator is very effective, leading to a strong increase in the pressure distribution on the suction side of the airfoil due to reattachment of the flow. Above  $20^\circ$  also the actuated airfoil separated. In 2006, Roupassov et al.[52] performed the same kind of experiments but now with the electrodes in streamwise direction, resulting in an induced jet perpendicular to the free stream. The obtained results were similar, indicating that this layout could also reattach the airflow. This is important, because it indicates that the reattachment is not directly caused by the flow acceleration due to the jet. The effect may better be explained by the formation of 3D vortexes or by the laminar-to-turbulent transition inside the boundary layer. Both effects increase the mixing rate between the high momentum outer flow and the low momentum flow close to the wall resulting in a increased resistance against adverse pressure gradients[23, 56].

### 2.3.4 Turbulent separation control

Most of the previous work has focused on the separation control of thin laminar boundary layers such as leading edge separation control and vortex shedding from a cylinder. However, there also have been studies that focused on the use of plasma actuators for flow control of turbulent boundary layer separation. Which is important in relation to the current thesis work.

Jolibois et al.[28] published a paper that focused on the optimal location of the actuators with respect to turbulent separation control. They mounted seven independent actuators on the suction side of 1m chord NACA-0015 airfoil. The actuators were located between  $x/c = 0.3-0.8$ . In

this study the effect of laminar-to-turbulent transition in the boundary layer is uncoupled from the effect of the velocity addition close to the wall by tripping the boundary layer upstream of the actuators. The large chord of 1m results in a Reynolds number of  $4.0 \cdot 10^5$  at a velocity of 6m/s. Flow visualizations and PIV measurements were performed to show the effect of each actuator as a function of the flow separation point, which depended on the angle of attack (trailing edge stall). They investigated the ability of the DBD plasma actuator to displace (upstream and downstream) the position of flow separation by reattaching naturally detached airflow or, inversely, by detaching naturally attached airflow. The main result was that, whatever the angle of attack of the airfoil and the location of the separation point, the actuator must act at the separation point to be the most efficient with a minimum power input.

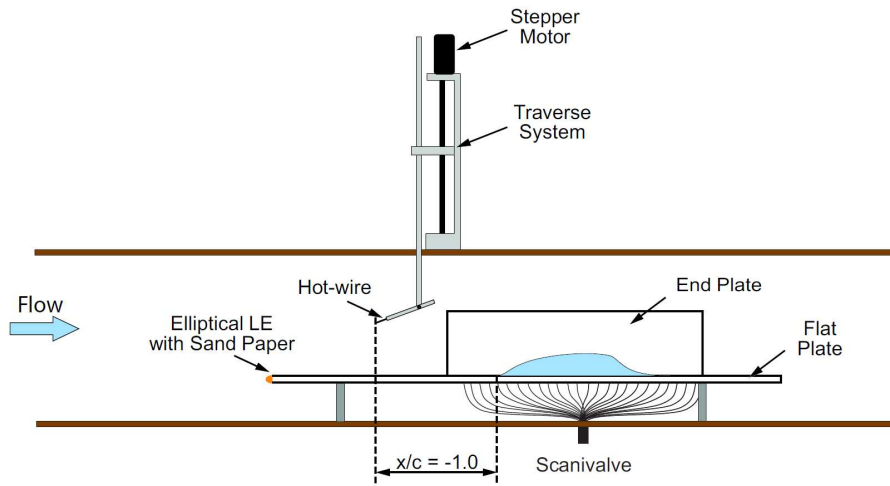
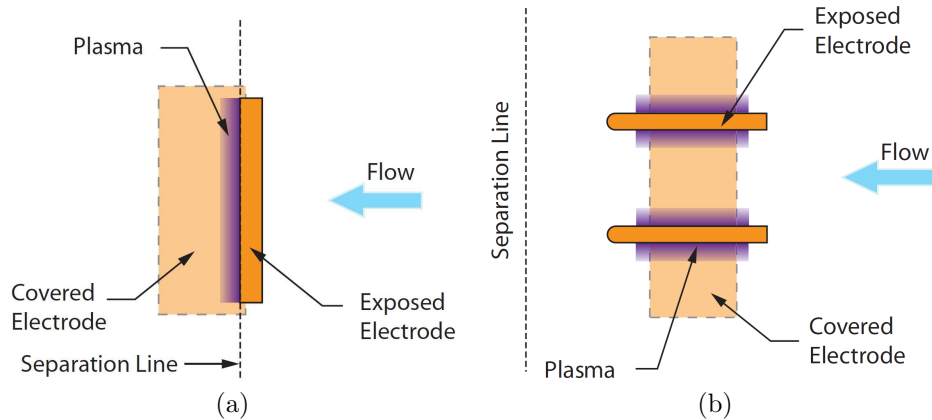


Figure 2.20: Schematic of the experimental setup for turbulent boundary layer measurements[23].

In his PhD work He[23] demonstrated the use of plasma actuators to control a turbulent separated flow over a wall mounted hump model, with the test setup as in figure 2.20. He performed experiments by measuring pressure distributions at a Reynolds number of  $2.88 \cdot 10^5$  and a flow velocity of 10m/s with spanwise and streamwise plasma actuator configurations, see figure 2.21. The spanwise actuator produces the wall jet while the streamwise actuator generates pairs of counter-rotating vortices that travel downstream, also called plasma streamwise vortex generators (PSVG). With the spanwise actuator gap located at the fixed separation location ( $x/c = 0.66$ ) and the streamwise actuator slightly upstream of this point, comparable results were produced. Both actuators ran in steady actuation and both configurations provided a pressure recovery in the separated region by decreasing its extent. It was stated that in general the spanwise plasma actuator can either be used in laminar separation control (unsteady operation) or turbulent separation control (steady operation) and that the streamwise actuator may be useful in both laminar and turbulent separated flows where the separation location changes.

The results found by He[23] were confirmed by Schatzmann[56]. In this study the effect of the spanwise and streamwise configurations were tested in a turbulent flat plate flow with zero pressure gradient and a turbulent boundary layer separated flow from a convex ramp with adverse pressure gradient, very similar to the hump model in figure 2.20. The free stream velocity was 5m/s and the corresponding Reynolds number was around  $2.8 \cdot 10^5$ . Flow visualization, PIV and LDV measurements indicated that the momentum addition in the near-wall region associated with the plasma-induced wall jet resulted in boundary layer reattachment. With increasing applied peak-to-peak voltage the actuator effectiveness increased. The integrated ramp pressure coefficient improved by 53% with steady actuation at 40kV and 2 kHz. Experiments with unsteady actua-



**Figure 2.21:** Schematics of (a) spanwise and (b) streamwise plasma actuators[23].

tion showed little sensitivity to the reduced frequency in the range of  $f^+ = 0.9 - 8.6$ , suggesting that the plasma actuation did not exploit any flow instability which is often the case in laminar separation control. It was found that the amount of high momentum fluid that is transferred to the near-wall region from the outer boundary layer is what really matters to avoid turbulent separation, since increasing the duty cycle of the unsteady actuation clearly increased the effectiveness. The use of PSVG actuators increased the integrated ramp pressure distribution up to 60% at 40kV and 2kHz, indicating that the momentum transfer by the counter-rotating streamwise vortices was more efficient in mixing the flow. The vortices created an upward velocity in the plane centred between two exposed electrodes and induced a downward velocity above the exposed electrodes. Another study focusing on the control of flow separation by PSVG can be found in Jukes et al.[31].

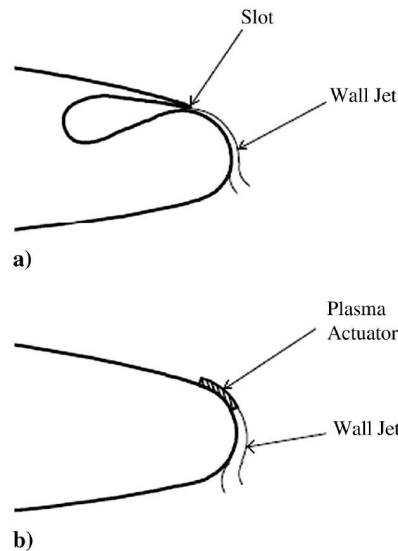


**Figure 2.22:** Sketch for the jet CC airfoil (a) and the PCC airfoil (b)[66].

The idea for the use of plasma actuators on an airfoil with a rounded trailing edge originates from a numerical RANS simulation performed by Zhang et al.[66]. In this study a plasma circulation control (PCC) method was proposed that uses the plasma induced wall jet to shift the trailing edge stagnation point (i.e. changing the Kutta condition), see figure 2.22 for a schematic of the method. The stagnation point is shifted due to postponement of the turbulent separation point

by input of momentum in the near-wall region of the boundary layer. The simulations were performed on a modified NCCR-1510-7607N airfoil with a chord of 1m and a free stream velocity of 10m/s, which yield a Reynolds number of  $6.84 \cdot 10^5$ . Optimization of the position of the plasma actuator resulted in lift coefficient increments  $\Delta c_l$  up to 1.4 at  $\alpha = 0^\circ$  and 0.4 at  $\alpha = 12^\circ$ . In contrast to the two previous papers by He[23] and Schatzmann[56] it was stated that the optimal location of the plasma actuator was slightly downstream of the separation point. However, when the actuator was totally merged in the separated wake of the airfoil it had not enough power to reattach the separated boundary layer.

### 2.3.5 DBD plasma actuators for load control

The use of DBD plasma actuators for active load control on wind turbines has some clear advantages with respect to other methods. The plasma actuator is fully electronic with no moving parts that need maintenance, the response time is very fast (in the order of ms), the mass is very low, the power consumption is low due to the direct conversion of electric energy in kinetic energy and the actuator is very flexible and simple in its use. Additionally, the plasma actuator is non-intrusive and therefore generates no additional parasitic drag. This also reduces the aeroacoustic noise generated by the load control actuator. When comparing the plasma actuators to other actuators it is important to note that it has no complicated structures inside the airfoil, making it easier to manufacture, and it only requires a high voltage source and wires to connect the electrodes. Another feature is the ability to operate in co-flow and counterflow mode by adding an exposed electrode, which allows for more options when controlling local flow.

A primary disadvantage of the plasma actuators is the relatively low momentum input with respect to the flow. It is known that the performance reduces considerably at higher Reynolds numbers. This can also be seen by looking at the free stream velocities used in the papers that were discussed in this chapter, in most cases the values are around or below 10m/s with the exception of leading edge separation cases where the DBD plasma actuators are used to enhance laminar-to-turbulent transition.



# Measurement techniques

Two measurement techniques have been used in order to investigate the potential of plasma actuators to control Kutta condition on the rounded trailing edge model: a force balance with force sensors and Particle Image Velocimetry (PIV). Also a technique to measure the power consumption of a plasma actuator is used. In this chapter the working principle of these three techniques are presented. The first section describes the force sensors, the second the PIV method and the last section discusses a method to measure the power consumption.

### 3.1 Force sensors

For the quantification of the aerodynamic effect of the plasma actuator the aerodynamic forces are measured with force sensors. The type of force sensor used is the KD40s double bending beam sensor from ME-Meßsysteme GmbH, see figure 3.1. The sensor is capable of measuring forces in the range  $\pm 100N$  with a precision of 0.1%.



**Figure 3.1:** An image of the KD40s force sensor.

The force sensor is connected to a National Instruments (NI) Compact Data Acquisition (DAQ) module that converts the analog voltage signal of the force sensor into a digital voltage output. In NI LabVIEW (Laboratory Virtual Instrument Engineering Workbench) the digital signal is translated to a force in Newtons. The 50kHz digital output signal from the module is averaged over a period of 1s to filter out the oscillations in the raw data. Each data point that will be presented in the results of this thesis work is the mean of 10 of these averaged raw data points. This is done to find an indication of the precision of the force measurements. The precision will be expressed by the standard deviation of this set of 10 points, calculated according to the

standard rules for calculation of the standard deviation. For cases where two variables are added or subtracted:

$$\sigma_x = \sqrt{\sigma_A^2 + \sigma_B^2} \quad (3.1)$$

While for multiplication and division:

$$\sigma_x = \mu_x \sqrt{\frac{\sigma_A^2}{\mu_A^2} + \frac{\sigma_B^2}{\mu_B^2}} \quad (3.2)$$

Where subscript x denotes the variable to be calculated, given by a formula depending on the variables with subscript A and B, for example  $x = A \cdot B$  or  $x = A/B$ .

Chapter 4 will discuss how the force sensors are used to measure the lift, drag and pitching moment generated by the airfoil model in the force balance.

## 3.2 Particle image velocimetry

In order to determine the effectiveness of the plasma actuator in controlling the position of the rear separation point, and therefore the circulation and lift, a technique called Particle Image Velocimetry (PIV) is used. This section will discuss the basics of PIV as used for the experimental investigations in this thesis. For more details on the historical development, the measurement technique and applications of PIV readers are referred to Jahanmiri[25].

PIV is a relatively new and successful measurement technique developed and employed for instantaneous velocity field determination in the last decades. PIV allows the measurement of the instantaneous velocity field within a plane, e.g. planar PIV or a three-dimensional space, e.g. tomographic PIV[25]. One of the main advantages of PIV is that it returns at the same time both a quantitative measurement and an intuitive visualization of the flow field around an object.

### 3.2.1 Working principle

The PIV measurement technique is based on the tracking of tracer particles within a fluid flow. A schematic overview of a planar PIV process is depicted in figure 3.2. A typical planar PIV system consists of a seeding system (not displayed) that seeds small tracer particles into the flow, a laser system with laser optics to produce a thin laser sheet, and a digital imaging and recording system consisting of at least one camera with imaging optics.

Tracer particles, which are often referred to as 'seeding', are introduced into the flow. A fundamental property of these particles is that they are required to travel along with the fluid, having a fast response to flow changes and to not alter the behavior of the fluid. When moving through a plane of interest, the particles are illuminated twice by a thin laser sheet, generated by two laser pulses a time-step  $\Delta t$  apart. Simultaneously a camera, placed perpendicular to the light sheet, will record the light scattered by the particles in two frames, corresponding to the two laser light pulses from the laser. The two images,  $I(x, y, t)$  and  $I(x, y, t + \Delta t)$ , contain the specific particle positions.

For processing, the images are commonly divided into small sub-domains, called 'interrogation windows', also shown in figure 3.2. A cross-correlation between the interrogation windows of the

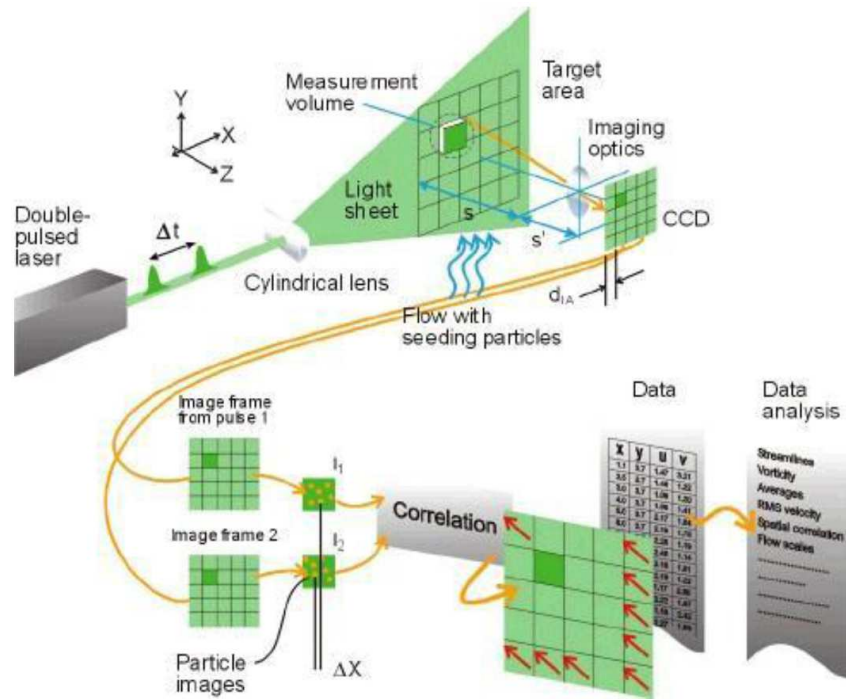


Figure 3.2: Schematic overview of a planer PIV process.

two frames yields the average particle displacement in pixels within such a window, as is indicated in figure 3.2. Evaluating the particle displacement with cross-correlation has the advantage that no explicit particle detection is required, it is the overall movement of the particles that determines the displacement. By taking into account the magnification factor, the pixel displacement vector can be expressed in particle displacement in meters. Furthermore, by using the time separation between the two light source pulses,  $\Delta t$ , the velocity vector can be determined. Repeating this process for all interrogation windows allows us to reconstruct the instantaneous velocity vector field.

With the camera(s) and laser placed outside the flow only the particles are present in the flow. Taking into consideration their requirement to not alter the fluid properties, this measurement technique is considered to be non-intrusive. Furthermore, PIV measures instantaneous velocity fields with a high spatial resolution, while most other velocity measurement techniques can only measure the instantaneous velocity at a single point, as for example hot wire anemometry (HWA) and laser doppler velocimetry (LDV). Even though the temporal resolution of PIV is increasing, it is still limited by the camera acquisition frequency or laser repetition rate. Additionally, the storage of the camera puts restrictions on the recording time.

### 3.2.2 Tracer particles

The tracer particles inserted into a fluid flow act as a tracking device and are typically employed with PIV or LDV. As described above, the particles are required to follow the flow accurately without altering the fluid flow characteristics. Consequently, the tracer particles characteristic response time has to be smaller than the smallest characteristic time scale of the fluid flow. Moreover, for the illuminated particles to be detectable by cameras, they should scatter enough light towards the camera.

### Mechanical properties

The accuracy of PIV depends on the capability of tracer particles to actually follow the motions of the flow. This is optimized when the velocity difference between the tracer particles and the fluid is very small. The velocity difference or slipping velocity, as illustrated in figure 3.3, is  $\hat{V} = \hat{U}_p - \hat{U}_f$ , where  $\hat{U}_p$  is the particle velocity vector and  $\hat{U}_f$  is the fluid velocity vector.

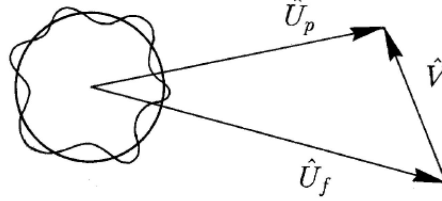


Figure 3.3: The relative particle motion, from Melling[40].

The exact particle motion in a moving fluid is rather complicated, but an accepted model to (qualitatively) describe the motion of seeding particles is Hinze's model[2]. The model describes the balancing of forces on a particle.

$$\frac{\pi}{6} d_p^3 \rho_p \frac{dU_p}{dt} = F_{st} + F_p + F_f + F_u \quad (3.3)$$

where  $d_p$  is the particle diameter,  $U_p$  is the velocity of the particle,  $\rho_p$  is the density of the particle material. The force terms on the right hand side are the viscous drag given by Stokes law ( $F_{st}$ ), pressure gradient force ( $F_p$ ), the resistance of an inviscid fluid to acceleration of the seeding particle ( $F_f$ ) and the Basset history integral that represents the drag force associated with unsteady motion ( $F_u$ ), respectively. For very small tracer particles as in the case of PIV the first part of the quasi steady viscous term (Stokes drag) dominates the right hand side of the equation[54]. The Stokes force is given by:

$$F_{st} = -3\mu d_p \hat{V} \quad (3.4)$$

where  $\mu$  is the dynamic viscosity coefficient.

### Electrostatic effects

Equation 3.3 is valid under a number of assumptions. One of the assumptions states that the tracer particles are spherical, which is a valid assumption for small droplets and disperse solid particles of uniform size. Another assumption is that external body forces are negligible. However, the ionization of the fluid particles during the plasma actuation results in tracer particles getting charged by ion impact. Under the influence of the electrostatic forces generated by the electric field the trajectory of the tracer particles can be affected. Therefore an additional force, the electrostatic force  $F_{el}$ , has to be added to the right hand side of equation 3.3. The electrostatic force can be described as a combination of the net charge level obtained after a certain exposure time to an electric field,  $q_n$ , and the electric field strength,  $E_0$ :

$$F_{el} = q_n E_0 \quad (3.5)$$

As a particle collects more and more charge, it develops its own electric field, and the charging process slows down due to growing repulsion. The maximum surface charge is reached when the

net electric field at the particle surface equals zero. According to Chui[10] and Artana et al.[2] this saturated charge level  $q_n$  is given by:

$$q_n = \left[ \frac{3\epsilon_r}{\epsilon_r + 2} \right] \epsilon_0 \pi d_p^2 E_0 \quad (3.6)$$

with  $\epsilon_r = \epsilon/\epsilon_0$  as the relative permittivity or dielectric constant and  $\epsilon_0$  as the permittivity of vacuum equal to  $8.854 \cdot 10^{-12}$ F/M. An upper limit of the attainable charge for droplets of dyethelene-glycol/water based tracer particles as used in the current work (relative dielectric constant  $\epsilon_r = 31.7$ ) is obtained with:

$$q_n = 2.82\epsilon_0 \pi d_p^2 E_0 \quad (3.7)$$

Considering this upper limit it can be seen that the electrostatic forces are proportional to the surface of the particle and to the square of the electric field. An inspection of equations 3.3 and 3.4 for small particles corrected with the electrostatic forces, shows that these last forces will only be important when the slipping velocity is very low. For instance considering a particle in air of  $d_p \approx 1\mu m$  and an electric field of  $E_0 \approx 10^6 V/m$  the ratio of the viscous to the electric forces is:

$$\frac{F_{st}}{F_{el}} = \frac{-3\mu d_p \hat{V}}{2.82\epsilon_0 \pi d_p^2 E_0^2} \approx -2.19\hat{V} \quad (3.8)$$

The ratio is directly dependent on the slipping velocity of the particles  $\hat{V}$  and it can be said that the Stokes forces are significantly larger than the electric forces at electric field strengths below  $E_0 \approx 10^6 V/m$ , except for low values of the slipping velocity.

The electric field for the plasma actuator design used throughout the experiments in this work is determined by solving the Poisson equation of the electric potential. The analysis is described in more detail in appendix A and the result is shown in figures 3.4 and 3.5. These figures show a very high electric field strength between the two electrode edges facing each other and a fast decaying strength when moving away from the electrodes.

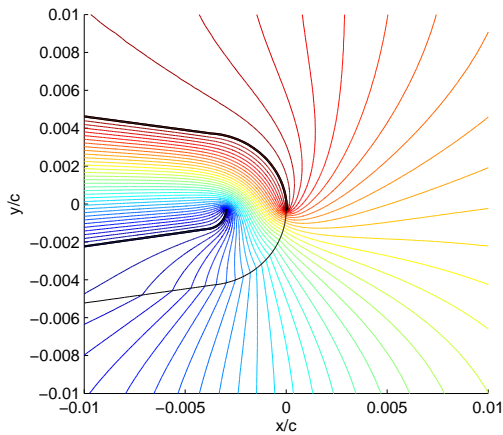


**Figure 3.4:** Electric potential distribution of the plasma actuator gap at the trailing edge and the maximum applied peak-to-peak voltage of 35kV.

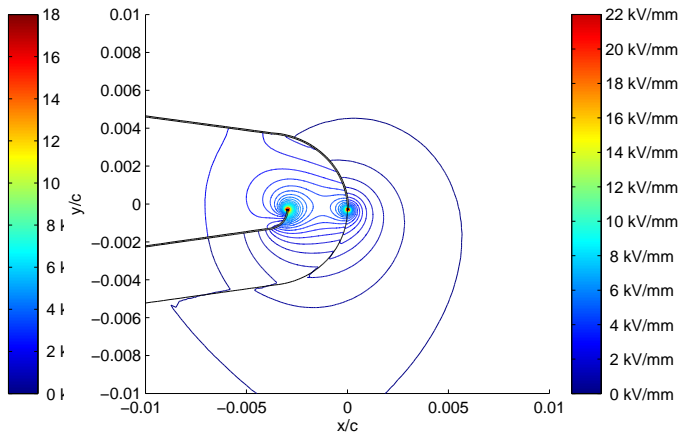


**Figure 3.5:** Electric field strength of the plasma actuator gap at the trailing edge and the maximum applied peak-to-peak voltage of 35kV.

The conclusion from this analysis is that near the exposed electrode's trailing edge, within a circle with a radius of 2.5mm, the electrostatic force dominates the particle motion. The first visible low level contour line that can be seen in figure 3.5 belongs to  $E_0 = 0.5 \cdot 10^6 V/m$  and the second one to  $E_0 = 1.0 \cdot 10^6 V/m$ . Moving away from the trailing edge the electrostatic force quickly decays and is several times smaller than the viscous term and at some point the electrostatic forces can be neglected. It should also be noted that the figures represent the potential and electric fields at the time instant where the maximum electrode potential is reached during an actuation cycle and for the highest peak-to-peak voltage used in this work (35kV).

The effect of the electrostatic forces is also investigated in an experimental way by Zito et al.[67]. They compared the calculated velocity field near the edge of the exposed electrode using PIV with the measured velocity distribution using a glass pitot tube. The pitot measurements showed good agreement with the PIV data, with slight discrepancy between the vertical location of the data points. The offset between the two measurements was most likely attributed to the 1mm diameter of the pitot tube over which the pressure measurement was averaged, as well as the initial manual alignment. Stephen et al.[58] performed a similar experiment with independent pitot tube measurements showing that the particle-free flow is in good agreement with the PIV data, concluding that there is no significant influence on motion of the the seeding particles.

For the current research the overall flow effect of the plasma actuator is important and no calculated data from near the exposed electrode's edge is used in the evaluation of the results. However, care should be taken when interpreting the results, since the effect of the electrostatic force is clearly present close to the trailing edge.

### Scattering properties

Besides mechanical requirements the tracer particles also have to scatter enough light towards the camera for them to be captured. The light scattering depends on several factors, such as the ratio of the refractive index of the particles to that of the surrounding medium, their size, shape and orientation. The shape and orientation are hard to control, but the average size and refractive index of the particles can be influenced, since these depend on the type of tracer particles that is used. Furthermore, the light scattering also depends on polarization and observation angle. For spherical particles with diameters,  $d_p$ , larger than the wavelength of the incident light  $\lambda$ , Mie's scattering theory can be applied. Figure 3.6 shows the scattered light intensity as a function of the scattering angle for a particle of  $1\mu m$  diameter.

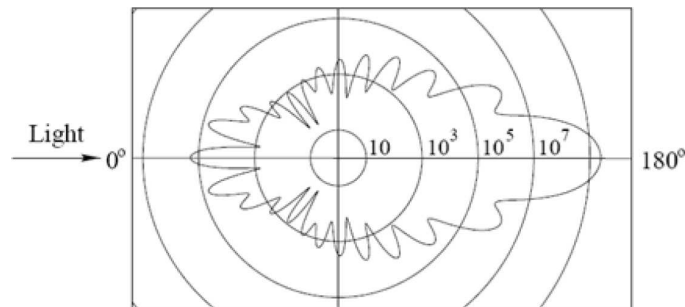


Figure 3.6: Scattered light intensity as a function of the scattering angle for a  $1\mu m$  oil droplet.

The scattered light intensity has a maximum at  $180^\circ$  and another peak at  $0^\circ$ . At  $90^\circ$ , which is the typical observation angle in PIV experiments, a minimum is found. Due to this minimum it is important to maximize the scattered light by selecting particles with a high refractive index and

the largest size possible, limited by their capability to follow the flow accurately and, in the case of plasma actuation, the effect of the electrostatic force acting on them. Other improvements can involve the light source, both in wavelength as in power. However, these variables are fixed most of the time due to expensive lasers and camera sensors and optics being optimized for one specific wavelength.

### 3.2.3 Illumination

For illumination of the tracer particles lasers are commonly used in PIV. This is because they emit monochromatic light with a high energy density which can easily be manipulated by using optics to form thin light sheets. The laser sheet illuminates the particles twice with a short time-step apart by emanating two separate pulses. The pulses are required to be short enough to avoid particle image streaks on the recorded images. The laser pulses leave the laser as a narrow cylindrical beam of several mm in diameter. Through a set of mirrors and lenses the laser beam is deflected, widened and focused to become a wide and thin laser sheet at the plane of interest near the model. The laser sheet has to be thin enough such that only particles in a plane are illuminated. Another requirement is that the energy of the light source beam is high enough to allow sufficient scattering from the particles such that they can be detected by the cameras.

The light sheet formation process is schematically shown in figure 3.7. The beam is focused by a convex cylindrical lens to minimize the laser sheet thickness at the point of interest. A cylindrical lens in front or behind the focusing lens expands the laser sheet to obtain the required width to cover the field of view. The strength of the lenses depends on the focal length  $f_2$  and the distance between the lens and the point of interest  $L$ .

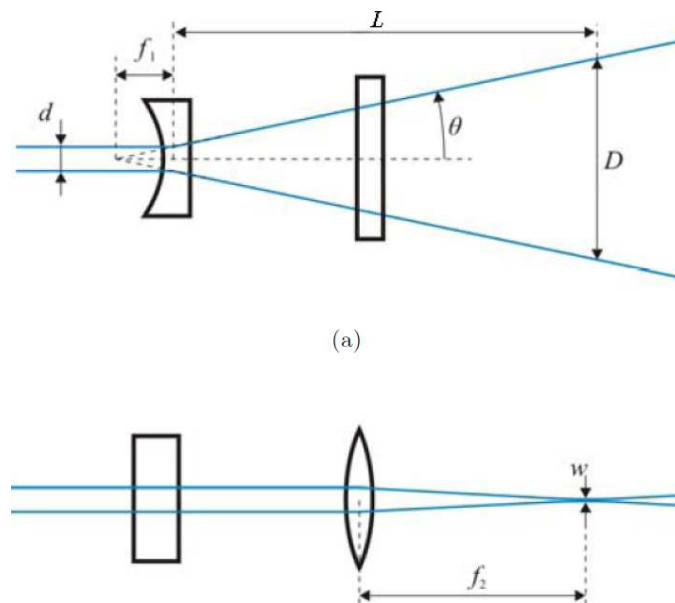


**Figure 3.7:** Light sheet formation optics: a) side view showing the expansion of the laser beam and b) top view showing beam focus at measurement location [54].

### 3.2.4 Particle imaging

The image of the tracer particles in the light sheet is focused on an image sensor of the camera, the imaging plane, by using a photographic lens. The imaging system, which is usually a

Charge Couple Device (CCD) or a Complementary Metal Oxide Semiconductor (CMOS) camera, is characterized by its focal length  $f$ , aperture number  $f_{\#}$ , and the image magnification  $M$ . The aperture number  $f_{\#}$  is defined as  $f/D$ , where  $D$  is the aperture diameter. The image magnification is defined as:

$$M = \frac{d_i}{d_o} = \frac{\text{sensor size}}{\text{FOV}} \quad (3.9)$$

where  $d_i$  is the image distance and  $d_o$  the object distance. The magnification factor can also be expressed as the ratio between the image sensor size (fixed by the camera's number of pixels times the pixel size) and the field of view (FOV). The focal length, image and object distance are related through the lens equation.

$$\frac{1}{f} = \frac{1}{d_i} + \frac{1}{d_o} \quad (3.10)$$

The applied aperture lenses are finite and therefore diffraction limited, which means that point sources will appear as Airy disks and rings on the image sensor. The diffraction pattern of a particle is shown in figure 3.8 and the size of such a disk  $d_{diff}$  can be approximated by:

$$d_{diff} = 2.44f_{\#}\lambda(M + 1) \quad (3.11)$$

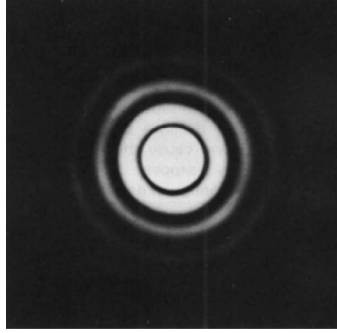


**Figure 3.8:** Airy diffraction pattern from a  $1\mu\text{m}$  diameter particle, figure taken from Scarano[54].

Then the minimal image particle diameter, as observed on the image sensor, is determined by:

$$d_{\tau} = \sqrt{(Md_p)^2 + (d_{diff})^2 + (d_{blur})^2} \quad (3.12)$$

In this equation the first term is due to a geometric optics effect (particle magnification by the lens) and the last term,  $d_{blur}$  due to a defocusing effect. Finally, the depth of focus  $\delta_z$  can be approximated by:

$$\delta_z = 2f_{\#}d_{diff}\frac{M + 1}{M^2} = 4.88f_{\#}^2\lambda\left(\frac{M + 1}{M}\right)^2 \quad (3.13)$$

For small particles of  $d_p \leq 1\mu\text{m}$  the minimal image particle diameter is typically dominated by the diffraction limit  $d_{diff}$ , although  $d_{diff}$  can be controlled to some extent by the aperture number  $f_{\#}$ , controlling the image light intensity. Good particle imaging may be found from a compromise between under sampling and spatial resolution. An optimal particle image is around 2-2.5 pixels[25]. A smaller particle image can indicate only the presence of a particle and will not results

in an accurate particle position due to the absence of intensity distribution in neighbouring pixels (i.e. under sampling). A too large value for  $f_{\#}$  will however lead to overlap of the particle images, due to increased diffraction and depth of focus, decreasing the image contrast and thereby the spatial resolution of the measurement.

A significantly large aperture diameter is required to achieve sufficient light from all the particles, and also to decrease the size of the diffraction pattern. However, a big aperture diameter decreases the depth of field, which is needed to have all the illuminated particles within the laser sheet in focus.

To accurately determine the velocity vectors from PIV measurements a proper choice of the seeding density and pulse separation time is required. In order to achieve an error in the particle displacement of 1-2%, the pulse separation time has to be chosen such that the particle displacement is approximately 10 pixels. Obtaining this pixel shift will result in a high number of particle pairs, meaning that the majority of the particle imaged remain in the same window during both exposures. Thereby the particle displacement can be determined accurately from the correlation peak. Considerably smaller displacements may be too small to correctly establish the velocity vectors and with larger displacements too many particles will have moved out of the window. As far as the seeding is concerned, the distribution should be uniform. Furthermore, according to Scarano[54] there should be at least 10 tracer particles in an interrogation window. Lower seeding density would result in individual particle tracking, which would probably not be representative for the considered flow field. On the other hand very high seeding density would make it difficult to distinguish the individual particles.

### 3.2.5 Image analysis

The final step in the PIV process is the image recording and processing. This section will discuss the recording camera, the acquisition mode, image pre-processing and the process to obtain the velocity field data.

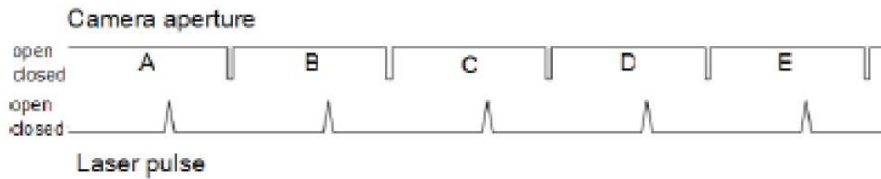
#### Image recording

The particle images are recorded on a CCD or CMOS sensor. A CCD consists of a two-dimensional array of pixels (size  $O(10^{-6})m$ , on a Cartesian grid and have a typical size of several mega-pixels. During exposure the pixels are exposed to a light intensity which is converted into electrons. The accumulated charge is read out sequentially on a row-by-row basis by a charge to voltage converter and digitized by an A/D converter. The readout process is limited to 10-20MHz allowing only for frames in the order of 10-30Hz. For fast recording, up to several kHz, CMOS sensors are used. The CMOS sensors are based on the active pixel sensor (APS) technology in which, in addition to the photo-diode, a readout amplifier is incorporated into each pixel. This converts the charge accumulated by the photo-diode into a voltage which is amplified inside the pixel and then transferred in sequential rows and columns to further processing circuits[48]. Together with highly parallel readout electronic storage devices this allows for the recording and handling of several thousand frames per second (3000 on full sensor size, up to 10000 on reduced sensor size) at acceptable noise levels. Cameras can have memory card up to 16Gb on board to store the large amount of data, recorded within seconds.

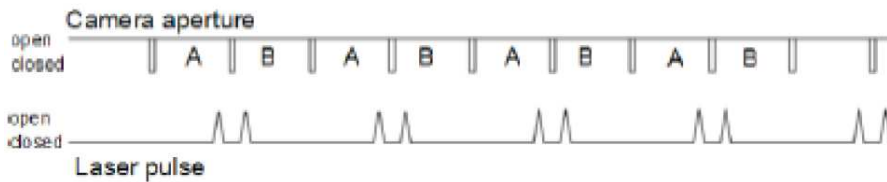
#### Image acquisition mode

Based on the available PIV equipment used, image acquisition can be performed on two different temporal scales. Low-frequency acquisition is used for obtaining statistically uncorrelated data

and visualization of the instantaneous flow fields. High-frequency acquisition, referred to as time-resolved PIV (TR-PIV), allows recording a several kHz and for accurate flow tracking during a specific time period. Besides obvious equipment differences, such as laser repetition rate and camera recording frequency, there is a between the two methods in camera-laser synchronization. The conventional double-frame acquisition mode based on the frame straddling technique is shown in figure 3.9(b). In this mode the image pairs are acquired at a low frequency and every set is acquired with two laser pulses a  $\Delta t$  apart. For data acquisition at high frequencies also the single frame mode can be selected, figure 3.9(a). In this case the images are acquired at a fixed frequency and subsequent images are taken as an image pair. In this case the laser repetition rate and the camera recording rate are set to the equivalent of the desired  $\Delta t$  separating the image pairs.



(a)



(b)

Figure 3.9: PIV acquisition modes: a) single frame b) double frame, figure from Raffel[48]

## Preprocessing

Recorded images are preprocessed before performing actual cross-correlation. During this procedure the minimum intensity of each pixel, based on a small set of frames, is subtracted from all frames in the data set in order to reduce the bright spots due to surface reflections of the laser light on the model. The resulting images are then used for further processing.

## Image processing

The processing of the acquired images is based on a cross-correlation between interrogation windows resulting from the image pairs, as briefly discussed in section 3.2.1 and figure 3.2. During evaluation of the image pair, containing the specific particle positioning at time  $t$  and  $t + \Delta t$ , are subdivided into smaller windows, the interrogation windows. The interrogation window size is chosen such that it contains at least ten tracer particle images[54]. An interrogation window consists of  $N \times N$  pixels. The intensity of the scattered light by the particles contained in the interrogation window of the first image,  $I(i, j, t)$ , is determined. Subsequently a window of the same size and intensities is shifted over the second image and the intensities corresponding to the second image,  $I(i + x, j + y, t + \Delta t)$ , are determined. After that the cross-correlation between the particles in the two images is performed according to:

$$R_{II} = \sum_{i=-K}^K \sum_{j=-L}^L I(i, j, t) I(i + x, j + y, t + \Delta t) \quad (3.14)$$

A high value of  $R_{II}$  corresponds to a close resemblance between the particles inside the two interrogation windows and the cross-correlation peak location indicates the shift for which particles in the first image match with the particles in the second image, as shown in figure 3.10.

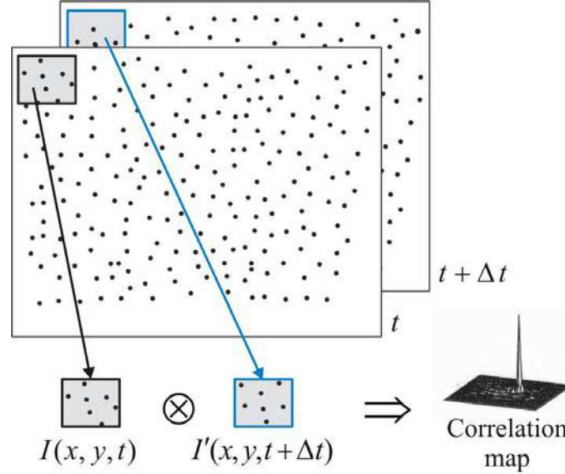


Figure 3.10: Image interrogation windows and cross-correlation map, figure from Scarano[54]

The position of the peak determines the average displacement of the particles over the time-step  $\Delta t$  separating the image pair. To obtain a distinct peak the signal-to-noise ratio should be high. When the particle image diameter are too large, the difference between the noise level and the measurement becomes so small that the measurement uncertainty increases. In cases where the particle image diameter is smaller than a pixel on the camera sensor the determined displacement will be biased towards integer values (i.e. pixel-locking).

To obtain a high number of imaged particles pairs in the same interrogation window the window size should be as large as possible. However, a large window size results in a poor spatial resolution. To increase the spatial resolution and maintain a high signal-to-noise ratio corresponding to large window sizes, a multi-pass interrogation with offset can be applied. In the first pass with large window size the local averaged displacement is determined. The results from this initial interrogation will be used as predictor. In the following interrogation the window size is reduced in all directions. Based on the predictor the interrogation area of the second image is given an offset to maximize the number of particle matches[55]. This allows to obtain a high number of particle images and a high spatial resolution. Applying an overlap in the interrogation windows can further increase the spatial resolution.

### Data processing

The velocity fields obtained from the image processing can be used for data processing. The velocity fields are represented by a large matrix containing the velocities in the FOV ((x,y) for planar PIV and (x,y,z) for tomographic PIV). The velocity fields can be elaborated, for instance with MATLAB, to obtain flow field properties (vorticity, streamlines, etc.) and field statistics (average velocity, rms).

### 3.3 Power consumption

The applicability of the plasma actuator for load control will also depend on the power consumption of the device. It is therefore important to determine the power consumption of the actuator. Measuring the power consumption of DBD plasma actuators is found to be a challenge due to the characteristics of the actuator current signal. Micro-discharges generate high-amplitude, high-frequency current spikes superimposed on a low-amplitude low-frequency current. This section will discuss a method that can be used to measure/calculate the power consumption.

#### 3.3.1 Integrating capacitor method

The power consumption measurement/calculation method used in this report is based on the work of Ashpis[3]. In this report an oscilloscope is used to determine the actuator power consumption according to the monitor capacitor method. In this method, an integrating capacitor with a known capacitance is used. It is placed in series between the covered electrode and the ground, as can be seen in figure 3.11. The method is based on the measurement of the voltage over the capacitor and comparing it to the applied voltage over the electrodes of the plasma actuator.

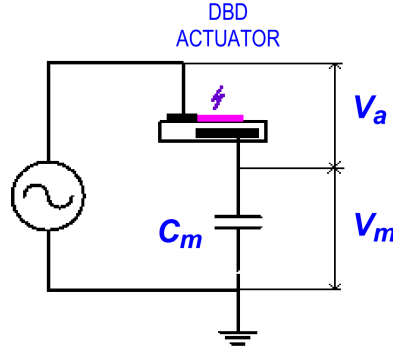


Figure 3.11: Electric circuit diagram of the monitor capacitor method.

The capacitor capacitance value  $C_m$  is chosen to be large compared to the capacitance of the DBD actuator without plasma discharge (sometimes called 'cold' capacitance). Since the capacitance of typical actuators used in published studies is very low (5pF to 200pF), typical monitor capacitor are selected with a value between 10nF and 330nF. The capacitance is usually selected to provide a voltage that is adequately low for the measurement by the oscilloscope. The monitor capacitor does not have to withstand high voltages, typical values are smaller than  $\pm 15V$ . The capacitance of the monitor capacitor is desired to be constant over the operating voltage and frequency range of the actuator.

The capacitor based charge method is described as follows; the instantaneous charge on the monitor capacitor is:

$$Q_m(t) = C_m \cdot V_m(t) \quad (3.15)$$

And the current through the capacitor is:

$$I_m(t) = C_m \frac{dV_m(t)}{dt} \quad (3.16)$$

Where  $Q_m$  is the charge on the capacitor,  $V_m$  the voltage across the capacitor,  $C_m$  the capacitor capacitance (assumed to be constant) and  $I_m$  the current through the capacitor. Since the current

through the monitor capacitor must be identical to the current through the actuator (since they are in series),  $I_m = I_a$ , the instantaneous power dissipated by the actuator is:

$$P_a(t) = V_a(t) \cdot I_a(t) = V_a(t) \cdot C_m \frac{dV_m(t)}{dt} \quad (3.17)$$

Where  $V_a$  is the voltage across the actuator and  $I_a$  the current through the actuator. The average power over a time period  $T$  is obtained by integration of equation 3.17 and a change of variables:

$$\bar{P}_a = \frac{1}{T} \int_0^T V_a(t) \cdot C_m \frac{dV_m(t)}{dt} dt = \frac{1}{T} \int V_a \cdot C_m dV_m = \frac{1}{n \cdot T} \oint_n V_a dQ_m \quad (3.18)$$

In which  $n$  represents the number of cycles, usually set to one. The instantaneous capacitor charge  $Q_m$  and the instantaneous actuator voltage  $V_a$  plotted against each other generate a so-called Lissajous curve in the  $Q_m - V_a$  plane. Equation 3.18 shows that the area inside the closed Lissajous curve divided by the AC cycle period is equal to the actuator power consumption.

### 3.3.2 Data smoothing

The choice is made to use a least squares filter based on the work of Savitzky and Golay[53] to prepare the raw data for further post-processing. This method enhances the signal-to-noise ratio of the raw data signal by a signal smoothing algorithm. The underlying idea is use of a least squares fit of a small set of consecutive raw data points to a polynomial and take the calculated central point of the fitted polynomial curve as the new smoothed data point. Savitzky and Golay state that a set of integers can be derived and used as weighting coefficients to carry out the smoothing operation. The use of these weighting coefficients, known as convolution integers turn out to be exactly equivalent to fitting the data to a polynomial. However, the use of a constant set of integers for all sub-sets of raw data points instead of calculating the coefficients of a polynomial for every sub-set, makes it computationally more effective and much faster. The smoothed data point  $(y_k)_s$  by the Savitzky-Golay algorithm is given by the following equation:

$$(y_k)_s = \frac{\sum_{i=-m}^m A_i \cdot y_{k+i}}{\sum_{i=-m}^m A_i} \quad (3.19)$$

Where  $A_i$  are the convolution integers or the weighting coefficients. Many sets of convolution integers can be used depending on the filter width and the polynomial degree. The filter width is expressed by  $2m + 1$ . For the smoothing of the raw power data in this report a quadratic smoothing is applied with a filter width of 9 points, corresponding to  $m = 4$ . The convolution integers corresponding to these settings are given in figure 3.12a.

Figure 3.12b shows the selection sequence of the data sub-sets in the algorithm, the dashed ellipses show the data sub-sets and the circles show the location of the new smoothed data point. As a result of the smoothing algorithm the new data set is reduced by a  $2m$  points. The smoothing algorithm can be applied multiple times until a desired smoothness is reached. The smoothing effect of the Savitzky-Golay algorithm is not as aggressive as, for example, a moving average method and the loss/distortion of the vital information is comparatively limited. However, it should be stressed that because of the algorithm a part of the original information is lost or distorted. In this report it is assumed that the loss/distortion of information is acceptable with respect to the gain in smoothness of the data.

Data Set Point $i$	-4	-3	-2	-1	0	1	2	3	4
Weight $A_i$	-21	14	39	54	59	54	39	14	-21

(a) Data points and corresponding weights



(b) Data set selection sequence

**Figure 3.12:** Overview of the smoothing algorithm; a) convolution integers with respect to the sub-set data points; b) data set selection sequence, the dashed ellipses show the data sub-sets and the circles show the location of the new smoothed data point.

## Experimental set-up

An experimental investigation has been conducted to study the ability of the plasma actuators to change the total circulation by control of the rear separation point on the rounded trailing edge model. Additionally a reference case with Gurney flaps and a case with leading edge actuation on a flap are investigated. The design and set-up of these experiments are described in this chapter. In the first sections the airfoil model, flow facility and high voltage supply are discussed, followed by a description of the force measurement and PIV measurement set-ups. The latter two include a detailed explanation on how the data in the subsequent chapters is obtained, together with a list of the configurations and variables that are investigated in the experiments.

### 4.1 Model design

The used airfoil is a modified version of a NACA64-2-A015 airfoil employing a circular trailing edge as shown in figure 4.1.

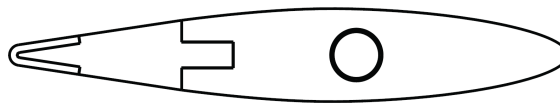
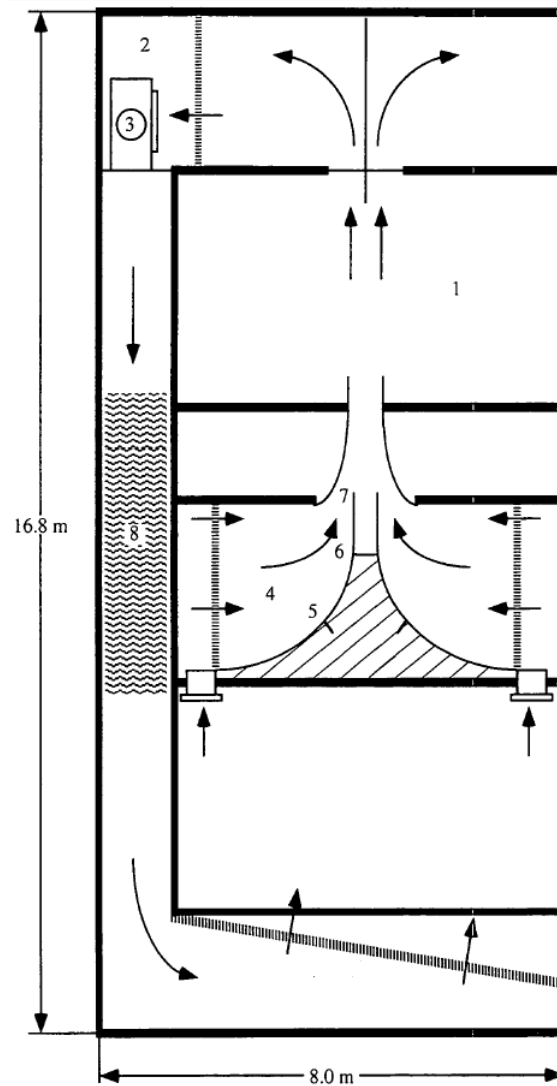


Figure 4.1: Modified NACA64-2-A015 airfoil with a circular trailing edge.

The airfoil's main body is milled out of solid aluminium while a removable trailing edge is made of Polyoxymethylene (POM) to accommodate the high voltage installation of the covered electrode of the plasma actuator. The curved trailing edge part is made out of PolyMethylMethAcrylaat (PMMA or Plexiglas®) and acts as a dielectric for the plasma actuator. This part has a thickness of 3mm and can be removed from the model in order to place the covered electrode. The original airfoil had a chord of 240mm and a thickness-to-chord ratio of  $t/c=0.15$ . The modified airfoil has a reduced chord of 217mm and consequently an altered thickness-to-chord ratio of  $t/c=0.166$ . Besides the reduction in chord and the rounded trailing edge, the aft part of the modified airfoil, between approximately  $x/c=0.69$  and  $x/c=0.985$ , has a constant slope. The span,  $b$ , of the model is 560mm. At approximately  $x/c=0.02$  a pair of roughness strips (carborundum grains) are applied on both sides of the airfoil in order to force transition.

## 4.2 Flow facility

The experimental investigation is carried out in the vertical (V-tunnel) low turbulence tunnel located in the Low Speed Laboratory of the Technical University in Delft. The V-tunnel is an open jet configuration with a circular test section and vertical inflow from below, a schematic overview is given in figure 4.2.



**Figure 4.2:** Overview of the V-tunnel: 1) measuring room, 2) fan room, 3) fan, 4) settling chamber, 5) & 6) spike, 7) contraction, 8) sound damper.

The contraction ratio is about 100:1. The diameter of the exit section is 0.6m. Due to the high contraction ratio between the settling chamber and the test section the quality of the airflow is very high in terms of the turbulence level, which is lower than 0.1%. The maximum achievable velocity is 45m/s. The free stream velocity is determined from the dynamic pressure measured with a pitot tube at the exit section.

## 4.3 High voltage supply

The plasma actuator is powered by a TREK 20/20C HV amplifier ( $\pm 20\text{kV}$ ,  $\pm 20\text{mA}$ ,  $1000\text{W}$ ), capable of generating a range of waveforms with a maximum peak-to-peak voltage of  $40\text{kV}$  (maximum amplitude of  $20\text{kV}$ ). The maximum frequency depends on the load and slew rate of the waveform. For the maximum voltage and frequency used in this report,  $35kV_{pp}$  and  $1.5\text{kHz}$ , it is found that the produced signal shows no distortion. The amplifier is controlled by LabVIEW through two NI-DAQ modules.

## 4.4 Force measurements

In order to quantify the effect of the plasma actuator a force balance is used. This section discusses the force balance set-up that is designed and how the forces are calibrated and calculated. Additionally some important wind tunnel corrections are discussed that follow from the use of an open jet wind tunnel. Finally, this section shows the experimental test matrix of all experiments where the aerodynamic forces generated by the airfoil model are measured.

### 4.4.1 Experimental set-up of the force balance

The aerodynamic forces (lift, drag and pitching moment) are measured with a force balance and force sensors (as discussed in section 3.1), see figure 4.3 for a schematic view of the set-up.

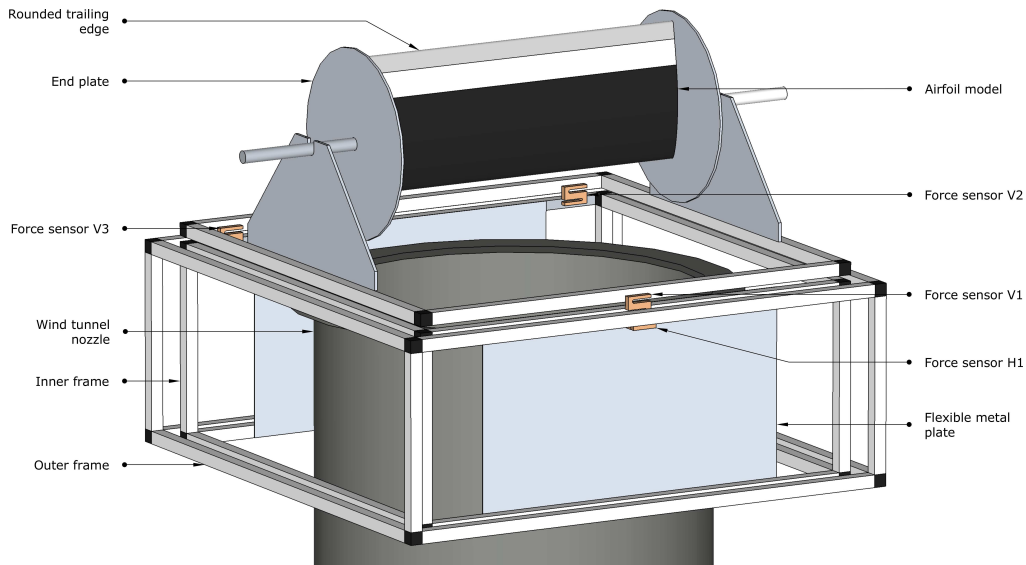


**Figure 4.3:** A schematic view of the force balance set-up

The force balance is placed over the wind tunnel nozzle and the airfoil is mounted on top of it. The balance has an inner and an outer frame. The outer frame is considered to be rigid while the inner frame consists of two flat plates and a frame on top of it. It is assumed that the plates bend without any friction, such that the top of the inner part of the balance moves freely in the direction perpendicular to the free stream, the direction of the lift force. A force sensor (H1) is mounted such that it holds this moving part of the balance in place and therefore it measures the lift force directly. The model is mounted onto this 'moving' part of the balance by three force sensors, two on one side (V2 and V3) and one (V1) on the opposite side. These three sensors

essentially carry the airfoil model and the structure that holds the airfoil in place, the top part of the inner frame.

#### 4.4.2 Force calibration and calculation

By the use of a NI CompactDAQ module and LabVIEW the voltage output signal from the sensors is transferred into a force in Newtons, as discussed in section 3.1. From the four force sensors the lift (L), drag (D) and pitching moment (M) are calculated. Figure 4.4 shows a free body diagram (FBD) of the test set-up.

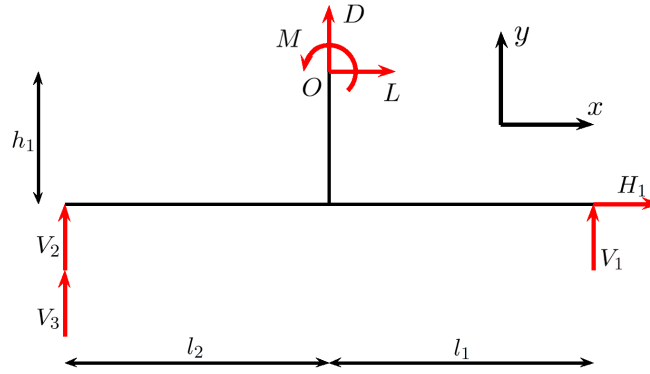


Figure 4.4: A schematic free body diagram of the test set-up used.

The figure shows a simplified side view of the top part of the inner frame. The force  $H_1$  is measured by the force sensor that holds the inner frame in place, whereas forces  $V_1$ ,  $V_2$  and  $V_3$  are measured by the three force sensors that carry the top part and the airfoil.  $L$ ,  $D$  and  $M$  are the aerodynamic forces generated by the airfoil at the position where the airfoil is mounted onto the balance (point  $O$ ). The lift follows directly from the summation of the forces in  $x$ -direction:

$$\sum F_x^{\rightarrow+} : \quad L + H_1 = 0 \quad (4.1)$$

$$\Rightarrow L = -H_1 \quad (4.2)$$

The drag follows from the sum of the forces in  $y$ -direction:

$$\sum F_y^{\uparrow+} : \quad D + V_1 + V_2 + V_3 = 0 \quad (4.3)$$

$$\Rightarrow D = -V_1 - V_2 - V_3 \quad (4.4)$$

The pitching moment at point  $O$  can be found by summation of all moment contributions around point  $O$ , as follows:

$$\sum M_O^{\curvearrowright+} : \quad M + h_1 \cdot H_1 + l_1 \cdot V_1 - l_2 \cdot V_2 - l_2 \cdot V_3 = 0 \quad (4.5)$$

$$\Rightarrow M = -h_1 \cdot H_1 - l_1 \cdot V_1 + l_2 (V_2 + V_3) \quad (4.6)$$

In order to find the pitching moment around the quarter chord point  $M_{c/4}$ , the moment and forces acting at point  $O$  are translated along the chord. Figure 4.5 shows a schematic view of the

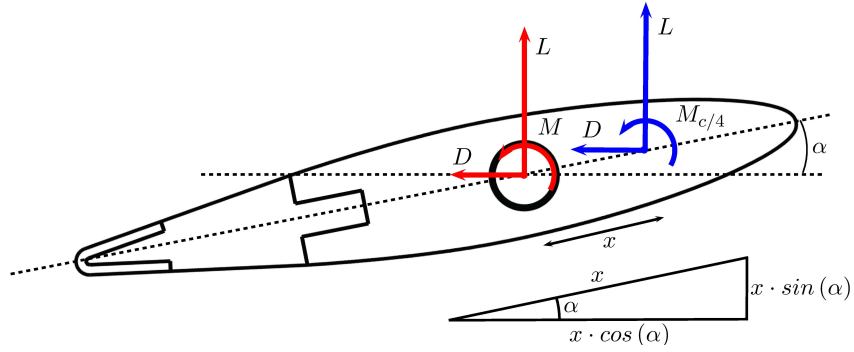


Figure 4.5: A schematic free body diagram of the test set-up used.

translation in the case when the airfoil is under an angle of attack  $\alpha$ . The triangle at the bottom of the figure shows how the arm lengths of the forces are determined.

The lift and drag force can be translated without any change. The new pitching moment can be found by summation of all moment contributions around point  $c/4$ :

$$\sum M_{c/4}^{\wedge+} : \quad M_{c/4} = M - x \cdot \sin(\alpha) \cdot D - x \cdot \cos(\alpha) \cdot L \quad (4.7)$$

Where  $x \cdot \sin(\alpha)$  is the arm length to the force  $D$  and  $x \cdot \cos(\alpha)$  the arm length of force  $L$ . The distance  $x$  is found to be 2.775cm.

Another step in finding the right pitching moment is to take into account a correction for the static moment created by the angle of attack at zero velocity. The pitching moment is found to change linearly with the angle of attack. The following equation gives the new pitching moment:

$$M'_{c/4} = M_{c/4} - (0.0196\alpha - 0.0045) \quad (4.8)$$

In section 4.4.3 a final correction will be discussed, considering a wind tunnel effect.

All sensors are calibrated by subtraction of the static forces measured in rest at zero free stream velocity and zero angle of attack. Before each run the force sensors are calibrated such that all measured forces and the deduced moment are zero. Before and at the end of each run an extra data point is saved, both at the same angle of attack and no free stream velocity. The average forces and moment of these two points is subtracted from all raw data points in order to compensate for any error produced by the relaxation of the force sensors.

#### 4.4.3 Wind tunnel corrections

When testing in closed and/or open jet wind tunnels it is necessary to apply corrections to the measured data since the flow conditions in the test section are not the same as those in free flow. A large amount of literature is available on wind tunnel corrections for both closed and open jet testing. The current study is performed in an open jet test facility and therefore the focus will be on corrections applicable to these wind tunnels.

The main difference is that the jet flow in an open jet tunnel is free to expand. With this property it is assumed that important corrections for closed jet tunnels, such as solid and wake blockage

and horizontal buoyancy, can be neglected. Solid and wake blockages are caused by the model and the wake blocking the cross sectional area of the wind tunnel. These blockages locally increase the velocity of the flow and that leads to incorrect data. Horizontal buoyancy results from the thickening of the boundary layer along the wind tunnel walls in downstream direction. This causes the effective cross sectional area of the wind tunnel to decrease gradually, increasing the flow and decreasing the static pressure along the test section. The pressure gradient will give incorrect forces on the model. The free expansion of the jet in an open tunnel is assumed to compensate for the blockage effects created by these phenomena, resulting in a very limited effect.

The corrections that are considered in this study are down-wash and streamline curvature. Both result in a change of angle of attack due to an induced normal velocity component to the flow direction. The down-wash is important in this case since the span of the 2D model is smaller than the diameter of the wind tunnel. The airfoil is seen as a finite wing and vortices are generated. These vortices induce a down-wash velocity component that, in case of positive lift coefficient, reduce the angle of attack and create additional drag. The effect of down-wash is limited by using end plates at the airfoil tips, as shown in figure 4.3. The end plates are directly attached to the airfoil with no gap. This means that the drag of the end plates (and a part of the cylinder beyond the end plates) is incorporated in the results. No correction is applied for this, however, the change in drag coefficient between actuator on and off is still a good indication of the effect of the plasma actuator. It is assumed that with the end plates the formation of tip vortices is prevented and no down-wash is present.

Streamline curvature is of importance when the jet flow is able to diverge from its original direction downstream of the airfoil. With the absence of walls in an open jet the effect of streamline curvature is relatively large. The curvature decreases the effective angle of attack and increases the drag generated, resulting in a lift curve slope which is too small and the drag coefficient that is too high, respectively.

An analytic correction method is used for the correction of the streamline curvature based on the work of Brooks et al.[9]. The method uses the method of images where the airfoil is replaced by a distribution of vortices along the chord and the flow is approximated by a series of image vortices, see figure 4.6. This figure shows the dimensions that are important in the correction method; the nozzle width  $h$ , the chord length  $c$  and the downstream distance from the nozzle  $d$ . The method by Brooks et al. corrects the angle of attack, the drag coefficient and the moment coefficient. The effective angle of attack  $\alpha$  is found from equation 4.9.

$$\alpha = \alpha_t - \frac{\sqrt{3}\sigma}{\pi} c_{l,t} - \frac{2\sigma}{\pi} c_{l,t} - \frac{\sigma}{\pi} (4c_{mc/4,t}) \quad [\text{rad}] \quad (4.9)$$

Where  $\alpha_t$ ,  $c_{l,t}$  and  $c_{mc/4,t}$  are the measured angle of attack, section lift coefficient and the quarter chord section pitching moment coefficient respectively. The constant  $\sigma$  is given by:

$$\sigma = \frac{\pi^2}{48} \cdot \left(\frac{c}{h}\right)^2 \quad (4.10)$$

The corrected drag coefficient is calculated using the following formula:

$$c_d = c_{d,t} + \left[ -\frac{\sqrt{3}\sigma}{\pi} c_{l,t} \right] c_{l,t} \quad (4.11)$$

And finally the pitching moment coefficient correction is defined as:

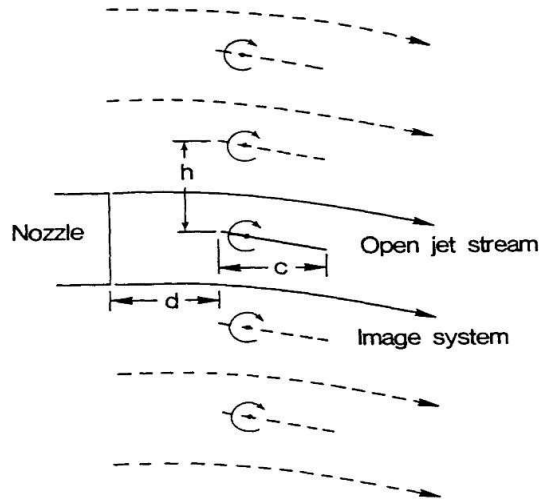


Figure 4.6: Airfoil and vortex image system used for derivation of 2D open jet streamline curvature correction

$$c_{mc/4} = c_{mc/4,t} - \frac{\sigma}{2} c_{l,t} \quad (4.12)$$

With these corrections the determination of any change in coefficients has to be considered in more detail. Equation 4.9 says that the new angle of attack is a function of the lift coefficient. The relation is such that a bigger correction occurs when the lift coefficient is larger, a schematic representation is shown in figure 4.7. In this figure the points marked by a + are the original raw data points, as measured with the force balance. The corrected points, by using equations 4.9-4.12 are marked with a x. The solid line represents the reference data and the dashed line indicates the data with plasma actuator on. Due to the correction applied the corrected data points no longer lie at approximately one single angle of attack. This means that when determining the change in any coefficient ( $\Delta c_l$ ,  $\Delta c_d$  or  $\Delta c_{mc}/4$ ) from the corrected data points one can not take the difference between the actuator on and off case (difference between x on dotted line and x on solid line, respectively). The problem is solved by interpolation of the reference data, as schematically shown in figure 4.7. The  $\Delta c_l$  of the top red x is found by interpolation of the two red x's on the solid line in order to find the  $c_l$  of the reference data at the same angle of attack as the top red x. The interpolated data point is marked by the green o. The resulting  $\Delta c_l$  of the top red x is indicated in the figure.

These are the corrections applied to the raw data. Any additional effects following from the design of the wind tunnel, such as a non-uniform flow field in the test section or other interferences and disturbances are not taken into account and are assumed to be negligible.

#### 4.4.4 Experimental test matrix: Force

During the process of this thesis work three sets of experiments are performed where the aerodynamic forces generated by the airfoil model are measured, i.e. experiments considering the plasma actuator on the rounded trailing edge, experiments with the well-known Gurney flaps that are used as reference and experiments considering leading edge plasma actuators on a flap attached to the airfoil model. This section will give an overview of the parameters that are important in these experiments.

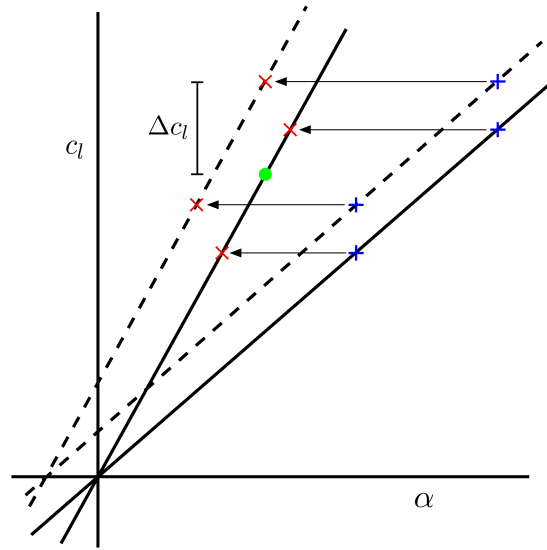


Figure 4.7: Schematic view of the method used to determine the change in coefficients

### Plasma actuator force measurements

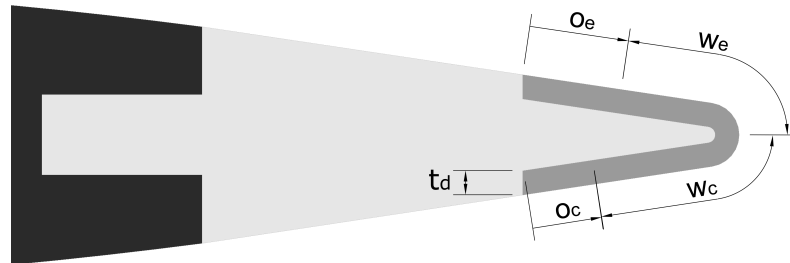
The study on the influence of the plasma actuator on the forces generated by the airfoil can be divided into two smaller parts. First a preliminary investigation is conducted to find a functional relationship between the actuator settings and the lift enhancement. The tested actuator settings are the actuation frequency,  $f_{ac}$ , and the applied peak-to-peak voltage,  $V_{app}$ . The effect of these parameters is investigated over a range of free stream velocities and angles of attack. An overview of the important parameters and variables is shown in table 4.1.

Table 4.1: Parameters used during the investigation on the effect of plasma actuator settings, for the actuator with the gap at position C

	Variation in $f_{ac}$			Variation in $V_{app}$		
	10m/s	15m/s	20m/s	10m/s	15m/s	20m/s
Free stream velocity ( $U_{\infty}$ )	10m/s	15m/s	20m/s	10m/s	15m/s	20m/s
Reynolds number (Re)	140000	210000	280000	140000	210000	280000
Measured angle of attack ( $\alpha_t$ )	0°	8°	16°	0°	8°	16°
Waveform	sine			sine		
Applied Voltage ( $V_{app}$ )	25kV			15kV	+2kV	35kV
AC frequency ( $f_{ac}$ )	500Hz	+100Hz	1500Hz	1000Hz		
Pulse frequency ( $f_p$ )	-			-		
Duty cycle (DC)	100%			100%		

The effect of the actuation frequency is tested over a range from 500Hz to 1500Hz in steps of 100Hz, while the applied voltage is kept constant at 25kV. The influence of the applied voltage is tested over a range from 15kV to 35kV in steps of 2kV, while the actuation frequency is kept constant at 1000Hz. For the preliminary study on the effect of the actuator settings on the lift enhancement the plasma actuator at position C is used. The characteristics of the plasma actuator at position C are defined by certain geometric parameters. The geometric parameters that define the location of the plasma actuator electrodes on the rounded trailing edge are given in figure 4.8.

Where  $w_e$  and  $w_c$  are the width of the exposed and covered electrode and  $o_e$  and  $o_c$  are the offset of the exposed and covered electrodes from the beginning of the PMMA dielectric, respectively.



**Figure 4.8:** Geometric parameters that define the location of the plasma actuator electrodes.

The parameter that is missing is the gap size or overlap of the electrodes. The aim is to get a zero gap size for all actuators, however, due to the small radius of the POM (inner) structure and manual application of the electrodes it difficult to get it exactly right. However, it can be said that the gap size is within  $\pm 1\text{mm}$  on the inside of the dielectric (taking into account the curvature difference between inner and outer electrode). The approximate values of the geometric parameters are summarized in table 4.2.

**Table 4.2:** Approximate values of the geometric parameters describing the electrode locations for all plasma actuators gap positions used.

Position	A	B	C	D	E
Exposed electrode offset ( $o_e$ )	2.5mm	3mm	4.6mm	7.4mm	10.3mm
Exposed electrode width ( $w_e$ )	20mm	25mm	25mm	25mm	25mm
Covered electrode offset ( $o_c$ )	12mm	10mm	9.8mm	9.1mm	8.4mm
Covered electrode width ( $w_c$ )			15mm		
Gap size (g)			0mm		
Electrode material			Copper		
Electrode thickness ( $t_e$ )			0.06mm		
Dielectric material			Plexiglass®/PMMA		
Dielectric thickness ( $t_d$ )			3mm		

The approximate locations of the electrode gaps of the plasma actuators are given in figure 4.9.

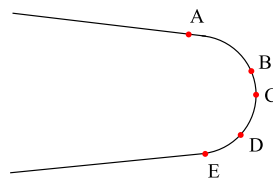


**Figure 4.9:** Plasma actuator gap position for all tested configurations.

The major goal of this thesis is to identify whether DBD plasma actuators are capable of affecting the Kutta condition of an airfoil in order to change the circulation and lift production. To avoid the typical locking of the Kutta condition, associated with sharp trailing edges airfoils, an airfoil

model with a rounded trailing edge is selected. The existence of the rounded trailing edge does however introduce an uncertainty regarding the optimum location of the plasma actuator for given flow conditions. This especially becomes important when changes in angle of attack are considered. Changing the angle of attack will move the Kutta condition compared to the actuator position, which is fixed. This will change the overall effect of the plasma actuator on the achieved change in lift. In order to reveal these effects, angle of attack sweeps are performed for 5 different actuator positions. The gap positions used in this study are defined in table 4.2. An overview of important parameters and variables in this experiment are given in table 4.3.

**Table 4.3:** Parameters used during the investigation on the effect of the plasma actuator position

Free stream velocity ( $U_\infty$ )	10m/s	15m/s	20m/s
Reynolds number (Re)	140000	210000	280000
Measured angle of attack ( $\alpha_t$ )	0°	+2°	20°
Waveform	sine		
Applied voltage ( $V_{app}$ )	35kV		
AC frequency ( $f_{ac}$ )	1kHz		

### Gurney flap force measurements

Gurney flaps have consistently proven to be a robust and simple method to achieve significant lift enhancement for airfoils. The amount of literature on this topic is extensive and the Gurney flap has found its way into several industrial applications over the years. In the field of active load control derivations of the classical Gurney flap have been proposed in order to provide dynamic lift enhancement. Although technically feasible, these concepts have not yet found their way to industrial technology readiness levels. This is mostly due to the involvement of complex moving structures required for the dynamic deployment of the Gurney flaps. It then becomes interesting to compare the results attained with the plasma actuator with a corresponding configuration involving Gurney flaps. To be able to compare the two, the tested airfoil is fitted with Gurney flaps and runs are performed at the same free stream velocities and angles of attack, as indicated in table 4.4. In order to increase the available range in Gurney flap heights,  $h$ , on the model with a rounded trailing edge, two different configurations are used. These are shown schematically in figure 4.10.

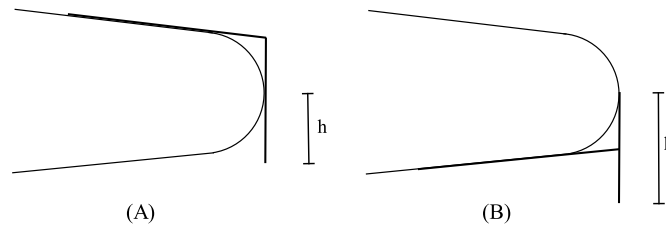


**Figure 4.10:** Schematic view of the two tested Gurney flap types.

Note that extra attention has to be paid to the implementation of the results of the two configurations. Configuration A has a blunt trailing edge while the trailing edge of configuration B is round on the upper (suction) side of the airfoil and blunt on the lower side. The corresponding Gurney flap heights are given in table 4.4.

**Table 4.4:** Parameters used during the investigation on the Gurney flaps

Free stream velocity ( $U_\infty$ )	10m/s		15m/s		20m/s	
Reynolds number (Re)	140000		210000		280000	
Measured angle of attack ( $\alpha_t$ )	0°		+2°		20°	
Flap type	A	A	A	B	B	
Flaps height (h)	2.5mm	7.5mm	10mm	11mm	13.5mm	

### Plasma flap force measurements

The use of plasma actuators for leading edge separation control is more advanced and proven to be capable of delaying stall and reattaching separated flows at angles of attack beyond normal stall. For this reason the effect of leading edge separation control by plasma actuators is investigated in more depth. During the experiment a symmetrical blade with a chord length of 5cm and span of 35cm is used as a flap and mounted onto the tested airfoil by brackets, as schematically shown in figure 4.11.

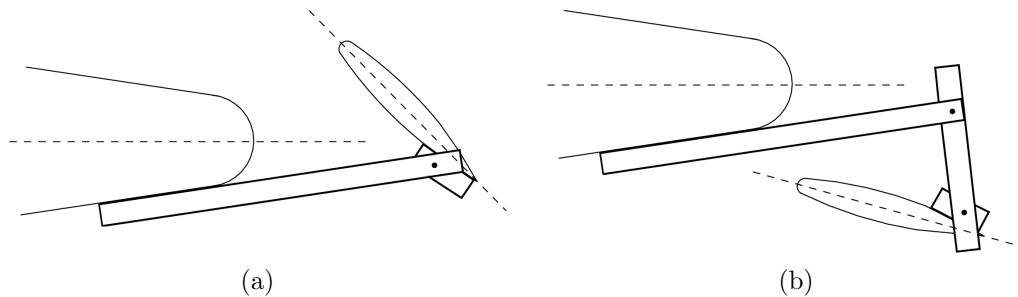


**Figure 4.11:** Schematic representation of the flap position with respect to the main airfoil: a) flap above chord line, b) flap below the chord line.

In case a the flap is above the chord on the suction side of the airfoil and in case b the flap is in a more conventional position below the chord line on the pressure side of the airfoil. The plasma actuator gap is located at the leading edge of the flap in both cases. The idea of this experiment is that the flap is continuously just beyond its stall point and that the activation of the plasma actuator will reattach the flow over the flap and therefore greatly enhance the lift generated by the airfoil. In rounded trailing edge of the main airfoil will allow for a change in the Kutta condition, which will further enhance the lift enhancement. Both configurations are tested for a variety of free stream velocities and angles of attack, as indicated in table 4.5. The focus is put on the effect of the actuation frequency, keeping in mind the effect of the Strouhal number or reduced frequency on the separation control as discussed in section 2.3.2. The dielectric used in these experiments is 2 layers of Kapton®polyimide, one layer has a thickness of 0.089mm.

## 4.5 Time-resolved PIV measurements

High speed PIV is applied to characterize the flow field in the wake of the circulation control airfoil. A two component PIV configuration is chosen since the span length of the actuator and airfoil allows the assumption of two dimensional flow for the mid-span area. This section presents the experimental set-up used, the equipment used and the experimental test matrix showing the important parameters during the test.

**Table 4.5:** Parameters used during the investigation on the effect of the flaps

	Flap above chord			Conventional flap			
	10m/s	20m/s	30m/s	10m/s	20m/s	30m/s	40m/s
Free stream velocity ( $U_\infty$ )	10m/s	20m/s	30m/s	10m/s	20m/s	30m/s	40m/s
Reynolds number (Re)	140000	280000	430000	140000	280000	430000	570000
Measured angle of attack ( $\alpha_t$ )	-6°	+2°	6°	0°	+1°	5°	
Waveform	square			square			
Applied voltage ( $V_{app}$ )	14kV			14kV			
AC frequency ( $f_{ac}$ )	0Hz	+100Hz	500Hz	0Hz	+100Hz	300Hz	
Dielectric material	Kapton®polyimide			Kapton®polyimide			
Dielectric thickness	2layers=0.18mm			2layers=0.18mm			

### 4.5.1 Experimental set-up of the PIV

The aerodynamic effect of the plasma actuator is investigated by the use of PIV, see section 3.2 for an introduction into PIV. Figure 4.12 shows schematically the test set-up as is used during these experiments. The airfoil model is mounted directly onto the wind tunnel exit by the use of two steel L-shaped frames. The end plates from the force measurements are replaced by transparent plates made out of Plexiglas® such that the camera can capture the desired part of the flow field indicated in the figure as the field of view. The laser light is deflected twice by two mirrors before it enters the laser optics that produces the thin laser sheet illuminating the plane of interest near the rounded trailing edge of the airfoil.

### 4.5.2 Tracer particles and seeding generator

The air is seeded with Safex non-toxic dyethylene-glycol/water based tracer particles of approximately  $1\mu\text{m}$  diameter generated by a Safex fog generator.

### 4.5.3 Laser and laser sheet formation

The seeding particles at the mid span of the actuator are illuminated by a light sheet of 2mm thickness generated by a dual-cavity, diode-pumped, Neodymium-doped yttrium lithium fluoride (Nd:YLF) laser (Quantronix Darwin-Duo 527-80), which emits green light with a wavelength of 527nm at a maximum pulse frequency of 10kHz. The average power output is 75W at 3kHz and the maximum pulse energy is 2.22mJ at 1kHz. The beam diameter at the laser exit is 3mm and the pulse duration or pulse width is about 190ns. The laser is operated via a high speed controller (LaVision GmbH), which is connected to the computer. For the experiments in this report both laser cavities are set to give a pulse at a frequency of 2kHz. The time separation (offset) between the two laser pulses (from separate cavities) can be set manually and depends on the free stream velocity of the flow and the maximum particle displacement of 10pixels on the sensor. For the tests in quiescent flow the  $\Delta t$  is set to  $200\mu\text{s}$ , for flows with a free stream velocity of 10 and 20m/s the  $\Delta t$  is set to  $70\mu\text{s}$  and  $35\mu\text{s}$ , respectively.

The laser sheet optics (simple mirror, +200mm spherical convergent, -100mm spherical divergent, and -200mm cylindrical divergent lenses in this order) are positioned to achieve a light sheet thickness of 2mm at the area of interest near the trailing edge of the airfoil, a picture of the optics is shown in figure 4.13.

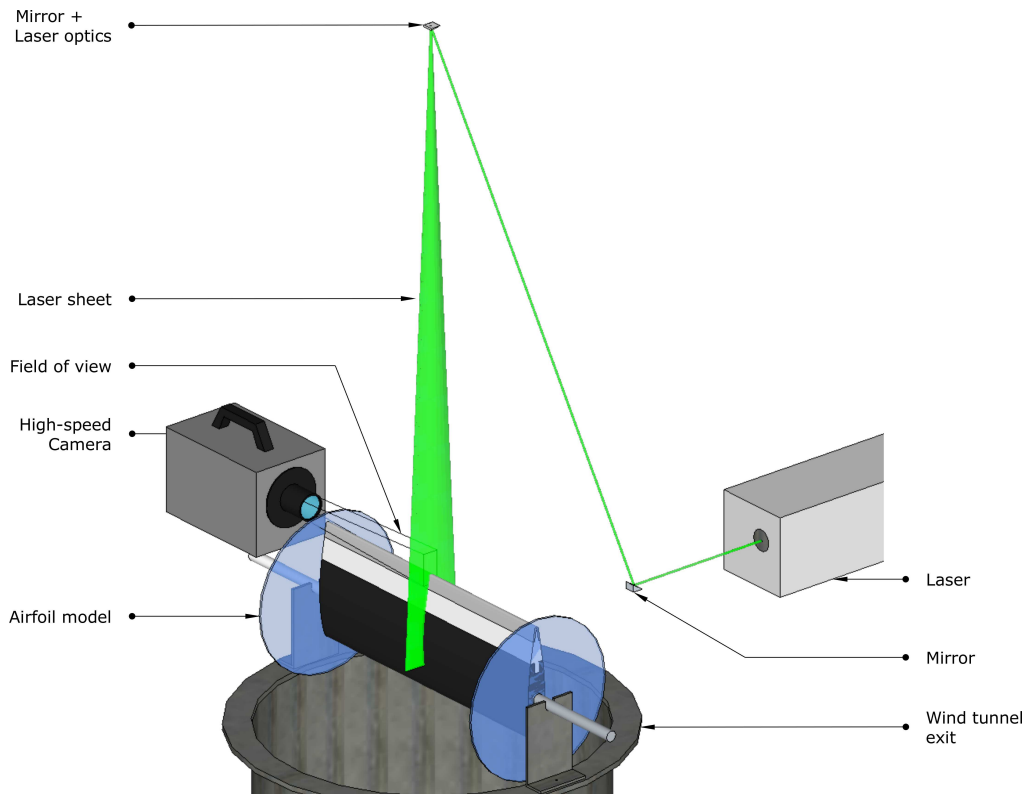


Figure 4.12: A schematic view of the PIV test set-up.

#### 4.5.4 High-speed Camera

A Photron Fastcam SA1 high-speed CMOS camera, with a 12-bit sensor size of  $1024 \times 1024 \text{pix}^2$  (full sensor size) and a pixel size of  $20 \mu\text{m}$ , is used to capture the field of view (FOV). Image acquisitions are conducted at 2kHz rate in double frame mode, therefore producing frames at 4kHz. In order to reduce the amount of data, the sensor is cropped to a size of  $1024 \times 512 \text{pix}$ . The camera is equipped with a Nikon 105mm focal length objective and is set at a  $f_{\#}$  of 4 and is used in order to achieve a magnification of 0.346. Each retrieved data set considered in this report consist of 5400 double frame images, with the rate of 2kHz this corresponds to 2.7s of time resolved PIV data.

The calibration of the PIV system consist of three parts. First the camera is focused on the desired illumination plane. In order to diminish bias-errors associated with pixel-locking[63], the particles in the viewing plane are slightly defocused to obtain a blur spot of approximately  $2 \times 2$  pixels. Secondly, a dark image (without laser light) correction is performed, to diminish camera noise. Finally, the image dimensions are determined and the origin of the axes can be set.

#### 4.5.5 Field of view

Following from the calibration, the final field of view is approximately  $60 \times 30 \text{mm}$ . The positioning of the FOV allows to calculate the flow field data in the range  $0.93 \leq x/c \leq 1.19$  and  $-0.06 \leq y/c \leq 0.06$ .

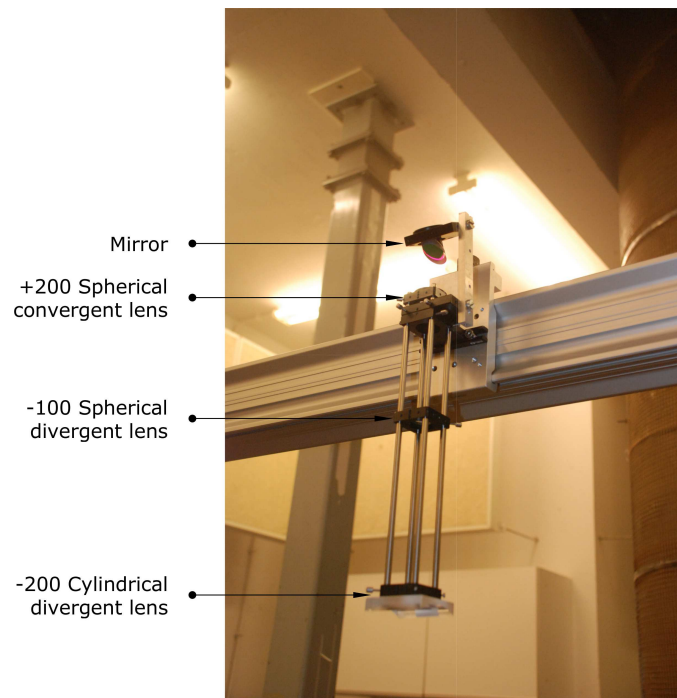


**Figure 4.13:** Photograph of the laser sheet optics used in the experiment.

#### 4.5.6 PIV-software

The laser and the high-speed camera were controlled via Davis 8.1.3 (Lavision GmbH). This software is used to operate the high speed controller for image data acquisition and to post-process the obtained double-frames by cross-correlation.

#### 4.5.7 Image processing

After the preprocessing as discussed in section 3.2.5 the double frame images are analysed using a multi-pass cross-correlation. The first cross-correlation is executed with a  $48 \times 48$ pix interrogation window (IW) using a round Gaussian weighting function, no aspect ratio and 50% overlap. For the second cross-correlation a  $12 \times 12$ pix IW with the same settings and 75% overlap is used. The final velocity vector field is returned on a grid of approximately 6 vectors per mm. The resulting velocity fields are also time averaged such that the overall flow field can be found.

#### 4.5.8 Experimental test matrix: PIV

PIV is applied in order to characterize the flow field around the rounded trailing edge. The recording parameters which are kept constant during the PIV experiments are presented in table 4.6.

Two selected actuator positions, angles of attack and free stream velocities are tested. Besides this also the quiescent condition is investigated in order to get an indication of the induced velocity and momentum generated by the plasma actuator. The data in tables 4.6 and 4.7 can be found in section 4.5 or calculated from the data presented in this section.

**Table 4.6:** Constant recording parameters of the PIV set-up

Recording medium	Photron Fastcam SA1.1
Recording lens	$f = 105\text{mm}$
Illumination	Nd:YLF laser
Focal length of lens 1, $f_1$	+200
Focal length of lens 2, $f_2$	-100
Focal length of lens 3, $f_3$	-200
Lasersheet thickness	2mm
Seeding material	Non-toxic glycol/water based fog ( $d_p \approx 1\mu\text{m}$ )

**Table 4.7:** Parameters of the PIV set-up

Free stream velocity ( $U_\infty$ )	0m/s	10m/s	20m/s
Reynolds number (Re)	140000	210000	280000
Measured angle of attack ( $\alpha_t$ )	0°		12°
Aperture $f_\#$		$f/4$	
Repetition rate		2kHz	
Recording method		double-frame	
Recording time		2.8s	
Pulse delay	200 $\mu\text{s}$	70 $\mu\text{s}$	35 $\mu\text{s}$
FOV ( $x \times y$ )		1024 $\times$ 512pix <sup>2</sup> 59.2 $\times$ 29.5mm <sup>2</sup>	
Digital resolution		17.3pix/mm	
Magnification (M)		0.35	
Interrogation window (IW) ( $x \times y$ )		12 $\times$ 12pix <sup>2</sup> 0.69 $\times$ 0.69mm <sup>2</sup>	
IW overlap		75%	
Vectors per field		342 $\times$ 171	
Vectors per mm		6	

## 4.6 Power consumption measurements

This section will discuss the experiment performed in order to find the power consumption of a plasma actuator in relation to the electrical parameters  $f_{ac}$  and  $V_{app}$ . Both the equipment that is used and the experimental test matrix are presented here.

### 4.6.1 Oscilloscope and capacitor

The integrating capacitor method requires the measured voltage across the capacitor and the applied voltage over the electrodes. The voltages are acquired by the use of a Tektronix TDs3054c

digital oscilloscope. The voltages are measured at a frequency of 1Ghz. The capacitor is placed in series between the covered electrode and the ground and the capacitance of the used capacitor is 150nF.

#### 4.6.2 Experimental test matrix: Power consumption

The integrating capacitor method is used to calculate the power consumption of the plasma actuator. The parameters that are of importance during the experiment are shown in table 4.8. The power consumption is calculated for a sweep in actuation frequency and a sweep in applied peak-to-peak voltage. The plasma actuator at position C is used in this experiment, details on the plasma actuator can be found in table 4.2.

**Table 4.8:** Parameters used during the investigation on the power consumption, for the actuator with the gap at position C

	Variation in $f_{ac}$			Variation in $V_{app}$		
Free stream velocity ( $U_{\infty}$ )	0m/s			0m/s		
Measured angle of attack ( $\alpha_t$ )	0°			0°		
Waveform	sine			sine		
Applied Voltage ( $V_{app}$ )	25kV			15kV	+2kV	35kV
AC frequency ( $f_{ac}$ )	500Hz	+100Hz	1500Hz	1000Hz		
Pulse frequency ( $f_p$ )	-			-		
Duty cycle (DC)	100%			100%		

---

# Chapter 5

---

## Results

This chapter presents the results obtained through the various experiments, as described in chapter 4. The experiments were performed in two major campaigns, the first campaign corresponds to the first section and includes all data obtained from measurements of the aerodynamic forces generated by the airfoil. The second section will discuss the achieved lift augmentation in more detail, including thrust calculations from the PIV velocity field measurements. The third section will discuss the second test campaign, during which the PIV technique is used to visualize the flow field around the rounded trailing edge and to calculate some typical wake characteristics. The final section deals with the power consumption measurements.

### 5.1 Force measurements

The first experimental campaign included all measurements performed with the force balance, as discussed in section 4.4. Due to the different cases that were considered, this section is divided in four subsections. The first subsection gives the results obtained with the rounded trailing edge model. The second subsection presents the data for the Gurney flap configurations, acting as a reference case. This subsection is followed by two subsections describing the experiments performed on the two flap configurations with leading edge plasma actuation. The third section for the flap above the chord line and the final section for the conventional flap layout, respectively. See section 4.4 for more information on the experimental set-up and tested parameters in each experiment.

#### 5.1.1 Rounded trailing edge model

The results from all experiments on the rounded trailing edge model are subdivided in three parts: a parametric study ( $f_{ac}$  and  $V_{app}$  sweeps), an angle of attack study ( $\alpha$  sweep) and a Reynolds number study ( $Re$  sweep).

##### Parametric study

Prior to the investigation regarding the effect of the actuator position, a parametric study was conducted to find a functional relationship between the actuator settings and the lift enhancement.

The tested plasma actuator settings are the actuation frequency,  $f_{ac}$ , and the applied peak-to-peak voltage,  $V_{app}$ . The results of this study will set the voltage and frequency values for the following experiments with the plasma actuator on the rounded trailing edge model. All data obtained for this study corresponds to plasma actuator position C, see figure 4.9.

The effect of the carrier frequency on the lift coefficient  $c_l$  at different free stream velocities and angles of attack can be seen in figure 5.1. These graphs are generated at a constant applied voltage of 25kV. The range of  $c_l$  for every graph is kept constant. This way the angle of attack effect can be compared. The offset between curves is caused by a slight difference in angle of attack in subsequent runs, which is set manually for every point. Each point is the mean of 10 data points, as discussed in section 3.1. The error bar corresponds to the standard deviation  $\pm\sigma$  of the 10 data points.

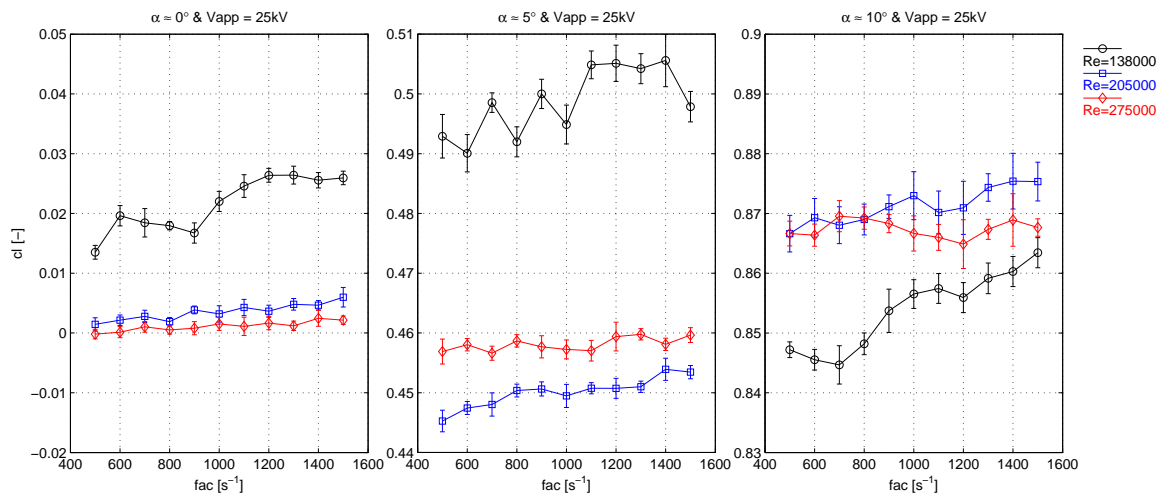
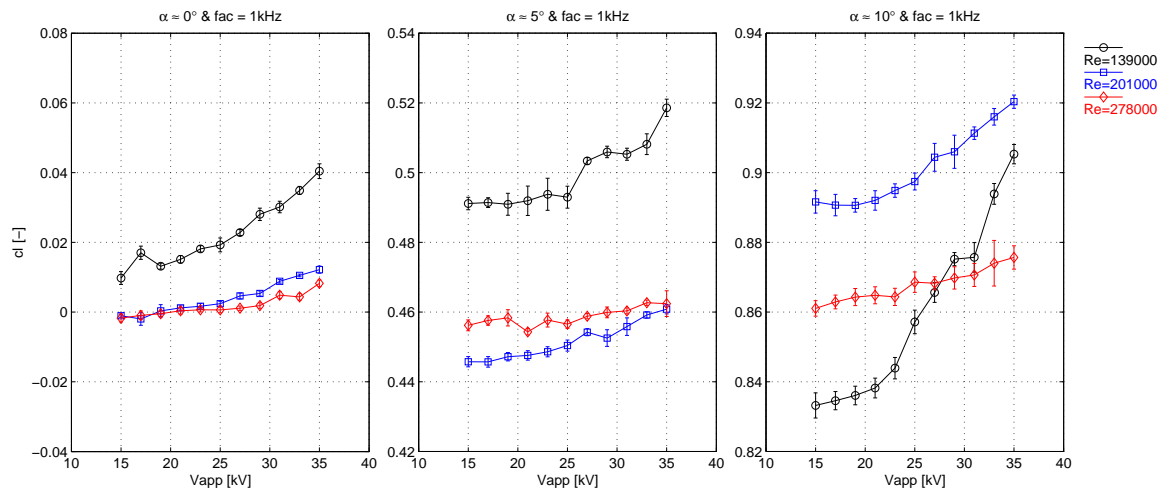


**Figure 5.1:** Variation of lift coefficient against carrier frequency for varying Reynolds number and angle of attack, plasma actuator position C.

It is clear that increasing the carrier frequency has no significant effect on  $c_l$ . Over the range of 1kHz the increase stays within a  $\Delta c_l$  of 0.01. Additionally, the effectiveness decreases significantly with increasing Reynolds number. At  $Re = 2.75 \cdot 10^5$  the effect is nearly negligible, especially when considering the data scatter. The angle of attack effect can be found when comparing the  $\alpha = 0^\circ$  and  $10^\circ$  graphs. Although the data shows more scatter at  $10^\circ$ , the change in  $c_l$  with  $f_{ac}$  is comparable to the  $0^\circ$  case for all Reynolds numbers.

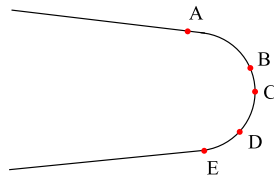
The overall effect of the carrier frequency on the lift coefficient is found to be insignificant, especially at higher velocities. Therefore it is concluded that the carrier frequency does not play an important role and it is decided to use a value of 1kHz for further experiments on the rounded trailing edge model.

Figure 5.2 shows the effect of the applied voltage on the lift coefficient for different velocities and angles of attack at a constant carrier frequency of 1kHz. Keep in mind that the applied voltage is peak-to-peak, meaning that the maximum voltage amplitude of the signal is half of the applied peak-to-peak voltage. The data range on the y-axis is again kept constant to see the angle of attack effect. The offset between curves is caused by a slight difference in angle of attack in subsequent runs.



**Figure 5.2:** Variation of lift coefficient against applied peak-to-peak voltage for varying Reynolds number and angle of attack, plasma actuator position C.

It can be seen that an increase in applied voltage has a stronger effect on the lift coefficient than the carrier frequency. The influence of the Reynolds number stays the same, the efficiency decreases at higher Reynolds numbers. Finally, an increase in angle of attack has a strong effect on the effectiveness of the plasma actuator. This can be seen from the graph at an angle of attack of  $10^\circ$ , where the increase in  $c_l$  is higher between 15 and 35kV than in case of  $0^\circ$  or  $5^\circ$ .



**Figure 5.3:** Plasma actuator gap position for all tested configurations. Copied from chapter 4.

From figure 5.2 it can be concluded that a higher applied voltage will increase the change in lift coefficient between the actuator on and off cases. Due to limitations of the dielectric and considering the degradation of the material it is decided that a value of 35kV is used for further experiments on the rounded trailing edge model.

### Angle of attack study

After the parametric study on the actuation settings an investigation on the effect of the plasma actuator positioning was performed. Angle of attack sweeps were generated for 5 different actuator gap positions as indicated in figure 5.3 as a reminder. The corresponding  $c_l - \alpha$  curves are shown in figure 5.4 for different Reynolds numbers. The reference data is from a run with the actuator (electrodes) on the model but without actuation. The reference data is corrected for the symmetric profile such that  $c_l = 0$  at  $\alpha=0$ .

The graphs show both the decreasing efficiency with increasing Reynolds number and the angle of attack effect mentioned before. The plasma actuator is most efficient at angles of attack right

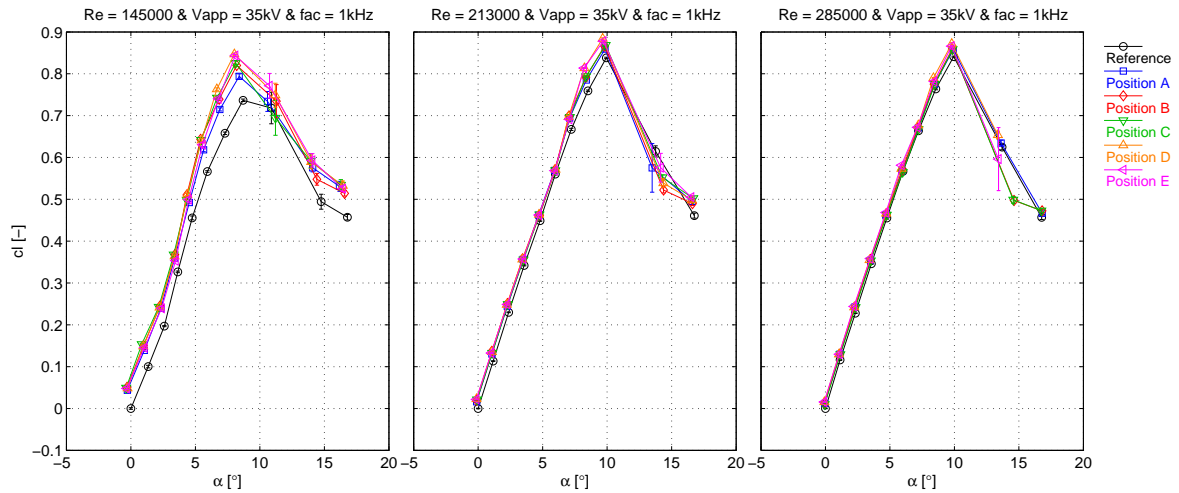


**Figure 5.4:** Variation of lift coefficient against angle of attack for varying Reynolds number and all plasma actuator gap positions.

before the airfoil stalls, at angles of attack between approximately  $7^\circ$  and  $10^\circ$ .

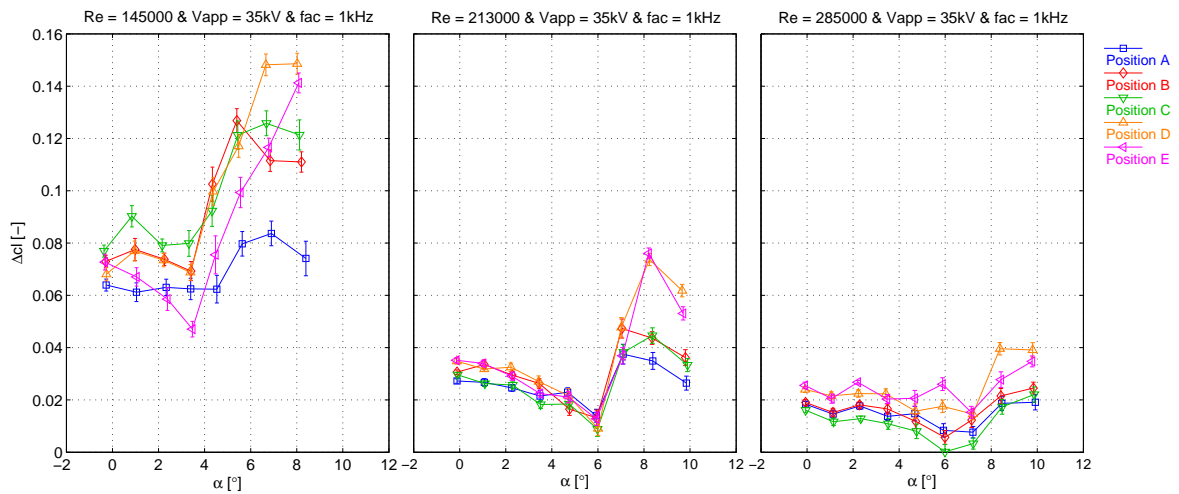


**Figure 5.5:** The change in lift coefficient against angle of attack for varying Reynolds number and all plasma actuator gap positions.

The increase in lift coefficient between cases with and without plasma actuation is plotted in figure 5.5. Again the scale on the y-axis is kept the same as the Reynolds number is changed. When comparing the different actuators configurations it is found that position D is the most efficient at all Reynolds numbers, followed by position C at that lowest Reynolds number and position E at higher Reynolds numbers. The decrease in effectiveness with the increase in Reynolds number is again clearly visible and so is the effect with angle of attack. At angles of attack close to stall the increase in lift coefficient is consistently higher. This holds for all plasma actuator configurations. No explanation could be found for the decrease in  $\Delta c_l$  at  $\alpha=6^\circ$  for  $Re=2.13 \cdot 10^5$ .

The variation of the drag coefficient with angle of attack is shown in figure 5.6. As a reminder,

the drag coefficient presented here includes the drag generated by the model plus the drag of the end plates and a small part of a bar that is necessary to mount the model in the balance. However, an indication of the change in drag due to plasma actuation is found by subtracting the drag from the reference run. The results from this can be found in figure 5.7. In general the drag coefficient shows the same behaviour as for the lift coefficient; the higher the Reynolds number, the smaller the drag coefficient increase and for larger angles of attack the drag coefficient increases.

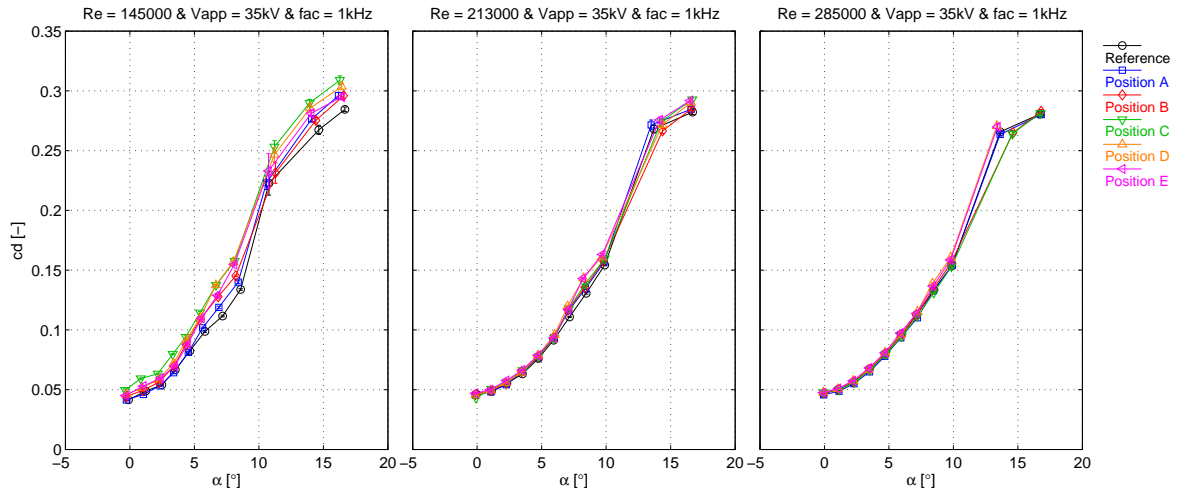


Figure 5.6: Variation of drag coefficient against angle of attack for varying Reynolds number and all plasma actuator gap positions.

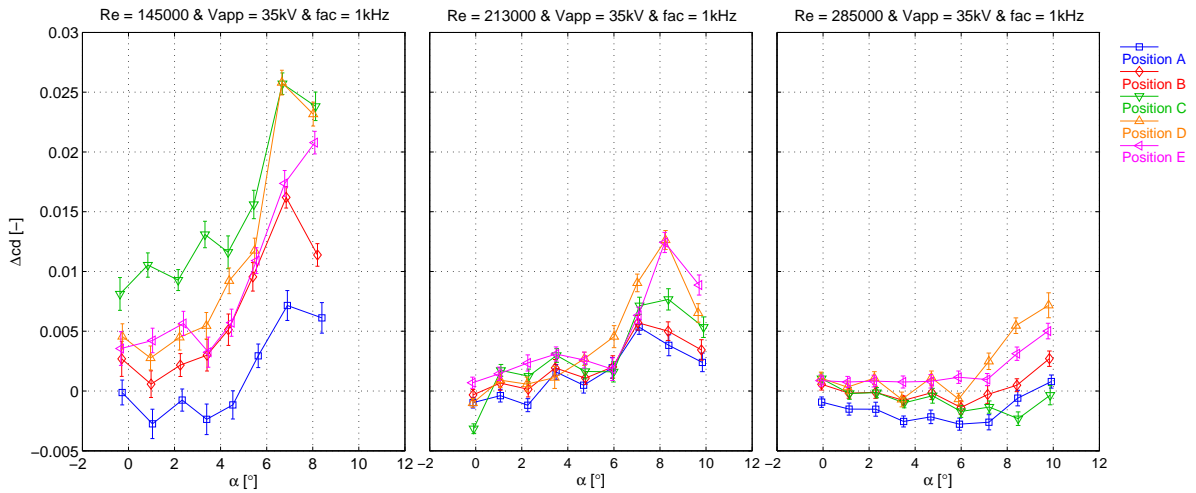


Figure 5.7: Change in drag coefficient against angle of attack for varying Reynolds number and all plasma actuator gap positions.

Since both the lift and drag coefficient increase with a small amount the  $c_d - c_l$  curves are similar to the reference case. This is presented in figure 5.8. In percentages the increase in drag coefficient is larger than the increase in lift coefficient, that is causing the graphs to be on the right side of the reference case. Only in case of plasma actuator A the  $c_l/c_d$  efficiency is increased. However, the increase in lift coefficient for the corresponding actuator position is the smallest of all tested

cases, especially at high angles of attack (see figure 5.5).

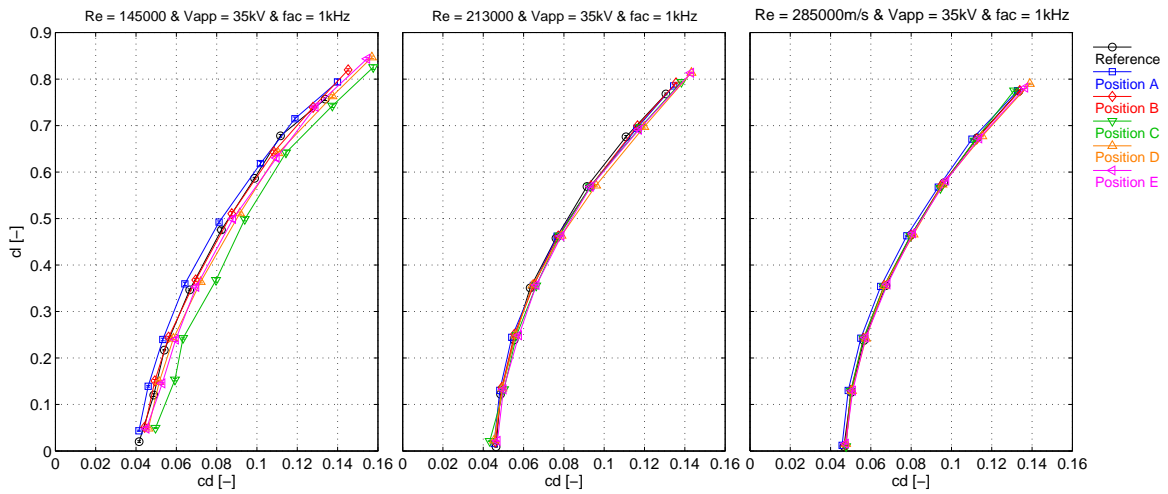


Figure 5.8: Lift against drag coefficient for varying Reynolds number and all plasma actuator gap positions.

### Reynolds number study

Finally, the effect of the Reynolds number is investigated in more depth. Figures 5.9 and 5.10 show the change in lift coefficient with Reynolds number for small and large angles of attack, respectively. The reference run used is the same as in previous figures. It is clear that the effectiveness of the plasma actuator decreases with the Reynolds number, as expected. The plasma actuator adds a constant momentum to the flow for all Reynolds numbers. For higher Reynolds numbers the relative momentum input decreases with respect to the momentum of the flow, resulting in a smaller efficiency.

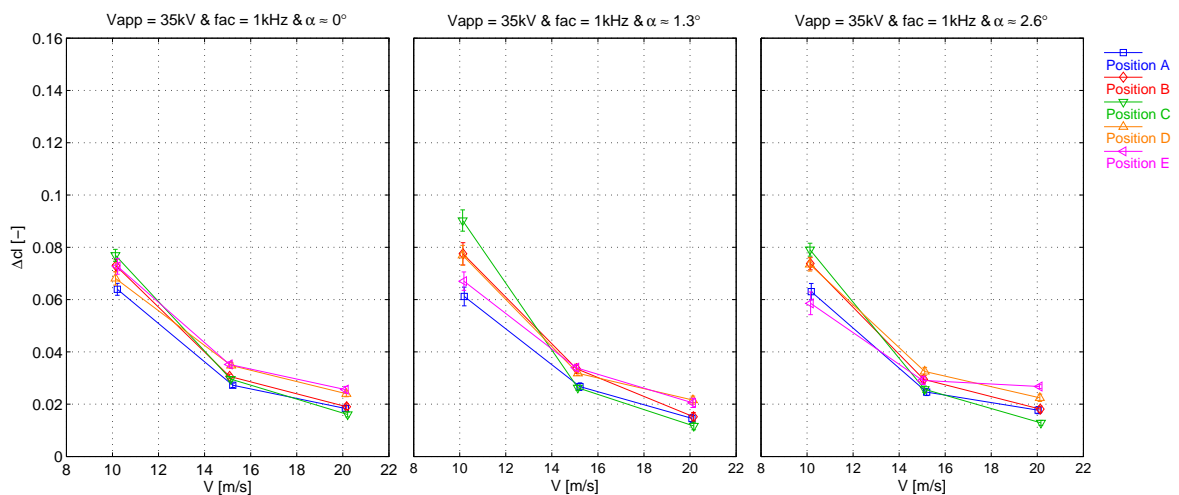
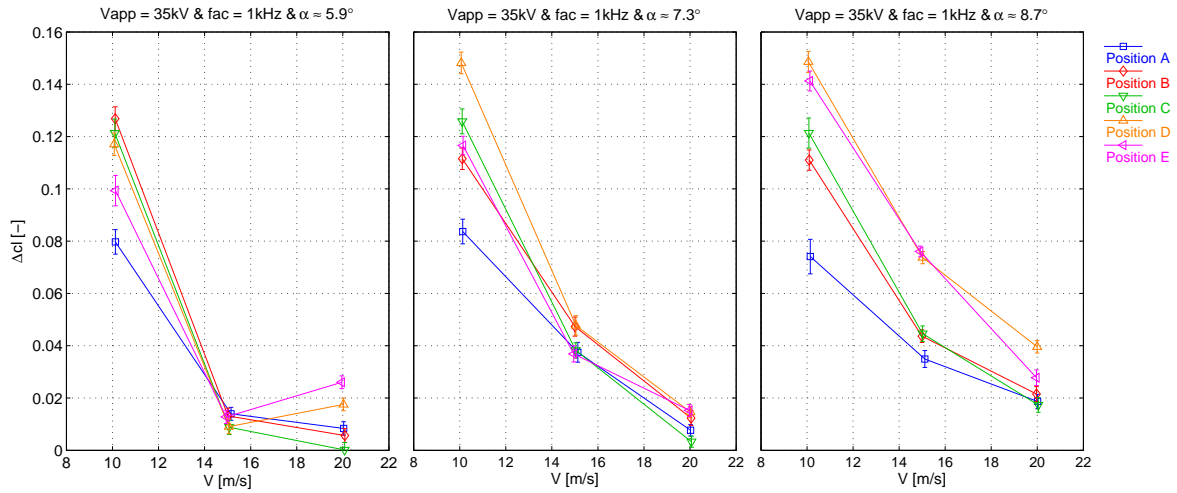


Figure 5.9: Change in lift coefficient against Reynolds number for three small angles of attack and all plasma actuator gap positions.



**Figure 5.10:** Change in lift coefficient against Reynolds number for three angles of attack near stall and all plasma actuator gap positions.

### 5.1.2 Gurney flap

Angle of attack sweeps with the Gurney flap configurations were performed for identical conditions as with the plasma actuators. As a reminder the Gurney flap configurations are repeated in figure 5.11, with the corresponding geometric and flow parameters in table 4.4. The results from all experiments with the Gurney flaps are subdivided in two parts: an angle of attack study ( $\alpha$  sweep) and a Reynolds number study ( $U_\infty$  sweep).

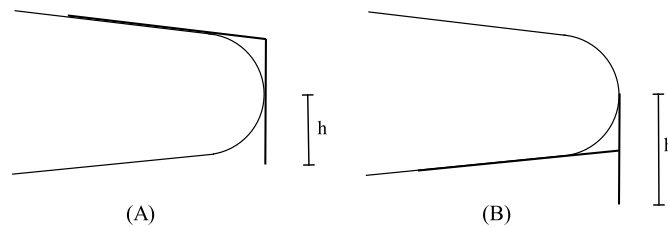


**Figure 5.11:** Schematic view of the two tested Gurney flap types. Copied from chapter 4.

#### Angle of attack study

The variation of the lift coefficient with angle of attack for all tested Gurney flaps are presented in figure 5.12. Additionally the most effective DBD plasma actuator configuration (position D) is shown for comparison.

It is clear that the Gurney flap is able to generate significant changes in the lift compared to the plasma actuator and the reference case, which is the same as before, i.e. the airfoil with the plasma actuator electrodes but without actuation. The lift generated by plasma actuator at position D is of the same order as the type 2A Gurney flap configuration at high angles of attack and at the lowest Reynolds number, i.e.  $Re=1.42 \cdot 10^5$ . This can also be seen in figure 5.13, where the change in lift coefficient is plotted against the angle of attack.

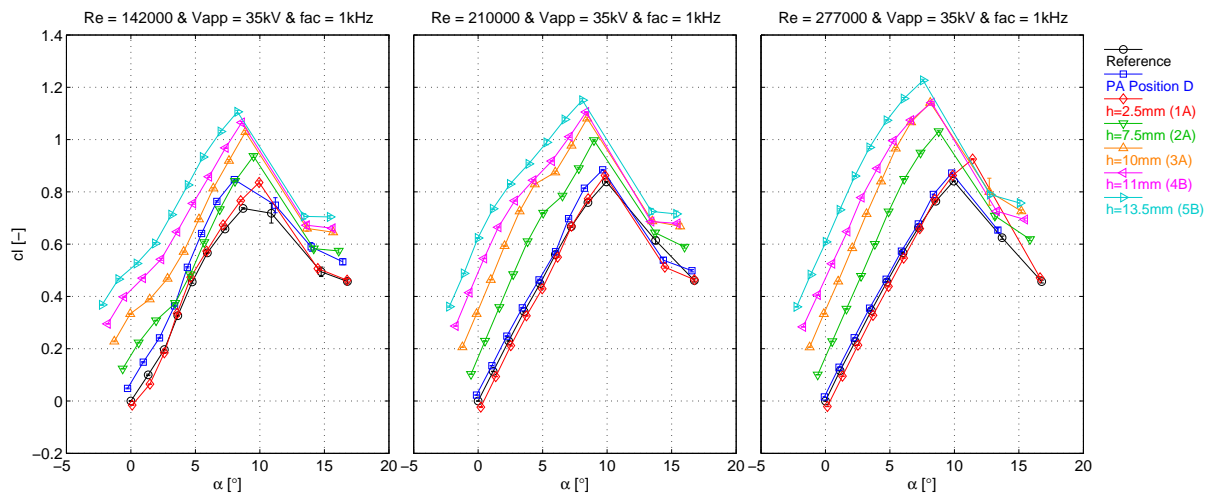


**Figure 5.12:** Variation of lift coefficient against angle of attack for varying Reynolds number and all Gurney flap configurations + plasma actuator position D

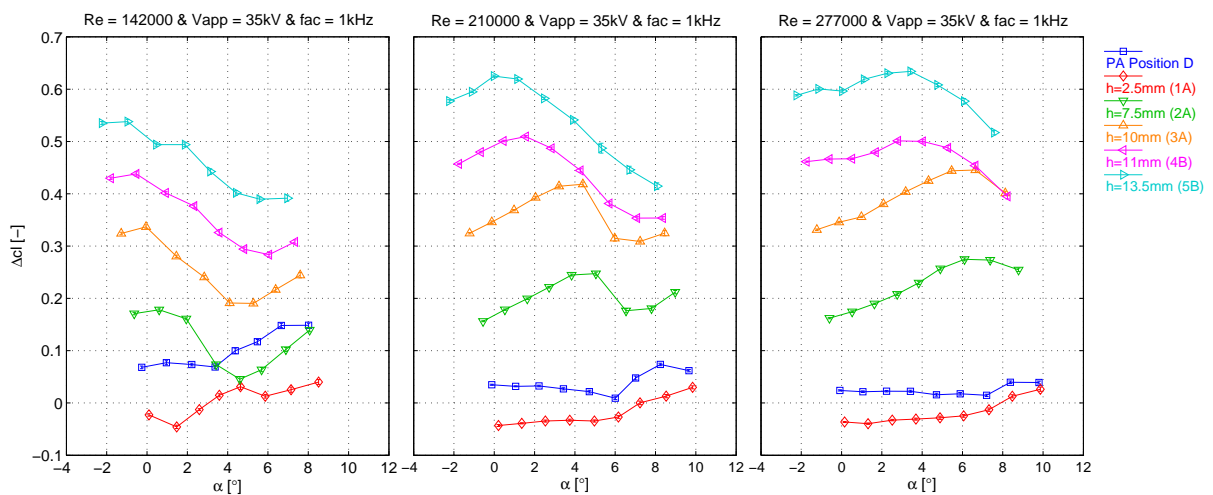


**Figure 5.13:** Change in lift coefficient against angle of attack for varying Reynolds number and all Gurney flap configurations + plasma actuator position D

The type 2A Gurney flap corresponds to the blunt trailing edge flap with a height of 7.5mm from the chord line. The part of the Gurney flap that is effectively penetrating the boundary layer, coming from the pressure side of the airfoil, is approximately 4mm or  $h/c=0.018$ , this value is obtained by considering the rounded trailing edge radius and the slope of the airfoil just before the trailing edge. The same way it can be said that the smallest Gurney flap has a negative effective height and together with the blunt trailing edge it shows a slight detrimental effect on the lift production. Besides this it seems that the effectiveness of the Gurney flaps is not limited by the Reynolds number, since strong lift enhancement is visible up to the highest Reynolds number tested, i.e.  $Re=2.77 \cdot 10^5$ . At this Reynolds number the effect of the plasma actuator is considerably weaker.

For the largest Gurney flap, with a effective height of 10mm or  $h/c=0.046$ , a maximum change

in  $c_l$  of 0.6 is reached. It is difficult to find the effect of the Gurney flap type, i.e. the full blunt trailing edge type A and the half blunt trailing edge type B, since the different types are not tested at the same Gurney flap height. The only remark made here is on the  $Re=2.77 \cdot 10^5$  case. In the corresponding graph in figure 5.13 it is noticed that the lift enhancement at small angles of attack is more constant in the case of the half blunt trailing edge Gurney flap were in the case of full blunt trailing edge the lift enhancement shows a constant increase. However, the effect is minimal and not visible at lower Reynolds number.

The variation of the drag coefficient with the angle of attack is shown in figure 5.14. Again, remember that the drag coefficient presented here includes the drag generated by the model plus the drag of the end plates and a small part of a bar that is necessary to mount the model in the balance.

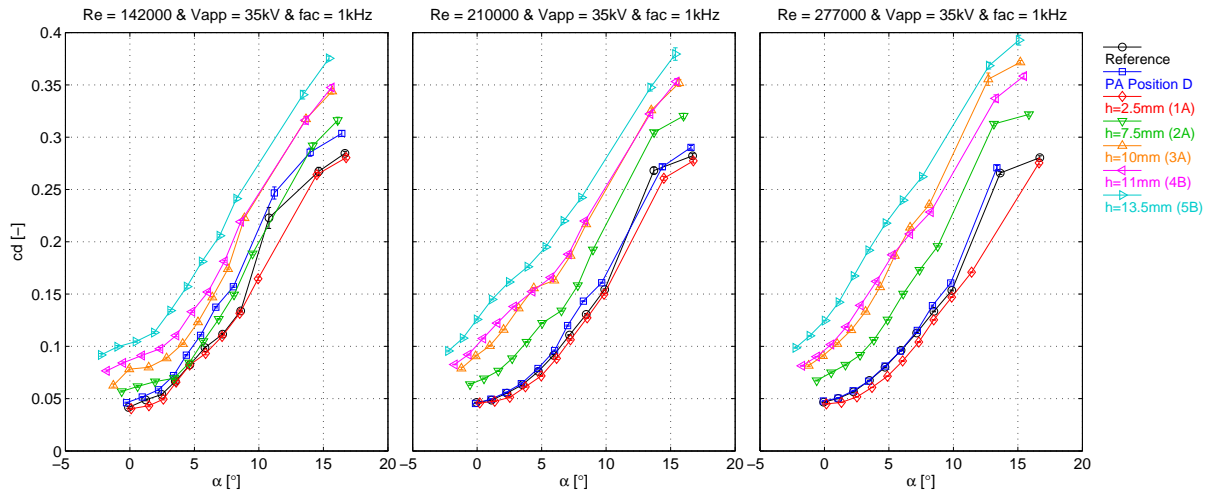
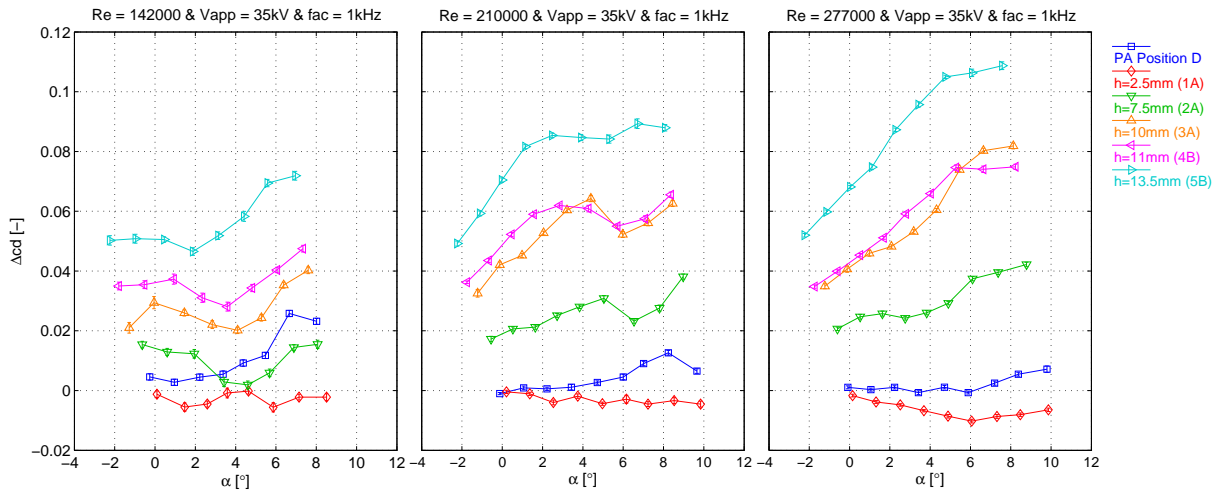


Figure 5.14: Variation of drag coefficient against angle of attack for varying Reynolds number and all Gurney flap configurations + plasma actuator position D

As is known from the Gurney flaps, the large lift enhancement comes at the cost of an increase in drag. For the largest Gurney flap height tested, with an effective flap height of  $h/c=0.046$ , the drag is more than doubled with respect to the reference airfoil. From the change in drag coefficient against angle of attack in figure 5.15 it follows again that the drag coefficient increment of the type 2A Gurney flap in of the same order as the plasma actuator at position D for the lowest Reynolds number case. For higher Reynolds numbers the drag of the Gurney flaps is increased due to the thinner boundary layers and the corresponding larger effective Gurney flap height.

When considering the type 1A Gurney flap, with the negative effective flap height, it can be seen that the drag coefficient is actually decreased. This could be caused by a reduction in the vortex sheet strength due to the asymmetric trailing edge shape. The difference between the full blunt and half blunt Gurney flap configurations is better visible in the drag coefficient. When comparing the 3A and 4B types it seems that the half blunt Gurney flap of type 4B has a lower drag increase for the same flap height, especially at higher Reynolds number. This is confirmed by the  $c_l - c_d$  curves in figure 5.16, where it is shown that the relative drag increase of type 4B is lower than for type 3A.



**Figure 5.15:** Change in drag coefficient against angle of attack for varying Reynolds number and all Gurney flap configurations + plasma actuator position D

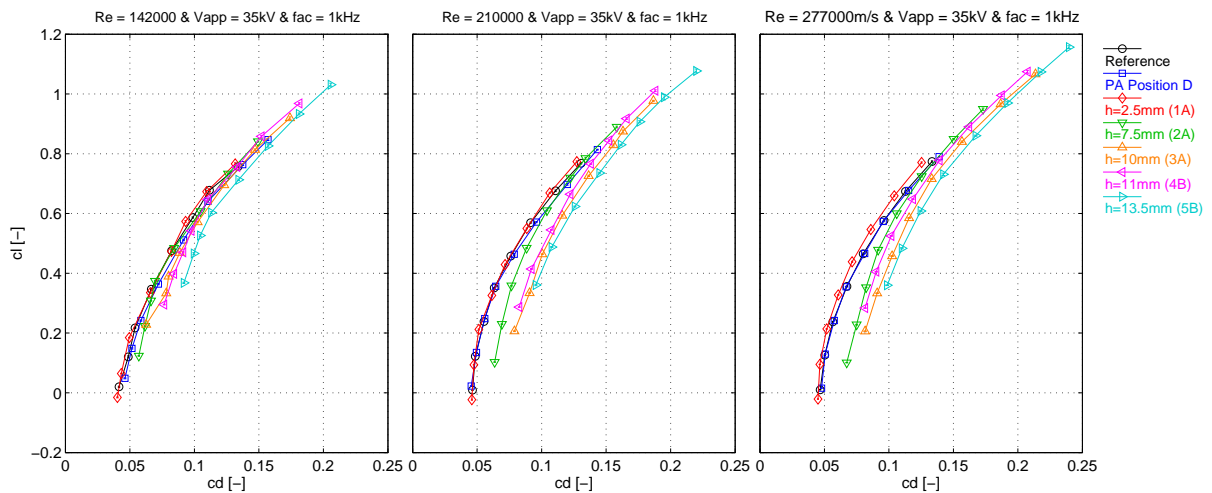


**Figure 5.16:** Lift against drag coefficient for varying Reynolds numbers and all Gurney flap configurations + plasma actuator position D

## Reynolds number study

In this section the effect of the Reynolds number is investigated in more depth. Figures 5.17 and 5.18 show the change in lift coefficient with Reynolds number for small and large angles of attack, respectively. The reference run used is the same as in previous figures. In contrast to the plasma actuators the effectiveness of the Gurney flap is increasing with Reynolds number, the higher Reynolds numbers reduces the boundary layer thickness and makes any geometric shape more effective. Due to the negative effective flap height of the type 1A flap it does not show the same behaviour.

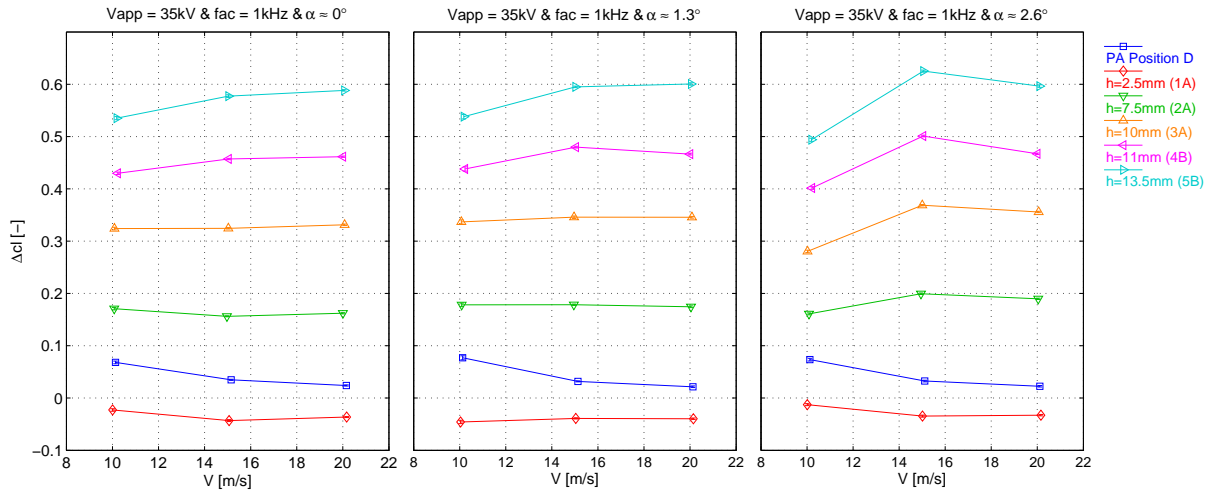


**Figure 5.17:** Change in lift coefficient against Reynolds number for three small angles of attack and Gurney flap configurations + plasma actuator position D.

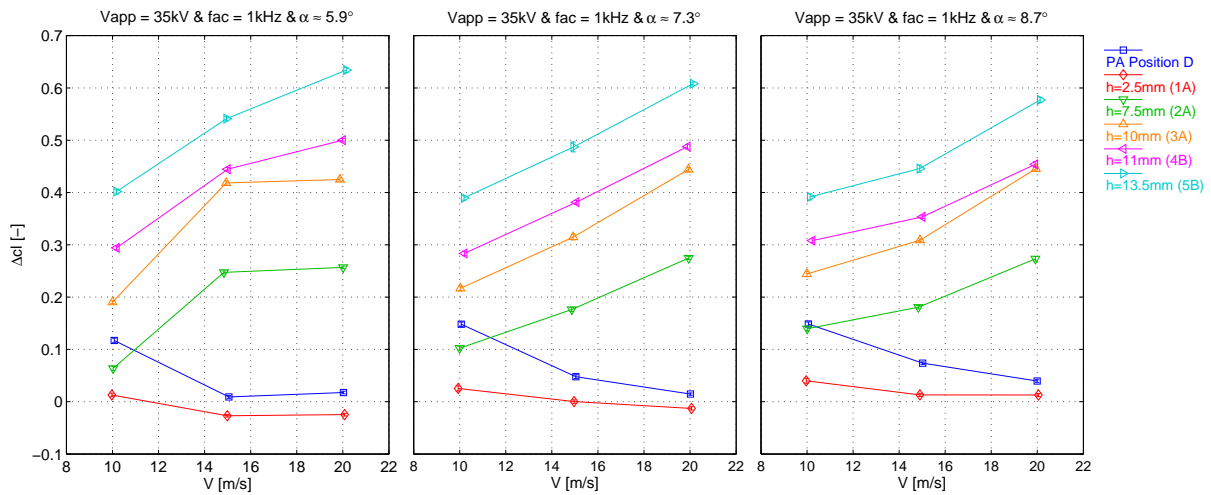


**Figure 5.18:** Change in lift coefficient against Reynolds number for three angles of attack near stall and all Gurney flap configurations + plasma actuator position D.

### 5.1.3 Trailing edge flap above chord line

During the experiment with the trailing edge flap above the chord line the focus was put on the effect of the actuation frequency ( $f_{ac}$  sweep) of the leading edge plasma actuator. The configuration used in this case is again shown in figure 5.19a. The effect of the Reynolds number is discussed briefly.

#### Parametric study

In the current case, where the flap is situated above the chord line, the stall angle of the flap is found manually for each angle of attack. This is done by the use of tufts attached to the flap. The achieved change in lift coefficient for every tested actuation frequency is shown in figure 5.20.

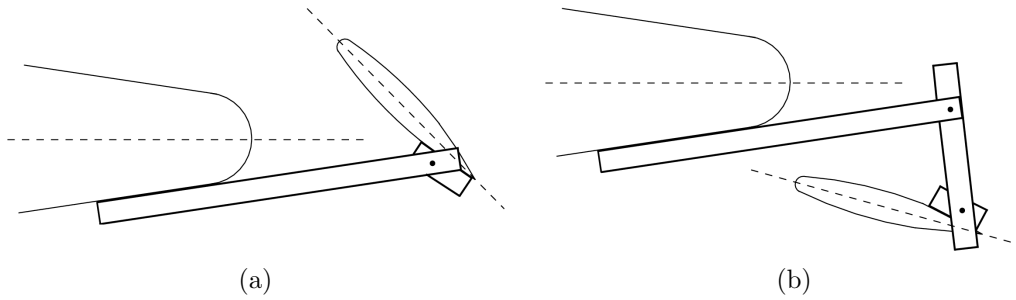


**Figure 5.19:** Schematic representation of the flap position with respect to the main airfoil: a) flap above chord line, b) flap below the chord line. Copied from chapter 4.

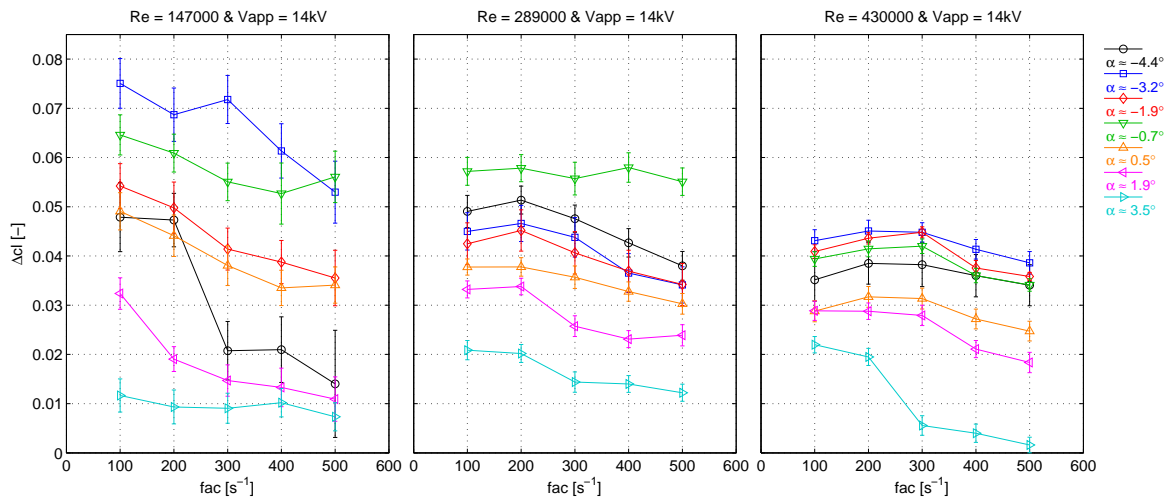


**Figure 5.20:** Change in lift coefficient against carrier frequency for different angles of attack and Reynolds numbers (flap above chord line)

The  $\Delta c_l$  is in this case the difference between plasma on and off for each individual angle of attack. The spread in the data between different angles of attack is probably caused by the manual adjustments made during the experiment. Although manual adjustments were made it turned out that the flap deflection, with respect to the chord line of the main airfoil, stayed approximately  $34^\circ$  for all angles of attack. For Reynolds numbers  $2.89 \cdot 10^5$  and  $4.3 \cdot 10^5$  a small effect of the actuation frequency is found, at  $Re=2.89 \cdot 10^5$  the peak in lift enhancement lies at approximately 200Hz, while for  $Re=4.3 \cdot 10^5$  the peak is shifted to approximately 225Hz. The corresponding Strouhal numbers (equation 2.6) corresponding to these values are  $St_D=0.5$  and  $0.375$ , respectively. The fact that these values are not close to each other, as is expected, is probably caused by the effect of the main body on flow over the flap.

Figure 5.21 shows the change in drag coefficient between actuator on and off. Increasing the actuation frequency, with respect to low frequency actuation, decreases the drag in all cases. Due to the manual adjustments made at each angle of attack no further conclusions can be drawn from this data.

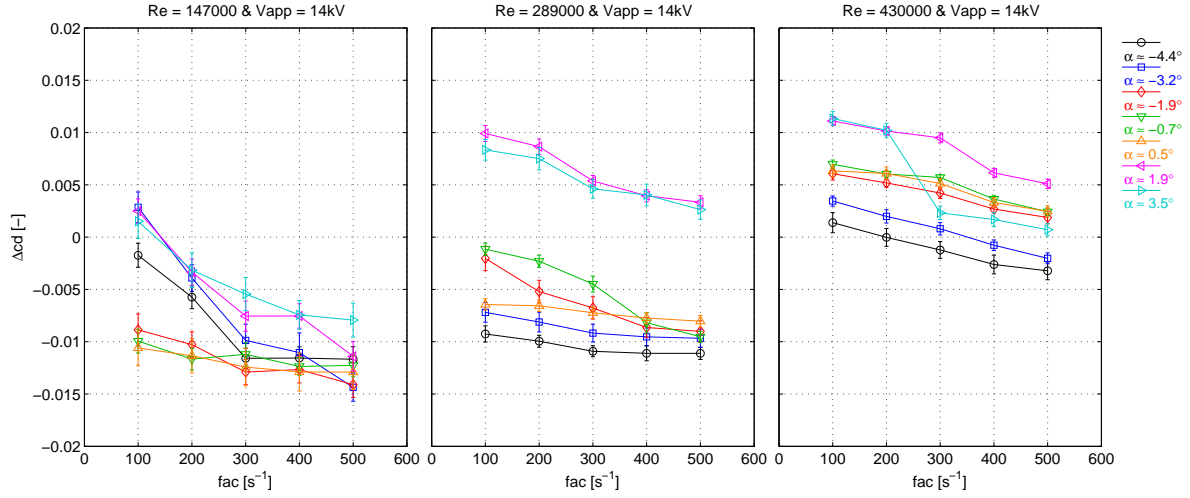


**Figure 5.21:** Change in drag coefficient against carrier frequency for different angles of attack and Reynolds numbers (flap above chord line)

### Reynolds number effect

From the data presented in figure 5.20 it is concluded that the effect of the Reynolds number is less pronounced compared to the case with rounded trailing edge actuation. Even for Reynolds numbers up to  $4.3 \cdot 10^5$  the lift enhancement is still clearly visible.

#### 5.1.4 Trailing edge flap below chord line

After this an the same experiment was performed with the conventional trailing edge flap. The configuration used in this case is again shown in figure 5.19b. Again the effect of the actuation frequency ( $f_{ac}$  sweep) of the leading edge plasma actuator is investigated. The effect of the Reynolds number is discussed briefly.

#### Parametric study

For the conventional trailing edge flap layout the choice was made to keep the flap deflection fixed at approximately  $14^\circ$  for all angles of attack. The achieved change in lift coefficient for every tested actuation frequency is shown in figure 5.22.

The  $\Delta c_l$  is again the difference between plasma on and off. This time the same effect of the actuation frequency is found, albeit at higher Reynolds number. At  $Re=4.28 \cdot 10^5$  the peak in lift enhancement lies at approximately 190Hz, while for  $Re=5.71 \cdot 10^5$  the peak is shifted to approximately 225Hz. The corresponding Strouhal numbers (equation 2.6) corresponding to these values are  $St_D=0.317$  and  $0.281$ , respectively. The effect is however not as strong as expected from previous experiments on leading edge plasma actuation, probably due to the effect of the main body on the flow over the flap.

Figure 5.21 shows the change in drag coefficient between actuator on and off. Increasing the actuation frequency, with respect to low frequency actuation, decreases the drag in all cases. The overall effect of plasma actuation is the slight increase in drag coefficient at all angles of attack and Reynolds numbers.

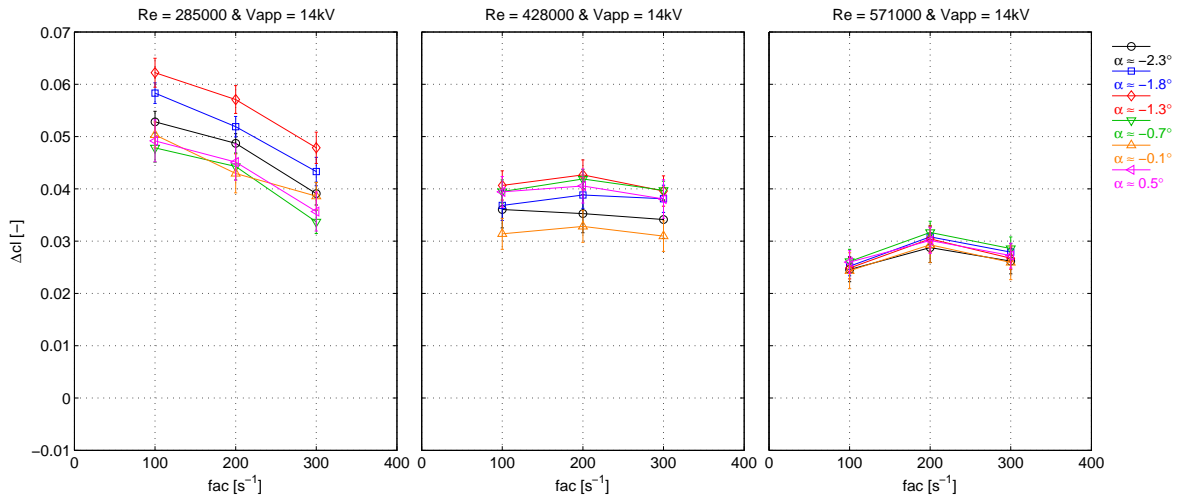


**Figure 5.22:** Change in lift coefficient against carrier frequency for different angles of attack and Reynolds numbers (flap below chord line)

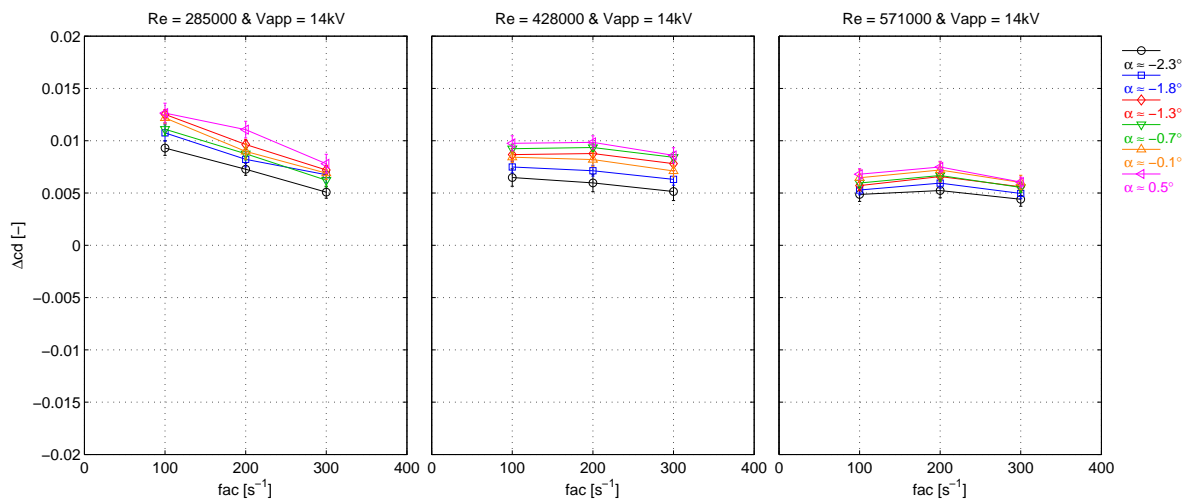


**Figure 5.23:** Change in drag coefficient against carrier frequency for different angles of attack and Reynolds numbers (flap above chord line)

### Reynolds number effect

From the data presented in figure 5.20 it is concluded that the effect of the Reynolds number is slightly less pronounced compared to the case with rounded trailing edge actuation, i.e. the decrease in lift with increasing Reynolds number is smaller. Nevertheless, the overall lift enhancement is still small at large Reynolds numbers.

## 5.2 Lift augmentation

In this section the effectiveness of the plasma actuator is calculated by using a method which is commonly used in applications involving slot blowing. In these applications blowing is performed

through a slot over a rounded trailing edge at approximately the same location as the gap of the plasma actuator at position A, see figure 4.9. The blowing efficiency in this method is expressed through the lift augmentation coefficient  $\Delta C_l/C_\mu$ . The  $C_\mu$  is the blowing momentum coefficient and is defined as the normalized thrust input[66, 14]:

$$C_\mu = \frac{T_m \cdot b_e}{q_\infty \cdot c \cdot b} \quad (5.1)$$

In which  $T_m$  is the thrust per unit span,  $b_e$  the effective width of the plasma actuator electrode and  $b$  the span of the airfoil.

An attempt is made to find the thrust per unit span produced by the plasma actuators used in this study. The method used is based on measurements of the velocity field in the vicinity of the plasma actuator, obtained by PIV[35]. The measured flowfields in quiescent flow conditions (no free stream velocity) are shown in figures 5.24 and 5.25 for the measured (uncorrected) angles of attack of  $0^\circ$  and  $12^\circ$ , or corrected values of  $0^\circ$  and  $7^\circ$ , respectively<sup>1</sup>. The typical wall jet associated with DBD plasma actuation is developed in both cases along the pressure side of the airfoil. The maximum achieved velocity is in the order of 3m/s.

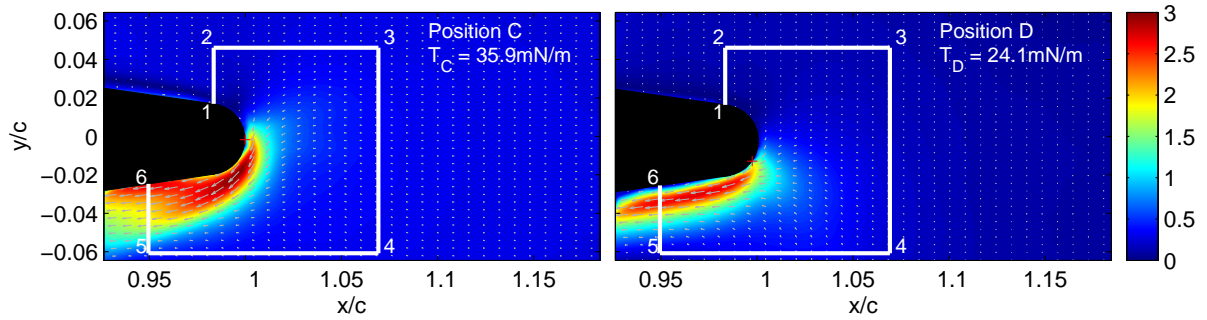


**Figure 5.24:** Mean velocity fields induced by plasma actuators C and D at an angle of attack of  $0^\circ$  and quiescent flow conditions. The + indicates the actuator gap position. The velocity is in m/s.

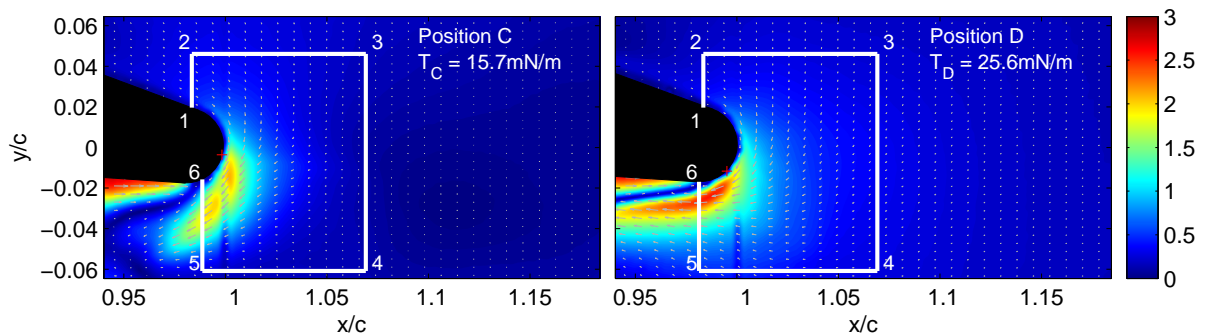


**Figure 5.25:** Mean velocity fields induced by plasma actuators C and D at an angle of attack of  $7^\circ$  and quiescent flow conditions. The + indicates the actuator gap position. The velocity is in m/s.

The method involves the definition of a control volume in the flow where the momentum flux is calculated at the boundaries of the domain and equilibrium with the internal forces is assumed.

<sup>1</sup>For all PIV figures and references to spatial dimensions and distances in this chapter, the origin of the coordinate system used is located at the trailing edge,  $x/c=1$  and  $y/c=0$ , with the x-axes always approximately parallel to the free stream velocity vector. References to the angle of attack refers to the corrected values, unless stated otherwise

This approach is well established in experimental and numerical investigations for the calculation of the aerodynamic drag of airfoils and wings[1]. In an experimental study by Hoskinson et al. in 2008 the same method was used for estimating the thrust of plasma actuators[24]. The calculated thrust includes both the body force from the actuator and the surface force acting on the airfoil. Applying the momentum balance equation on the specified control volumes gives:

$$\bar{T} = \oint_{123456} \rho \bar{U} (\bar{U} \cdot \bar{n}) dS - \oint_{123456} p \bar{n} dS \quad (5.2)$$

Where  $\bar{T}$  is the integrated thrust force (in x and y-direction) exerted on the fluid and  $\bar{n}$  is the wall normal unit vector. Equation 5.2 is developed for the boundaries taking into account the no-slip condition at the wall, which implies that the momentum flux across the wall is zero. Note that the wall unit vector is defined in the direction pointing away from the control volume, resulting in a positive momentum when flow is moving out of the control volume. The momentum balance in x and y-direction are defined as follows:

- In x-direction

$$\begin{aligned} T_x = & -\rho \int_{12} u_x^2 dy + \rho \int_{23} u_x u_y dx + \rho \int_{34} u_x^2 dy - \rho \int_{45} u_x u_y dx \\ & -\rho \int_{56} u_x^2 dy + \int_{12} p dy - \int_{34} p dy + \int_{56} p dy - \int_{16} (pdS)_x \end{aligned} \quad (5.3)$$

- In y-direction

$$\begin{aligned} T_y = & -\rho \int_{12} u_x u_y dy + \rho \int_{23} u_y^2 dx + \rho \int_{34} u_x u_y dy - \rho \int_{45} u_y^2 dx \\ & -\rho \int_{56} u_x u_y dy - \int_{23} p dx + \int_{45} p dx - \int_{16} (pdS)_y \end{aligned} \quad (5.4)$$

Due to the fact that the pressure is not readily available from the velocity data, a further assumption needs to be made for the calculation of the momentum budget. This states that if the control volume boundaries are far enough from the ionisation region (near the exposed electrode edge) the static pressures at the boundaries can be considered uniform and equal. Similar assumption is typically made in the case of airfoil drag estimation. It should also be noted here that the calculated forces ( $T_x$  and  $T_y$ ) also contain the surface force (shear and pressure forces) between the flow and the surface ( $T_x^s$  and  $T_y^s$ ). These assumptions reduce equations 5.3 and 5.4 to:

- In x-direction

$$T_x^p + T_x^s = -\rho \int_{12} u_x^2 dy + \rho \int_{23} u_x u_y dx + \rho \int_{34} u_x^2 dy - \rho \int_{45} u_x u_y dx - \rho \int_{56} u_x^2 dy \quad (5.5)$$

- In y-direction

$$T_y^p + T_y^s = -\rho \int_{12} u_x u_y dy + \rho \int_{23} u_y^2 dx + \rho \int_{34} u_x u_y dy - \rho \int_{45} u_y^2 dx - \rho \int_{56} u_x u_y dy \quad (5.6)$$

The obtained momentum balance equations are applied to the control volumes in figures 5.24 and 5.25. The magnitude of the total thrust is given in the top right corner of the corresponding velocity fields.

At this point it should be stated that the gap size and gap positions of plasma actuator D are exactly the same in figure 5.24 and 5.25. Whereas the electrodes of plasma actuator C are removed and reapplied between the two figures. This is due to the choice made not to change the high speed camera position twice, since each change requires a new calibration. Besides this, the angle of attack needs to be set manually, causing it to be different after every change (in  $\alpha$  and/or actuator). It is shown in figures 5.24 and 5.25 that changing the actuator has a large effect on the measured/calculated thrust. This is attributed to three things. Firstly, the largest part of this is most probably caused by the change in electrode positions, and the following gap size. Secondly, it can be caused by the fact that the airfoil creates a shadow in the laser sheet (coming from the left in the figures) at a measured angle of attack of  $12^\circ$ . This results in the errors in the data in the small triangle below the airfoil in figure 5.25. The shadowing forced the control volume boundary on the bottom left to be closer to the ionisation region. Finally, it was found that the reflections of the laser on the airfoil were quite large in the  $12^\circ$  case, causing a vertical line at  $x/c=1$  with small errors in the velocity data. The last effect is considered to be negligible with respect to the other two, because the errors are small and the corresponding velocity data has almost no contribution to the momentum balance.

The thrust per unit span that will be used is 2.63g/m or 25.8mN/m, which the average of the values of thrust found for plasma actuator D. The value is comparable to the value 3.1g/m or 30.4mN/m found by Kotsonis[36] for the same plasma actuator settings but for a flat plasma actuator instead of an actuator with curved electrodes, as used in this study. This value is obtained by a load cell measurement, which relies on the direct measurement of the reaction force due to the acceleration of the fluid from the plasma operation. As with the momentum balance method, the value of the thrust obtained here also includes the surface force created by the induced jet flow over the airfoil surface.

The lift augmentation values are calculated and presented in tables 5.1, 5.2 and 5.3. Table 5.1 shows the lift augmentation at an angle of attack of approximately zero. The second table shows the maximum obtained increase in  $\Delta c_l$  in the range of angle of attack where no stall occurs and finally the average lift augmentation in this angle of attack range is shown in table 5.3.

V [m/s]	$C_\mu$ [-]	$\Delta c_{l,\alpha=0}$		$\Delta c_{l,\alpha=0}/C_\mu$	
		max (Position)	min (Position)	max (Position)	min (Position)
10	$13.7 \cdot 10^{-4}$	0.0769 (C)	0.0639 (A)	55.5 (C)	47.3 (A)
15	$6.2 \cdot 10^{-4}$	0.0352 (E)	0.0272 (A)	56.8 (E)	44.8 (A)
20	$3.6 \cdot 10^{-4}$	0.0256 (E)	0.0161 (C)	73.5 (E)	46.2 (C)

**Table 5.1:** Maximum and minimum  $\Delta c_l$  and corresponding lift augmentation values at an angle of attack of approximately zero.

The blowing momentum coefficient is used as a measure for the ratio of the thrust generated by the jet and the dynamic pressure times the reference wing area. In case of a plasma actuator the thrust can be measured using a flat plate actuator and a balance or the momentum balance method used in this study. The momentum coefficient is very small for plasma actuators due to the low velocity input. With the measured increase in lift coefficient this results in a large lift augmentation

V [m/s]	$C_\mu$ [-]	$\Delta c_{l,max}$		$\Delta c_{l,max}/C_\mu$	
		max (Position)	min (Position)	max (Position)	min (Position)
10	$13.7 \cdot 10^{-4}$	0.1486 (D)	0.0837 (A)	106.7 (D)	61.0 (A)
15	$6.2 \cdot 10^{-4}$	0.0760 (E)	0.0375 (A)	120.1 (E)	60.9 (A)
20	$3.6 \cdot 10^{-4}$	0.0396 (D)	0.0191 (A)	112.3 (D)	54.2 (A)

**Table 5.2:** Maximum and minimum obtained  $\Delta c_l$  and corresponding lift augmentation in the range of angle of attack where no stall occurs.

V [m/s]	$C_\mu$ [-]	$\Delta c_{l,ave}$		$\Delta c_{l,ave}/C_\mu$	
		max (Position)	min (Position)	max (Position)	min (Position)
10	$13.7 \cdot 10^{-4}$	0.1001 (D)	0.0688 (A)	72.4 (D)	50.5 (A)
15	$6.2 \cdot 10^{-4}$	0.0378 (D)	0.0264 (A)	61.0 (D)	42.8 (A)
20	$3.6 \cdot 10^{-4}$	0.0242 (E)	0.0114 (C)	68.9 (E)	32.4 (C)

**Table 5.3:** Maximum and minimum obtained average  $\Delta c_l$  and corresponding lift augmentation values in the range of angle of attack where no stall occurs.

coefficient. For an angle of attack of  $0^\circ$ , table 5.1 shows the maximum lift augmentation coefficient. The value lies in the range 55–75, depending on the free stream velocity and actuator position. From table 5.3 it follows that the maximum average lift augmentation coefficient lies around 60–75 in the angle of attack range of  $0$ – $10^\circ$ , depending on the configuration and the free stream velocity. In the same way the maximum obtained lift augmentation coefficient for a single angle of attack lies in the range 105–120. From this table it follows that at 15m/s the plasma actuator at position E produces lift augmentations as high as 120 times the relative momentum input by the actuator itself, see table 5.2. Compared to data found in literature, where in case of blowing lift augmentation coefficients up to 80 are recorded[66], it is concluded that the method used in the current work is very effective in increasing lift. However, the absolute increase in lift coefficient obtained is very low and potentially can be used for active load control only after careful upscaling.

## 5.3 PIV flow field measurements

During the second experimental campaign particle image velocimetry was applied in order to characterize the flow field around the trailing edge. Selected actuator configurations, angles of attack and Reynolds numbers were tested as indicated in table 4.7. By the use of Davis 8.1.3 (Lavision GmbH) the mean velocity field, mean turbulent kinetic energy and mean Reynolds shear stress are calculated. The mean velocity data in the wake is analysed and an attempt is made to characterize the effectiveness of the plasma actuators from the obtained results. In this section only the data for a Reynolds number of  $1.46 \cdot 10^5$  is presented. The results for  $Re = 2.19 \cdot 10^5$  can be found in appendix B (for field data) and appendix C (for the wake data). See section 4.5 for more information on the experimental set-up, selected actuator configurations and parameters used in this experiment.

### 5.3.1 Mean velocity field

The flow fields around the rounded trailing edge were obtained for measured angles of attack,  $\alpha_t$ , of  $0^\circ$  and  $12^\circ$ , corresponding to an effective or corrected angle of attack,  $\alpha$ , around  $0^\circ$  and  $7^\circ$ . For Reynolds number of  $1.46 \cdot 10^5$  the mean velocity fields are plotted in figures 5.26 and 5.27, for angles of attack  $0^\circ$  and  $7^\circ$ .

Flow streamlines (and/or particle pathlines in case of steady/mean flow fields) are shown in the same figures. In all cases were the plasma actuator is off the flow field appears as typical for blunt

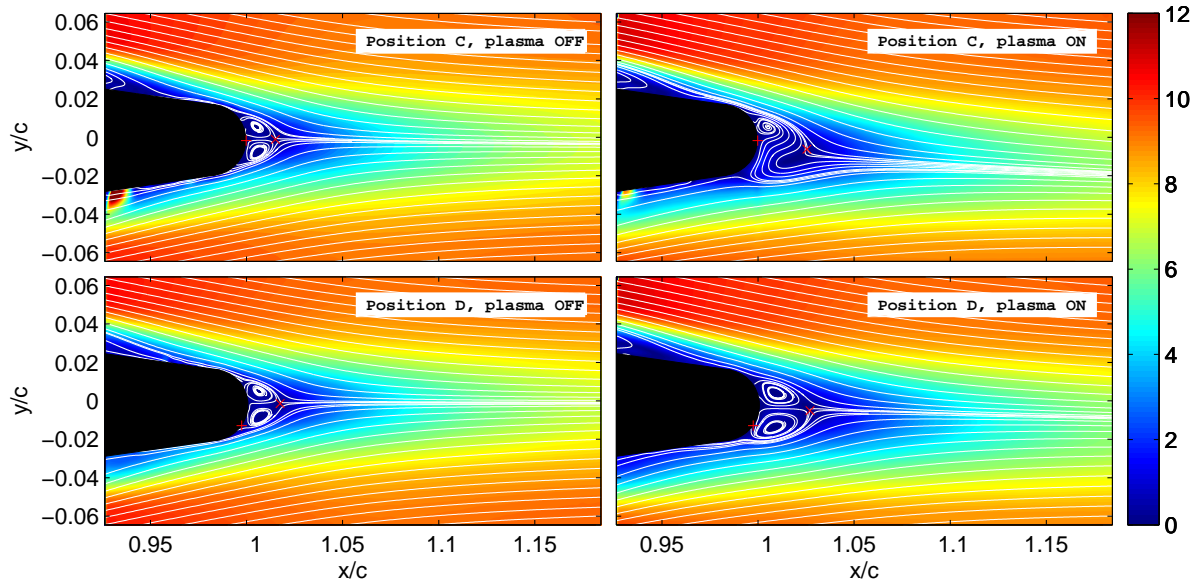


**Figure 5.26:** Mean velocity fields produced by plasma actuators C and D (on and off) at an angle of attack of  $0^\circ$  and Reynolds number  $1.46 \cdot 10^5$ . The + indicates the actuator gap position, the x indicates the location of the saddle point. The velocity is in m/s.

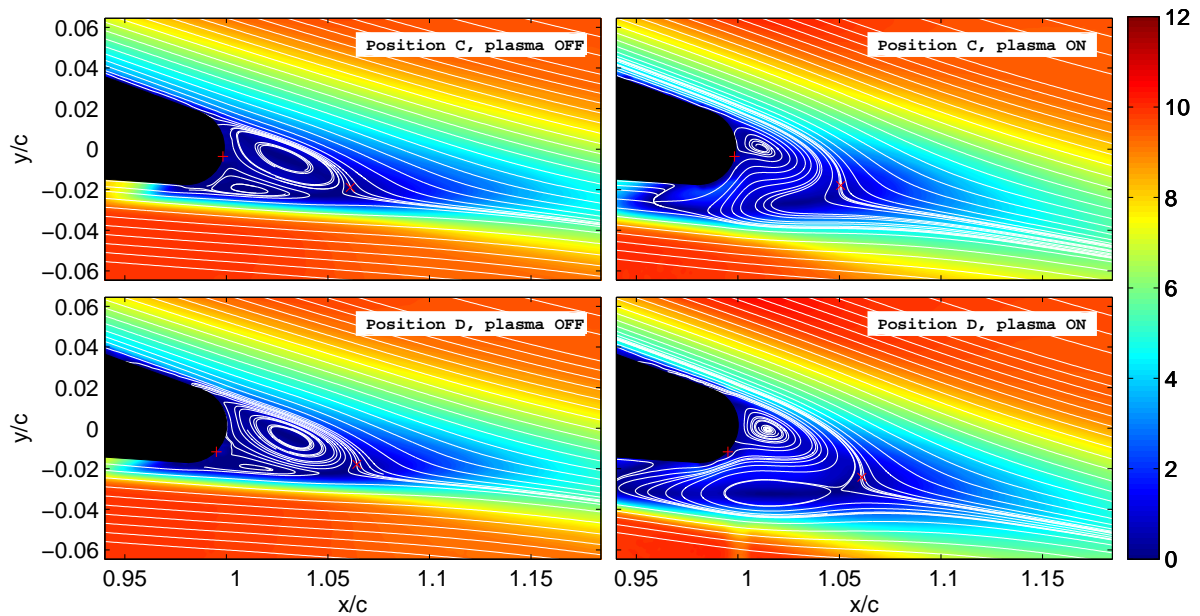


**Figure 5.27:** Mean velocity fields produced by plasma actuators C and D (on and off) at an angle of attack of  $7^\circ$  and Reynolds number  $1.46 \cdot 10^5$ . The + indicates the actuator gap position, the x indicates the location of the saddle point. The velocity is in m/s.

trailing edge airfoils with two counter-rotating vorticity areas right behind the trailing edge. At  $0^\circ$  the wake of the airfoil is symmetrical to the extended chord line while a saddle point is formed at approximately  $x/c=1.016$  downstream of the trailing edge for both plasma actuators. In order to evaluate the effectiveness of the plasma actuators for lift augmentation a metric is needed for assessing the change in streamline topologies between the actuator off and on cases. The same is done with the lift augmentation coefficient based on the force measurements in the previous section. The curvature of the rounded trailing edge does not allow for a direct use of the location of the Kutta condition, since it is too unsteady to determine it precisely. Meaning that the Kutta condition can not be used as a metric. Due to this a different approach is followed, similar to Gurney flap studies, where one of the used metrics for the effectiveness of lift augmentation is the displacement of the saddle point between actuator on and off[18]. The x-coordinate of the saddle point is determined by the distance from the trailing edge where the x-component of the velocity becomes positive everywhere (in y-direction). The y-coordinate of the saddle point corresponds to the location of minimum velocity (x-component). Table 5.4 shows the coordinates of the saddle points, normalized by the airfoil chord length, and the difference between actuator on and off for both plasma actuators and both angles of attack and Reynolds numbers. In this table  $r_{lx}$  is the recirculation length of the wake, the point where all velocity vectors (in y-direction) become positive. The  $r_{ly}$  indicates the location in y-direction where the maximum velocity deficit is found, i.e. the centre of the wake. Please note again that the x-axes of the coordinate system used in PIV results is always approximately parallel to the free stream velocity vector and not parallel to the airfoil chord.

**Table 5.4:** Table showing the coordinates of the saddle points, normalized by the airfoil chord length, and the difference between actuator on and off for both plasma actuators and both angles of attack and Reynolds numbers.

			plasma OFF		plasma ON		$\Delta r_l$	
			Pos. C	Pos. D	Pos. C	Pos. D	Pos. C	Pos. D
$\alpha = 0^\circ$	$Re = 1.46 \cdot 10^5$	$r_{lx}$	0.0151	0.0175	0.0254	0.0270	0.0103	0.0095
		$r_{ly}$	-0.0010	-0.0014	-0.0062	-0.0051	-0.0052	-0.0037
	$Re = 2.19 \cdot 10^5$	$r_{lx}$	0.0318	0.0334	0.0334	0.0342	0.0016	0.0008
		$r_{ly}$	-0.0012	-0.0018	-0.0021	-0.0025	-0.0009	-0.0007
$\alpha = 7^\circ$	$Re = 1.46 \cdot 10^5$	$r_{lx}$	0.0610	0.0642	0.0506	0.0610	-0.0104	-0.0032
		$r_{ly}$	-0.0188	-0.0178	-0.0179	-0.0242	0.0009	-0.0064
	$Re = 2.19 \cdot 10^5$	$r_{lx}$	0.0473	0.0465	0.0345	0.0329	-0.0128	-0.0136
		$r_{ly}$	-0.0107	-0.0092	-0.0077	-0.0065	0.0030	0.0027

Table 5.4 shows a clear difference in the effect of the plasma actuator on the saddle point between both angles of attack. At  $0^\circ$  the plasma actuators effectively increase the recirculation length of the wake while the centre of the wake is moved slightly down. The latter is as expected in case the Kutta condition is moved down, to the pressure side of the airfoil. Indicating that the plasma actuator is in fact capable of moving the Kutta condition downwards and increase the circulation and lift. The reason why the actuator at position C is more effective at  $0^\circ$  can be found in figure 5.26. This figure shows the working principle of the plasma actuator. For position C the actuator is disrupting the recirculation region, especially on the lower half of the trailing edge. The saddle point as well as the wake are clearly displaced downwards. The actuator at position D has a similar effect, although less pronounced in the recirculation region. The effect of the plasma jet enlarges the lower counter-clockwise vortex and moves the wake slightly downward. The higher effectiveness of actuator C in displacing the saddle point is shown here in the flow topology, but it is also in agreement with the force measurements at  $0^\circ$ , as shown in figure 5.5. The reason for the difference in performance between the two positions is apparently the relative position of the actuator to the recirculation region. The actuator at position C is located in a region dominated by low velocity close to the rear stagnation point, whereas actuator D is located almost

in the boundary layer coming from the pressure side of the airfoil. Due to this difference the jet produced by actuator C can interact with the vortex pair in the wake while the jet produced by actuator D is engulfed by the free stream flow. It appears that the actuator at position C has a more favorable position to interact with the vortex pair, resulting in a higher effectiveness as compared to actuator D. The results in appendix B again show that at higher Reynolds number, i.e.  $Re=2.19 \cdot 10^5$ , the effectiveness of the plasma actuators is reduced considerably. The metric in table 5.4 for  $0^\circ$  still shows the same effect as with lower Reynolds number, however the changes are an order of magnitude smaller.

The second angle of attack that is tested is  $7^\circ$ . At this angle of attack it is found that both plasma actuators effectively decrease the recirculation length, opposite to the  $0^\circ$  case, as presented in table 5.4. From the actuator off case in figure 5.27 it can be seen that now both plasma actuators are positioned in the low velocity region of the wake. The suggested higher effectiveness is directly found in the actuator on case on the right hand side. Both plasma actuators are disrupting the recirculation region on the lower side and move the wake downwards. It seems that in the  $7^\circ$  case the disruption of the recirculation region is the reason why the length of the recirculation region is decreasing. Unfortunately the data on vertical location of the saddle point in table 5.4 is in this case not a good metric for the effectiveness of the plasma actuators, since the majority of the values are positive while the wake clearly moves down for both Reynolds numbers (see appendix B). This is attributed to the spatial resolution of the velocity data in the PIV results. A point that can be made with figure 5.27 is that the direction of the streamlines at the actuator positions, indicated with the +, clearly coincide with the expected direction of the plasma jets. It follows that the more upstream directed jet created by plasma actuator D has a larger effect on the flow topology, as compared to position C. At this angle of attack the plasma actuator at position D seems to be closer to the rear stagnation point of the airfoil, as was stated before this is favourable with respect to the interaction with the vortex pair behind the airfoil. This also corresponds to the force measurements at  $7^\circ$ , as shown in figure 5.5, where the actuator at position D has a larger effect on the lift.

The trends regarding the effects of actuator positioning and angle of attack, as seen in force measurements (section 5.1.1) and PIV results (section 5.3), suggest that several mechanisms are influencing the airfoil circulation control. Firstly, the best performing (tested) positions D and E are located on the pressure side of the airfoil where the boundary layer is considerably thinner than on the suction side (in case of a positive angle of attack). This effectively places the actuator closer to an area of high momentum. In combination with the velocity jet produced by the plasma actuators, which are directed upstream in case of position D and E, it seems that it produces an higher influence on the high momentum flow. In other words, the velocity jet of the plasma actuator can 'penetrate' the boundary layer further. The higher effectiveness is explained by the smaller distance between the actuator location and the high momentum flow, resulting in a lower diffusion of the induced velocity field, as compared to actuator position C. At this point it should be added that this only holds in cases where the angle of attack is considerably higher than  $0^\circ$ , since at  $0^\circ$  point E and D are considered to be positioned too far upstream, such that the velocity jet is not able to fully develop and interaction with the wake vortex is not possible.

Secondly, as was suggested before, the relative position of the actuator with respect to the strong recirculation areas behind the airfoil is also a mechanism that seems to play a role. The occurring recirculation area is inherent to airfoils with truncated or blunt trailing edges. The relative large thickness of the trailing edge in this case is expected to produce a pair of counter-rotating vortices either alternating or simultaneously shed. At higher angles of attack the positions D and E are located in the neighbourhood of the counter-clockwise rotating vortex on the lower side of the airfoil. The induced velocity by the plasma actuators is directed in the same direction, which can be beneficial to the effectiveness of the actuators. In other words, it looks like the plasma actua-

tor is disrupting the vortex pair in the wake and redirecting some of the momentum stored in them.

Finally, through careful observation of the results an important conclusion can be stated for the general lift enhancement using plasma actuators. Firstly, it can be assumed that the momentum input due to the plasma actuation is independent of the positioning of the plasma actuator. This is a valid assumption since the exposed electrode thickness, covered electrode length, applied voltage, actuation frequency and dielectric thickness stay constant. Taking this into account it can be safely conducted that the lift enhancement is indeed due to manipulation of the Kutta condition. If the plasma actuator's effect was a simple increase in circulation due to the local induced momentum input (independent of the plasma actuator positioning) then the lift enhancement would be constant for any given position of the actuator and angle of attack. This is explained further with a short calculation. The thrust per unit span of an electrode is approximately equal to 3.1g/m or 30.4mN/m, as found by Kotsonis[36]. The thrust for an effective electrode length of  $b_e=0.4\text{m}$  is than:

$$T = 30.4 \cdot 10^{-3} \cdot 0.4 = 0.0122\text{N} \quad (5.7)$$

This thrust force can be approximated by a momentum flux through a 2D surface, using the same principle as in section 5.2 but assuming that the only contribution to the momentum balance is from the one surface crossing the plasma velocity jet. An reasonable assumption based on results from Kotsonis[35]. Further assuming an uniform velocity over this surface results to the following:

$$\begin{aligned} T &= \rho \cdot u_{\perp}^2 \cdot t \cdot w \\ \Rightarrow u_{\perp} &= \sqrt{\frac{T}{\rho \cdot t \cdot w}} = 4.98\text{m/s} \end{aligned} \quad (5.8)$$

Where  $t=1\text{mm}$  is the approximate height of the plasma jet. The next step is to equate the momentum obtained with this velocity with a momentum in case of a velocity parallel to the airfoil surface  $u_{\parallel}$  over an estimated surface length  $s=10\text{mm}$ :

$$\begin{aligned} \rho \cdot u_{\perp}^2 \cdot t \cdot w &= \rho \cdot u_{\parallel}^2 \cdot s \cdot w \\ \Rightarrow u_{\parallel} &= \sqrt{\frac{\rho \cdot u_{\perp}^2 \cdot t \cdot w}{\rho \cdot s \cdot w}} = 1.58\text{m/s} \end{aligned} \quad (5.9)$$

With this velocity the additional circulation due to the plasma jet can be approximated:

$$\Delta\Gamma = u_{\parallel} \cdot s = 0.0158\text{m}^2/\text{s} \quad (5.10)$$

And finally, with the increase in circulation the change in lift coefficient can be calculated, in case of a free stream of 10m/s this then becomes:

$$\Delta c_l = \frac{\Delta\Gamma \cdot b_e}{\frac{1}{2}U_{\infty} \cdot b \cdot c} = 0.0104 \quad (5.11)$$

The corresponding value for free stream velocities of 15m/s and 20m/s are 0.0069 and 0.0052, respectively. With respect to the average values found for the change in lift coefficient from

the force measurements, as presented in table 5.3, the added circulation due to the induced momentum input accounts for 10.4%, 18.3% and 21.5% of the total increase in  $\Delta c_l$ . This supports the statement made earlier that the lift enhancement is due to manipulation of the Kutta condition on the rounded trailing edge. At the same time it also shows that the decrease in effectiveness of the plasma actuator for increasing Reynolds number is mostly due to the constant momentum input of the plasma actuator, independent of flow conditions.

### 5.3.2 Mean turbulent kinetic energy

Additionally to the mean velocity fields also the mean turbulent kinetic energy distributions in the wake are calculated. The resulting distributions are shown in figures 5.28 and 5.29 for angles of attack of  $0^\circ$  and  $7^\circ$ , respectively.

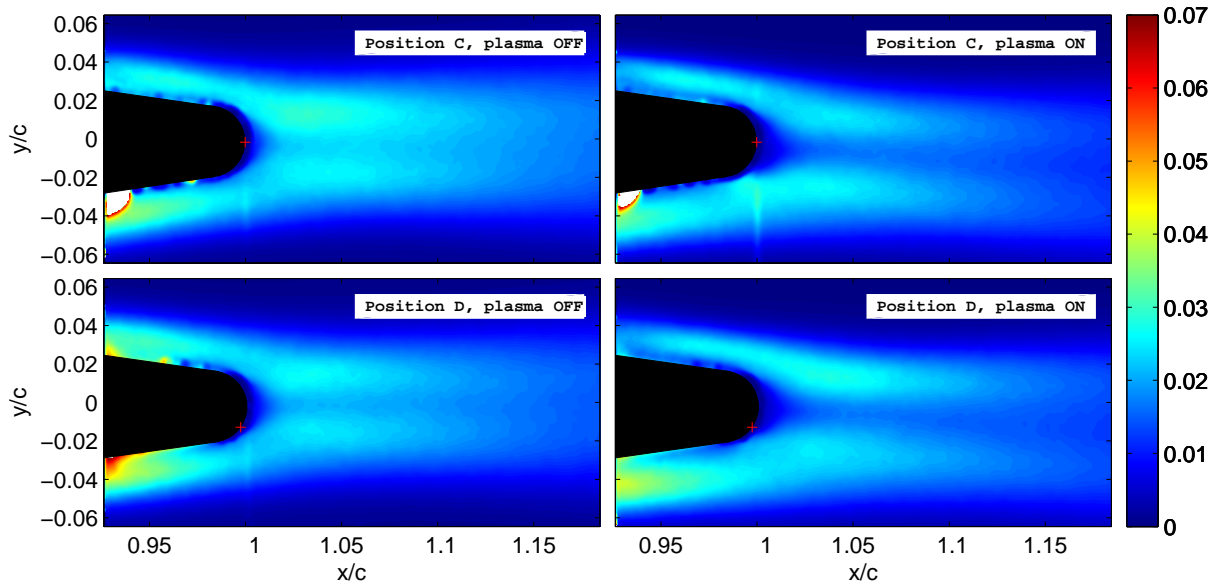


**Figure 5.28:** Turbulent kinetic energy fields produced by plasma actuators C and D (on and off) at an angle of attack of  $0^\circ$  and Reynolds number  $1.46 \cdot 10^5$ . The + indicates the actuator gap position. Turbulent kinetic energy in  $0.5(\overline{u'_x u'_x} + \overline{u'_y u'_y})/U_\infty^2$ .

The turbulent kinetic energy is normalized with the free stream velocity and defined as:

$$\frac{k}{U_\infty^2} = \frac{\frac{1}{2}(\overline{u'_x u'_x} + \overline{u'_y u'_y})}{U_\infty^2} \quad (5.12)$$

In which  $u'_x$  and  $u'_y$  are the fluctuating parts of the flow velocity in x and y-direction, respectively, as defined by the Reynolds decomposition:

$$u_i = \overline{u_i} + u'_i \quad (5.13)$$

The definition of the turbulent kinetic energy indicates that it is measure for the strength of the velocity fluctuations in the flow, or turbulence. Figure 5.28 shows the turbulent kinetic energy distribution for  $0^\circ$ . Besides the deflection of the wake, as discussed before, two new effects of the plasma actuator are noted here. Firstly, the impingement of the plasma jet of plasma actuator C

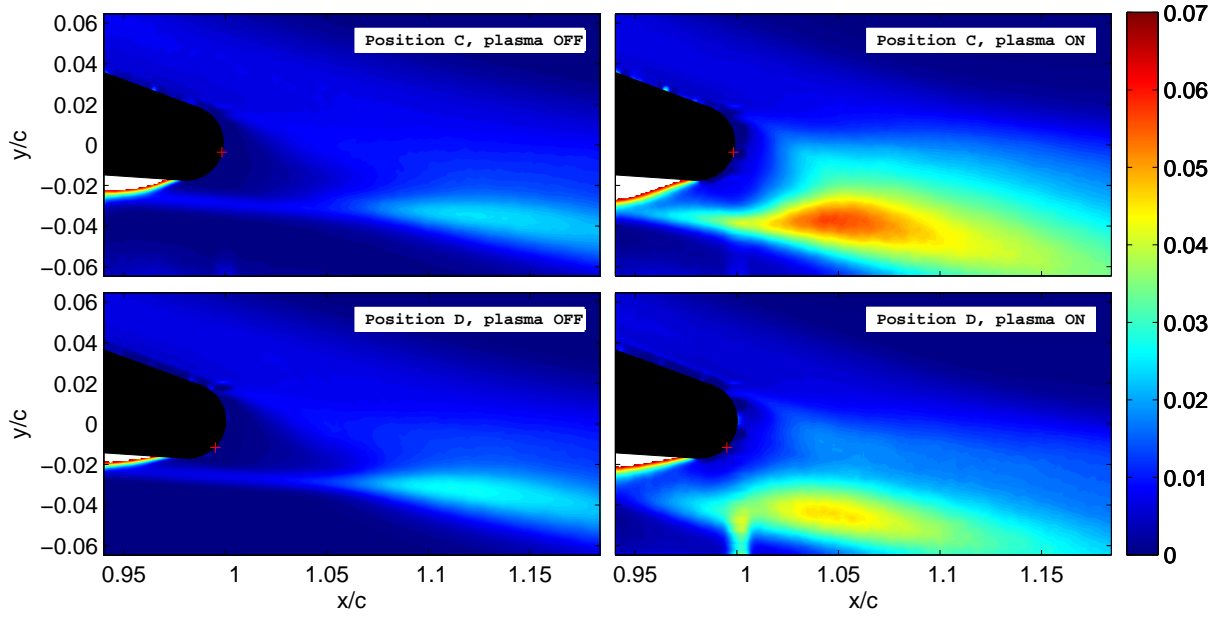


**Figure 5.29:** Turbulent kinetic energy fields produced by plasma actuators C and D (on and off) at an angle of attack of  $7^\circ$  and Reynolds number  $1.46 \cdot 10^5$ . The + indicates the actuator gap position. Turbulent kinetic energy in  $0.5(\overline{u'_x u'_x} + \overline{u'_y u'_y})/U_\infty^2$ .

with the free flow coming from the pressure side of the airfoil is visible. The location coincides with the point where the streamlines in figure 5.26 are bend to follow the free stream flow. The turbulent kinetic energy is slightly increase at this location. The second effect is the lower turbulent kinetic energy at the centre of the wake in the case with plasma actuation, present for both plasma actuator positions. This effect is contributed to the possible change in strength of the vortex pair in the recirculation region of the wake, due to the interaction with the plasma actuator jet.

For the  $7^\circ$  case a stronger effect is found in the turbulence kinetic energy distribution. Due to the larger effectiveness of both plasma actuator jets on the flow topology behind the rounded trailing edge, as found from the streamlines in figure 5.27, the interaction with the free stream flow is expected to be larger. The results indeed show an increase in turbulence on the lower side of the wake in the region after the collision of the jet with the main flow. The obvious increase in turbulence at this angle of attack coincides with the increase in drag coefficient at the same angle of attack as found during the force measurements, see figure 5.7.

### 5.3.3 Mean Reynolds shear stress

Finally, the mean Reynolds shear stress distributions in the wake of the rounded trailing edge model are shown in figures 5.30 and 5.31 for angles of attack of  $0^\circ$  and  $7^\circ$ , respectively.

Notice the difference in plotted data range when comparing the two angle of attack cases. The Reynolds shear stress shown is normalized with the free stream velocity and is defined as follows:

$$\frac{Re_{xy}}{U_\infty^2} = \frac{\overline{\rho u'_x u'_y}}{U_\infty^2} \quad (5.14)$$

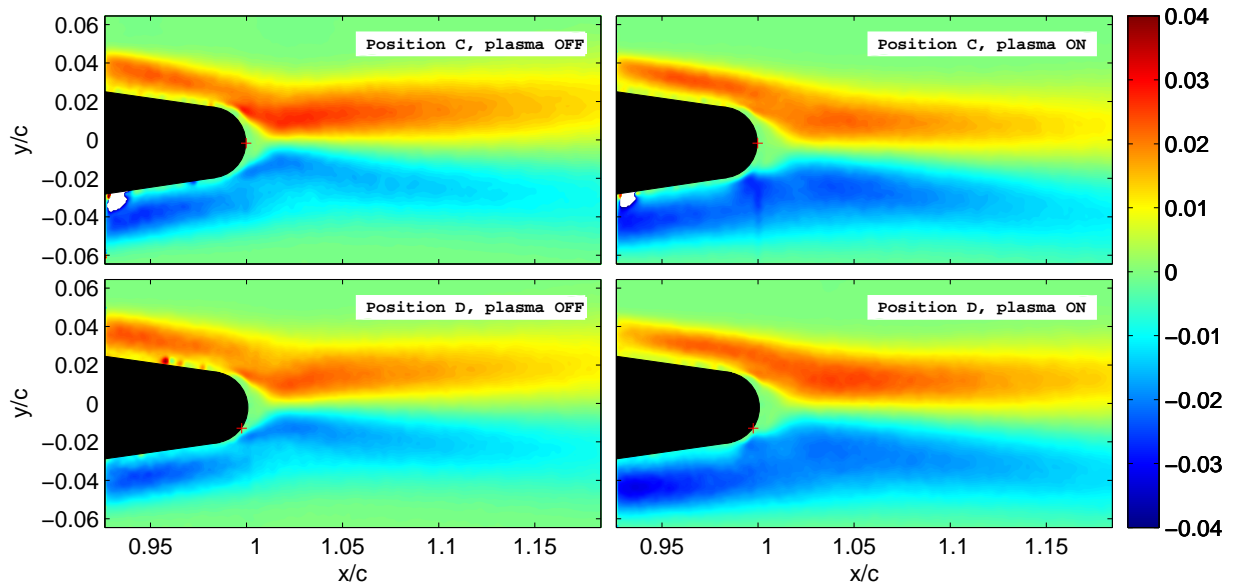


**Figure 5.30:** Average Reynolds stress fields produced by plasma actuators C and D (on and off) at an angle of attack of  $0^\circ$  and Reynolds number  $1.46 \cdot 10^5$ . The + indicates the actuator gap position. Average Reynolds shear stress fields in  $\overline{\rho u'_x u'_y} / U_\infty^2$ .

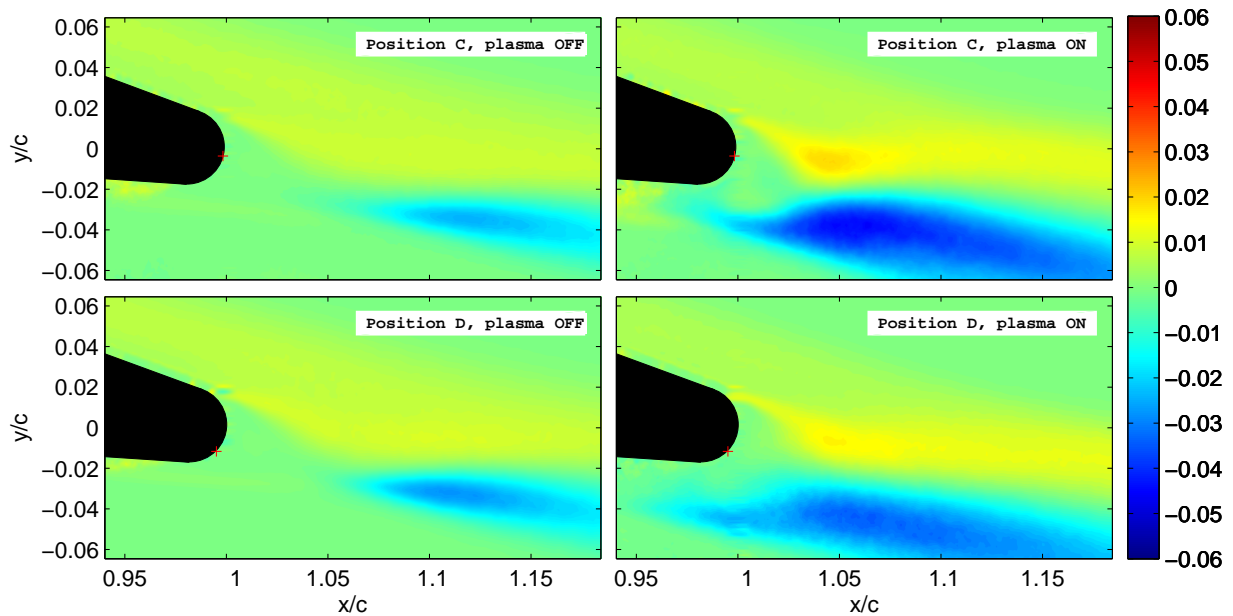


**Figure 5.31:** Average Reynolds stress fields produced by plasma actuators C and D (on and off) at an angle of attack of  $7^\circ$  and Reynolds number  $1.46 \cdot 10^5$ . The + indicates the actuator gap position. Average Reynolds shear stress fields in  $\overline{\rho u'_x u'_y} / U_\infty^2$ .

The Reynolds shear stress component shown here is a coefficient that plays an important role in the production of turbulence. It is therefore used as measure for the turbulence production. The figures shown here are therefore closely related to the turbulent kinetic energy presented in figures 5.28 and 5.29. The impingement of the plasma induced jet with the free flow is now visible for both plasma actuators in the  $0^\circ$  case. Additionally, the same figure shows an increase in boundary layer thickness on the pressure side of the airfoil, while on the suction side no change is noticed. This indicates that the plasma actuators are in fact influencing the flow upstream of the point of actuation. This is supporting the statement that the plasma actuators are changing the Kutta condition of the airfoil.

### 5.3.4 Wake analysis

In addition to the field data presented in previous sections, also the wake of the airfoil is analysed. In this section some typical wake characteristics are presented that are derived from the mean velocity data in figures 5.26 and 5.27. The velocity distribution in the wake (wake shape), the streamwise location of the maximum velocity deficit (wake location) and the streamwise distribution of the wake half-width (wake width) are presented in subsequent sections.

#### Wake shape

Figures 5.32 and 5.33 show the streamwise velocity component distribution at four different streamwise stations in the wake at an angle of attack of  $0^\circ$  and  $7^\circ$ , respectively. The selected stations are located at approximately  $x/c=0.03$ ,  $0.08$ ,  $0.13$  and  $0.18$  behind the trailing edge of airfoil.

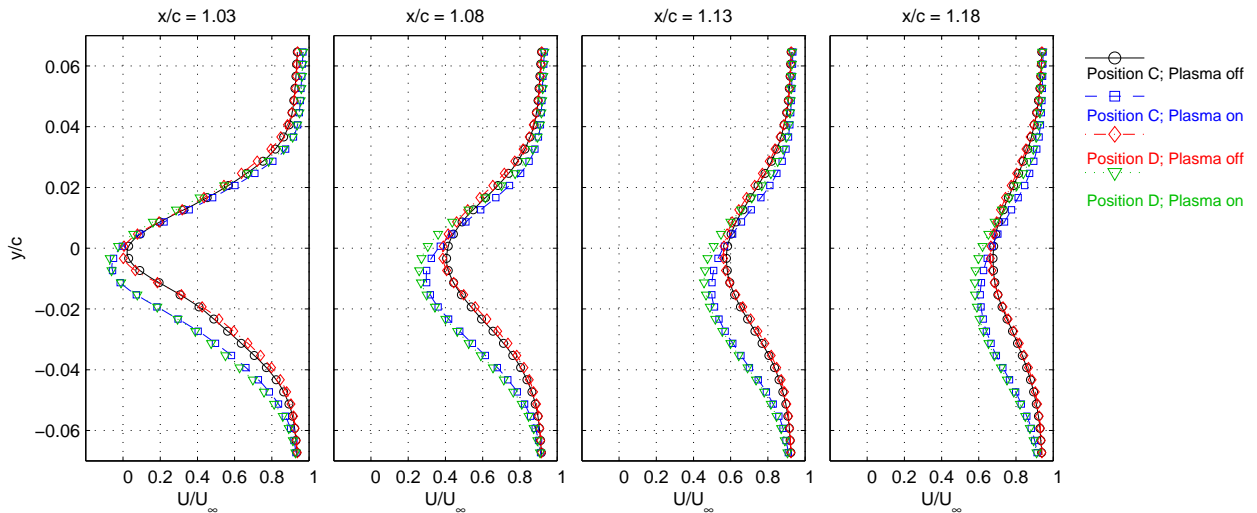


**Figure 5.32:** Vertical distribution of the time-averaged streamwise velocity component ( $u_x$ ) produced by plasma actuators C and D (on and off) at an angle of attack of  $0^\circ$  and Reynolds number  $1.46 \cdot 10^5$ .

These figures show a fuller velocity deficit distribution in both angle of attack cases, which is indicative of the increase in the measured drag coefficient. In addition to this it is again clear that the plasma actuators are displacing the wake in downward direction, since the wake centre (the point of maximum velocity deficit) is moved down. This effect is better visible when plotting the streamwise distribution of the maximum velocity deficit point.

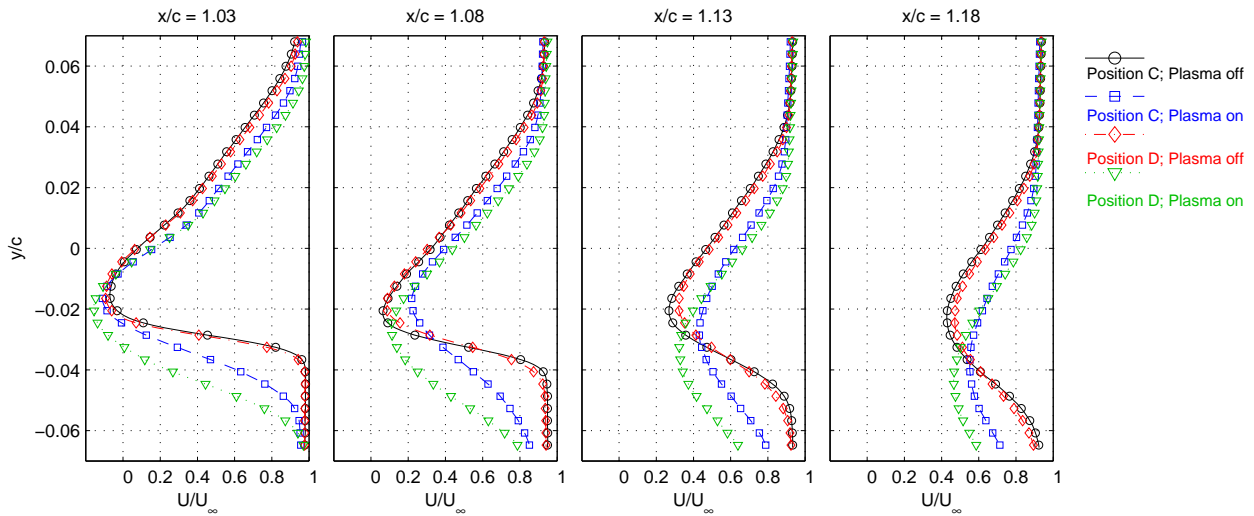


**Figure 5.33:** Vertical distribution of the time-averaged streamwise velocity component ( $u_x$ ) produced by plasma actuators C and D (on and off) at an angle of attack of  $7^\circ$  and Reynolds number  $1.46 \cdot 10^5$ .

### Wake location

Figures 5.34 and 5.35 show the locations of the wake in streamwise direction for all actuator on and off cases and at angles of attack of  $0^\circ$  and  $7^\circ$ , respectively.

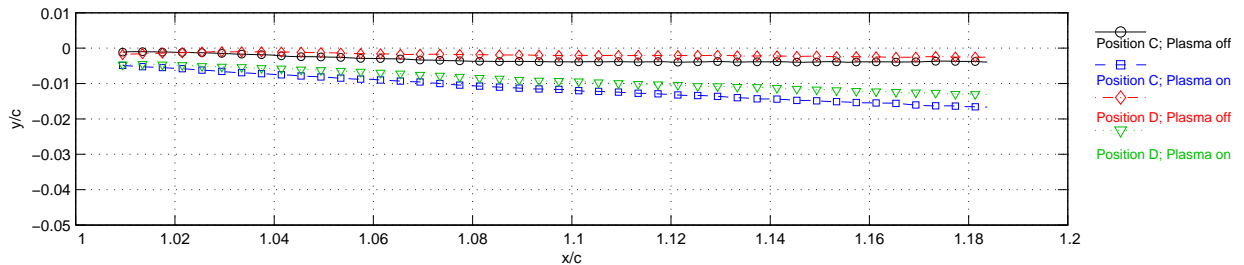


**Figure 5.34:** Location of the maximum streamwise velocity deficit in the wake as produced by plasma actuators C and D (on and off) at an angle of attack of  $0^\circ$  and Reynolds number  $1.46 \cdot 10^5$ .

The results are in accordance with the change in lift coefficient in figure 5.5. The wake deflection is in this case a good metric in determining the effectiveness of the plasma actuation. Table 5.5 shows the calculated wake deflections. The wake deflection presented here is the angle between the wake position in  $y$ -direction at  $x/c=0.18$  and the  $x$ -axes of the coordinate system used in the PIV data, with the origin approximately at the trailing edge of the airfoil.

From table 5.5 it follows that the change in wake deflection  $\Delta\theta_w$  and the change in measured lift coefficient  $\Delta c_l$  from the force measurements are closely related. This supports the statement that the plasma actuator is changing the Kutta condition on the rounded trailing edge. The wake deflection is used as measure for the change in the Kutta condition, the stagnation point is moved down to the pressure side of the airfoil. Due to this the total circulation on the airfoil is increased and since the circulation is related to the lift coefficient via equation 5.11, it can be said that the lift generated by the airfoil is increased.

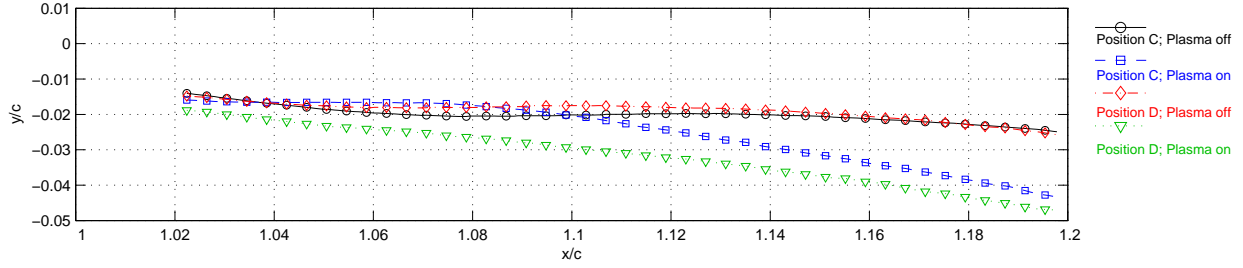


**Figure 5.35:** Location of the maximum streamwise velocity deficit in the wake as produced by plasma actuators C and D (on and off) at an angle of attack of  $7^\circ$  and Reynolds number  $1.46 \cdot 10^5$ .

**Table 5.5:** An overview of the calculated wake deflections  $\theta_w$  for plasma off and on and the corresponding change  $\Delta\theta_w$ , the angle is in degrees. Added are the  $\Delta c_l$  values obtained by force measurements, extracted from figure 5.5.

		plasma OFF		plasma ON		$\Delta\theta_w$		$\Delta c_l$	
		Pos. C	Pos. D	Pos. C	Pos. D	Pos. C	Pos. D	Pos. C	Pos. D
$\alpha = 0^\circ$	$Re = 1.46 \cdot 10^5$	1.19	0.80	5.24	4.12	4.05	3.32	0.077	0.068
	$Re = 2.19 \cdot 10^5$	0.78	0.88	1.37	1.51	0.59	0.63	0.016	0.024
$\alpha = 7^\circ$	$Re = 1.46 \cdot 10^5$	7.60	7.34	12.22	13.35	4.62	6.01	0.126	0.148
	$Re = 2.19 \cdot 10^5$	8.99	8.46	9.99	9.85	1.00	1.39	0.017	0.040

### Wake width

Finally, the streamwise distribution of the wake half-width is shown in figures 5.36 and 5.37 for angles of attack  $0^\circ$  and  $7^\circ$ , respectively. At this point it should be stated that an error is present in the results for the plasma on situation at  $7^\circ$ . For actuators C and D the graphs should be terminated after  $x/c=1.14$  and  $1.12$ , respectively. The error occurs when the wake moves too far out of the FOV in the PIV data, such that the wake half-width can not be determined anymore.

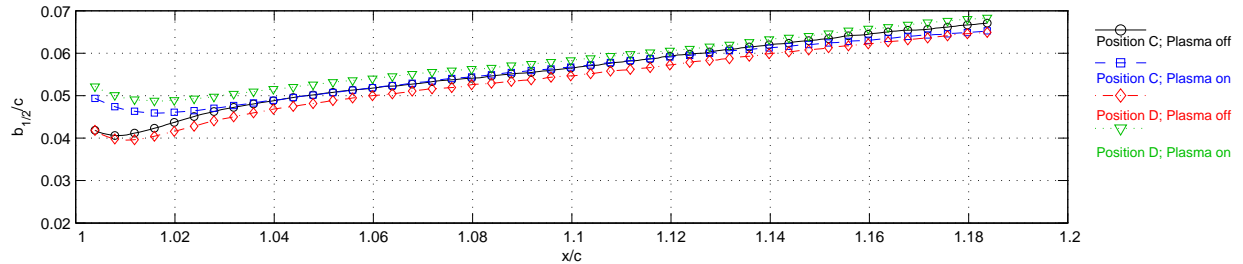


**Figure 5.36:** Streamwise distribution of the wake half-width as produced by plasma actuators C and D (on and off) at an angle of attack of  $0^\circ$  and Reynolds number  $1.46 \cdot 10^5$ .

The wake half-width is defined as the thickness of the wake (in  $y$ -direction) at the point where the velocity deficit is half of the maximum value. In a formula it is defined as:

$$\frac{b_{1/2}}{c} = \frac{y}{c} \Big|_{\left[ \frac{u_{min}}{U_\infty} + \frac{1 - \frac{u_{min}}{U_\infty}}{2} \right]_{top}} - \frac{y}{c} \Big|_{\left[ \frac{u_{min}}{U_\infty} + \frac{1 - \frac{u_{min}}{U_\infty}}{2} \right]_{bottom}} \quad (5.15)$$

Take for example the wake data of actuator C without plasma on the far left in figure 5.32, at  $x/c=1.03$ . The maximum value of the velocity deficit,  $u_{min}/U_\infty$ , is about  $-0.1$ . The point where

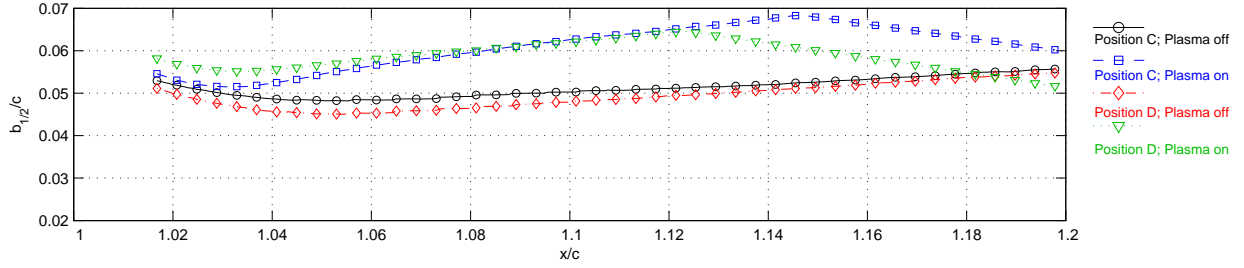


**Figure 5.37:** Streamwise distribution of the wake half-width as produced by plasma actuators C and D (on and off) at an angle of attack of  $7^\circ$  and Reynolds number  $1.46 \cdot 10^5$ .

the velocity deficit is half of the maximum value then becomes 0.55, the average of -0.1 and 1. Filling this in in equation 5.15 results in:

$$\frac{b_{1/2}}{c} \approx \frac{y}{c} @ [0.55]_{top} - \frac{y}{c} @ [0.55]_{bottom} \approx 0.02 - (-0.027) \approx 0.047 \quad (5.16)$$

This value is plotted in figure 5.36 at  $x/c=1.03$ . This process is repeated at different stations in streamwise direction and the final result is the distribution as shown in figure 5.36. For the plasma on cases the wake half-widths found are consistently larger as compared to the plasma off situation. This is true for both angles of attack. It agrees with the increase in boundary layer thickness on the pressure side of the airfoil, as is found from the Reynolds shear stress distributions.

## 5.4 Power consumption

During the course of this thesis also an investigation on the power consumption of the plasma actuator is performed. This is done with the use of the integrating capacitor method, as described in detail in section 3.3. During this study the power consumption was calculated for selected ranges of the actuation frequency,  $f_{ac}$ , and the applied peak-to-peak voltage,  $V_{app}$ . The experimental parameters used are given in table 4.1. After smoothing of the raw voltage data by the Savitzky-Golay algorithm, signals of the measured voltage over the capacitor and the applied voltage over the electrodes of the plasma actuator are plotted on the left hand side of in figure 5.38, for a couple combinations of  $f_{ac}$  and  $V_{app}$ . The corresponding Lissajous curves and the calculated power consumption are plotted on the right hand side of figure 5.38.

Figures 5.38a-b and 5.38c-d show the results for the highest tested values of  $f_{ac}$  and  $V_{app}$ , respectively. The data in figures 5.38a-b represent the data for the tested actuator setting used in this report. The corresponding power consumption per meter effective electrode length is found to be 35.8W/m. With an approximate electrode span of 0.4m, as used in this thesis work, the power consumption is found to be 14.3W. Figures 5.38e-h show the power consumption data at the same actuators settings twice (at different time instances). From the associated values of the of the power consumption it can be stated that the integrated capacitor method is reasonably precise. The variation of the measure power consumption against the actuation frequency,  $f_{ac}$ , and the applied peak-to-peak voltage,  $V_{app}$ , is shown in figure 5.39.

The functional relations between the power consumption and actuation frequency or applied peak-to-peak voltage correspond well with the relations found in literature[17, 16, 41]. A linear relation is found for the actuation frequency and a power law for the applied peak-to-peak voltage.

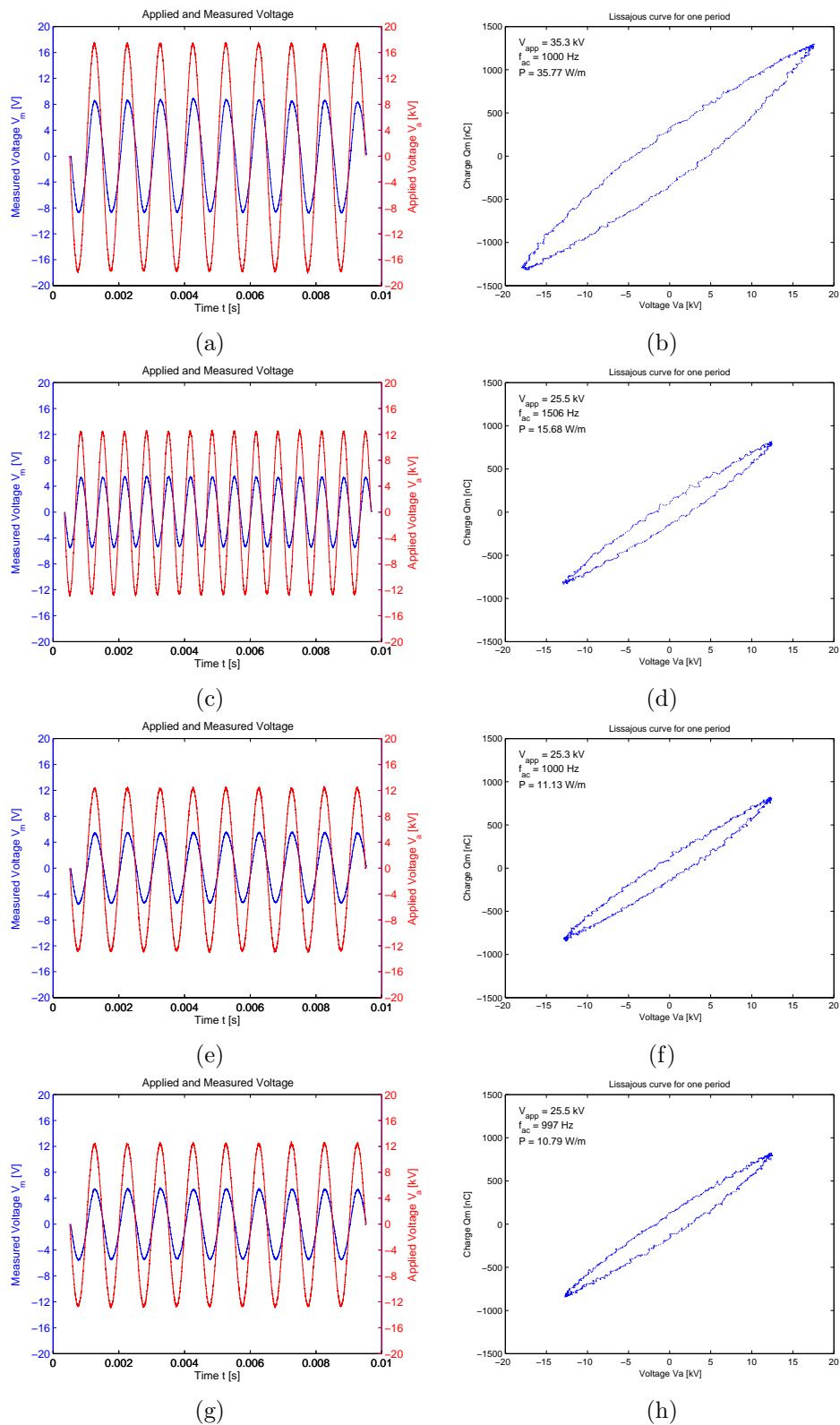


**Figure 5.38:** Figures with signals of the measured voltage over the capacitor and the applied voltage over the electrodes of the plasma actuator and the corresponding Lissajous curves and the calculated power consumption for: a-b)  $f_{ac}=1000$ Hz and  $V_{app}=35$ kV, c-d)  $f_{ac}=1500$ Hz and  $V_{app}=25$ kV, e-f)  $f_{ac}=1000$ Hz and  $V_{app}=25$ kV, g-h)  $f_{ac}=1000$ Hz and  $V_{app}=25$ kV, .

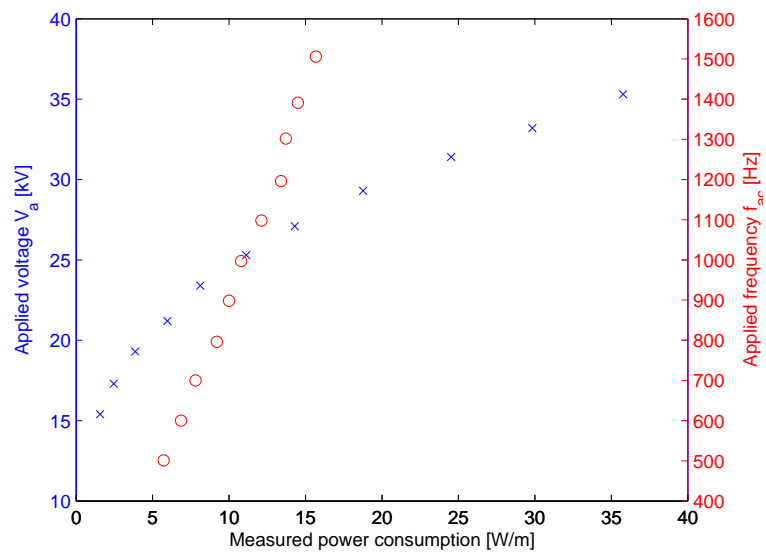


**Figure 5.39:** Measured power consumption against actuation frequency,  $f_{ac}$ , and the applied peak-to-peak voltage,  $V_{app}$ .



# Conclusions and recommendations

The work in the present thesis has been conducted in order to discover the capabilities of the DBD plasma actuator in the field of active load control. Experimental methods have been employed to investigate the ability of the plasma actuator to change the Kutta condition on a rounded trailing edge airfoil, as stated in chapter 1. This final chapter aims at presenting a summary of the major conclusions found from the performed investigations. Additionally, based on these conclusions, an attempt is made to give recommendations for future research in the area of circulation control with DBD plasma actuators.

## 6.1 Conclusions

During the experimental investigations a modified version of a NACA64-2-A015 airfoil with a rounded trailing edge was used. A force balance was designed to measure the aerodynamic forces. Several plasma actuator configurations were tested on their effectiveness in controlling the Kutta condition on the rounded trailing edge. The parameter that was changed between the configurations was the location of the gap between the electrodes, in the current case corresponding to the edge of the exposed electrode facing the covered electrode. From the force measurements it followed that the effectiveness of the plasma actuator depends on several factors. Firstly, the angle of attack  $\alpha$  of the airfoil had a strong influence on the achieved change in lift coefficient  $\Delta c_l$ . For all configurations the plasma actuator generated a higher  $\Delta c_l$  at angles of attack close to stall. No explanation for this behaviour could be found from the force measurements. Secondly, at higher  $\alpha$  the plasma actuators positioned on the lower side of the airfoil (pressure side) became more effective and changes up to  $\Delta c_l=0.15$  were measured for an  $\alpha=8^\circ$ , corresponding to a 21% increase in  $c_l$ . This was measured at a chord Reynolds number of around  $1.5 \cdot 10^5$ . Finally, for larger Reynolds numbers the actuators on the pressure side of the airfoil stayed more effective, however the overall effectiveness was greatly reduced. The maximum  $\Delta c_l$  is reduced to 0.075 at  $Re=2.1 \cdot 10^5$  and 0.04 at  $Re=2.9 \cdot 10^5$ . This effect is contributed to the constant momentum input by the plasma actuator. For higher Reynolds number the relative momentum input decreases with respect to the free stream momentum, resulting in a smaller efficiency.

The best plasma actuator configuration was compared with a series of Gurney flaps mounted on the rounded trailing edge airfoil. The measured lift coefficient data at  $Re=1.5 \cdot 10^5$  suggests that at

high pre-stall angles of attack the plasma actuator can be compared to a Gurney flap with an effective height of  $h/c=0.018$ . However, at higher Reynolds numbers the effectiveness of the plasma actuators is reduced while the Gurney flaps become even more effective. This can be attributed to the geometric nature of the flow control in case of the Gurney flaps. At higher Reynolds numbers the boundary layer becomes thinner, making the flow more sensitive to changes in airfoil shape.

The effectiveness of the plasma actuator is calculated using a method commonly used in classical circulation control applications with slot blowing. The efficiency is in this case expressed through the lift augmentation coefficient, defined by the ratio of the increase in lift coefficient and the blowing momentum coefficient. The blowing momentum coefficient being the relative momentum input by the plasma actuator with respect to the free stream flow momentum. The momentum input is calculated from a momentum balance over a control volume in the PIV velocity data in quiescent flow conditions. The maximum lift augmentation coefficient corresponding to a maximum  $\Delta c_l$  was on average 110, for angles of attack close to stall and regardless of the Reynolds number. This means that the lift augmentations achieved at some conditions is as high as 110 times the relative momentum input by the actuator itself. However, the absolute increase in lift coefficient obtained is very low and potentially can be used for active load control only after careful upscaling.

The investigation on the effectiveness of the plasma actuators in changing the Kutta condition continued with a time-resolved PIV study. The goal of this experiment was to gain insight in the flow phenomena occurring right behind the rounded trailing edge. The trends regarding the effects of actuator positioning and angle of attack, as seen during both experimental campaigns, suggest that several mechanisms are influencing the airfoil circulation control. Firstly, the positioning of the plasma actuator with respect to the commonly occurring recirculation region behind the blunt trailing edge is of importance. From the PIV mean velocity field data it was found that the plasma actuator seems to interact with the counter rotating vortex pair in the recirculation area. When the plasma actuator is positioned close to the rear stagnation point the forcing of the actuator disrupts the vortex pair and seems to redirect some of the momentum stored in the vortex system. Secondly, at high positive angles of attack the best performing (tested) positions D and E are located on the pressure side of the airfoil where the boundary layer is considerably thinner than on the suction side. This effectively places the actuator closer to an area of high momentum. In combination with the velocity jet produced by the plasma actuators, which are directed more upstream in case of position D and E, it seems that it produces an higher influence on the high momentum flow. In other words, the velocity jet of the plasma actuator can 'penetrate' the boundary layer further. The higher effectiveness is explained by the smaller distance between the actuator location and the high momentum flow, resulting in a lower diffusion of the induced velocity jet, as compared to actuator position C.

Through careful observation of the results an important conclusion can be stated for the general lift enhancement using plasma actuators. Firstly, it can be assumed that the momentum input due to the plasma actuation is independent of the positioning of the plasma actuator on the rounded trailing edge. This is a valid assumption since the geometric and electrical parameters stay constant. Taking this into account it can be safely concluded that the lift enhancement is indeed due to manipulation of the Kutta condition. If the plasma actuator's effect was a simple increase in circulation due to the induced momentum input (independent of the plasma actuator positioning) then the lift enhancement would be constant for any given position of the actuator and angle of attack. A simple calculation showed that for free stream velocities of 10, 15 and 20m/s the changes in lift coefficient are 0.0104, 0.0069 and 0.0052, respectively. With respect to the average values found for the change in lift coefficient the added circulation due to the local induced momentum input accounts for only 10.4%, 18.3% and 21.5% of the total increase in  $\Delta c_l$ . This supports the statement made earlier that the lift enhancement is due to manipulation of the Kutta condition on the rounded trailing edge. At the same time it also shows that the decrease in

effectiveness of the plasma actuator for increasing Reynolds number is mostly due to the constant momentum input of the plasma actuator, independent of flow conditions.

In addition to the field data also the wake of the airfoil was analysed. The wake deflection is in this case a good metric in determining the effectiveness of the plasma actuation. Results show that the change in wake deflection  $\Delta\theta_w$  and the change in measured lift coefficient  $\Delta c_l$  from the force measurements are closely related. The largest change in wake deflection found was  $6^\circ$  for a Reynolds number of  $1.46 \cdot 10^5$  at an angle of attack of  $7^\circ$ , this corresponded well to the largest change in lift coefficient found, 0.148 at the same flow conditions. This supports the statement that the plasma actuator is changing the Kutta condition on the rounded trailing edge since the wake deflection is commonly used as a measure for the change in the Kutta condition, the stagnation point is moved down to the pressure side of the airfoil. Due to this the total circulation on the airfoil is increased and since the circulation is related to the lift coefficient it can be said that the lift generated by the airfoil is increased.

Finally, the power consumption of the plasma actuator was calculated using the so called integrated capacitor method. The power consumption for the actuation settings used in the largest part of this thesis work, at an actuation frequency of 1000Hz and applied peak to peak voltage of 35kV, resulted in a power consumption of 35.8W/m. With an approximate electrode span of 0.4m, as used in this thesis work, the power consumption is found to be 14.3W. By testing the power consumption twice at the same settings indicated that the integrated capacitor method is reasonably precise.

## 6.2 Recommendations

The current research was intended to provide an overview of the capabilities of the plasma actuator to actively control the load generated by the rounded trailing edge airfoil through manipulation of the Kutta condition. The recommendations given in this section are provided for future research on this concept.

With the possible application for unsteady load control, it is important to focus on the upscaling of the plasma actuator. In this thesis work it was found that the Reynolds number has a strong influence on the performance of the plasma actuator, mainly due to the constant momentum input (independent of the external flow conditions). Future research should be towards the development of actuators which are capable to produce stronger wall jets. This way the plasma actuator will have more control over the Kutta condition and therefore more control over the lift generated by the airfoil.

Furthermore, the effect of the actuator position with respect to the rear stagnation point is something that should be investigated into more detail. From the obtained results it seems that the plasma actuators are most effective when the forcing on the flow occurs close to or at the stagnation point. It was also found that the effectiveness of the plasma actuators is strongly depending on the angle of attack. It is recommended to study this observation into more detail. While doing this, it is advised to increase the trailing edge radius. The relatively small radius used in this report makes it hard to position the plasma actuator electrodes exactly the way that is required. Besides this, the larger radius will create a larger recirculation area in the wake such that the found interaction of the plasma actuator with the vortex structures can be expanded and studied in more detail.

For active load control application it is important that the change in lift can be controlled by the plasma actuator. Meaning that the relation between the electrical settings of the plasma actuator

and the achieved lift coefficient should be investigated. An idea to achieve both positive and negative changes in lift is the implementation of spanwise distribution of discontinuous plasma actuator electrodes with altering forcing directions.

---

# References

- [1] J.D. Anderson. *Fundamentals of aerodynamics*. Edition. McGraw-Hill, 2005.
- [2] G. Artana, J. D'Adamo, L. Léger, E. Moreau, and G. Touchard. Flow control with electrohydrodynamic actuators. In *39th Aerospace Sciences Meeting and Exhibit*, Reno, Nevada, January 2001.
- [3] D.E. Ashpis and M.C. Laun. Progress toward accurate measurements of power consumptions of DBD plasma actuators. In *50th AIAA Aerospace Sciences Meeting*, Nashville, Tennessee, January 2012.
- [4] N. Benard and E. Moreau. Role of the electric waveform supplying a dielectric barrier discharge plasma actuator. *Applied Physics Letters*, 100(193503):1 – 5, 2012.
- [5] M. Blaylock, R. Chow, and C.P. van Dam. Comparison of microjets with microtabs for active aerodynamic load control. In *5th Flow Control Conference*, Chicago, Illinois, June-July 2010.
- [6] C.S. Boeijs, H. de Vries, I. Cleine, E. van Emden, G.G.M. Zwart, H. Stobbe, A. Hirschberg, and H.W.M. Hoeijmakers. Fluidic load control for wind turbine blades. In *47th AIAA Aerospace Sciences Meeting Including The New Horizons Forum and Aerospace Exposition*, Orlando, Florida, January 2009.
- [7] J.P. Boeuf, Y. Lagmich, T. Callegari, and L.C. Pitchford. EHD force in dielectric barrier discharges parametric study and influence of negative ions. In *45th AIAA Aerospace Sciences Meeting and Exhibit*, Reno, Nevada, January 2007.
- [8] V. Boucinha, R. Jousot, P. Magnier, R. Weber, and A. Leroy-Chesnau. Characterization of the ionic wind produced by a DBD actuator designed to control laminar-to-turbulent transition. In *14th International Symposium on Applications of Laser Techniques to Fluid Mechanics*, Lisbon, Portugal, July 2008.
- [9] T.F. Brooks and M.A. Marcolini. Airfoil trailing edge flow measurements and comparison with theory incorporating open wind tunnel corrections. In *AIAA/NASA 9th Aeroacoustics Conference*, Williamsburg, Virginia, October 1984.
- [10] P. Chui. CIEG 434: Air pollution control. <http://ce.ude1.edu/~dentel/434.html>, Spring 2007.
- [11] T.C. Corke, C.L. Enloe, and S.P. Wilkinson. Dielectric barrier discharge plasma actuators for flow control. *Annual Review of Fluid Mechanics*, 42: 505 – 529, 2010.

- [12] T.C. Corke, C. He, and M.P. Patel. Plasma flaps and slats: an application of weakly-ionized plasma actuators. In *2nd Flow Control Conference*, Portland, Oregon, June-July 2004.
- [13] T.C. Corke, M.L. Post, and D.M. Orlov. Single dielectric barrier discharge plasma enhanced aerodynamics: physics, modeling and applications. *Experiments in Fluids*, 46(1): 1 – 26, 2009.
- [14] R.J. Englar. Circulation control pneumatic aerodynamics: blown force and moment augmentation and modification; past, present & future. In *Fluids Conference and Exhibition*, Denver, Colorado, June 2000.
- [15] C.L. Enloe, M.G. McHarg, and T.E. McLaughlin. Time-correlated force production measurements of the dielectric barrier discharge plasma aerodynamic actuator. *Journal of Applied Physics*, 103(073302):1 – 7, 2008.
- [16] C.L. Enloe, T.E. McLaughlin, R.D. VanDyken, K.D. Kachner, E.J. Jumper, and T.C. Corke. Mechanisms and responses of a single dielectric barrier plasma actuator: plasma morphology. *AIAA Journal*, 42(3):589 – 594, 2004.
- [17] C.L. Enloe, T.E. McLaughlin, R.D. VanDyken, K.D. Kachner, E.J. Jumper, T.C. Corke, M. Post, and O. Haddad. Mechanisms and responses of a single dielectric barrier plasma actuator: geometric effects. *AIAA Journal*, 42(3):595 – 604, 2004.
- [18] L.H. Feng, T.N. Jukes, K.S. Choi, and J.J. Wang. Flow control over a NACA 0012 airfoil using dielectric-barrier-discharge plasma actuator with a Gurney flap. *Experiments in Fluids*, 52(6):1533 – 1546, 2012.
- [19] G.I. Font, C.L. Enloe, and T.E. McLaughlin. Plasma volumetric effects on the force production of a plasma actuator. *AIAA Journal*, 48(9):1869 – 1874, 2010.
- [20] M. Forte, J. Jolibois, E. Moreau, G. Touchard, and M. Cazalens. Optimization of a dielectric barrier discharge actuator by stationary and non-stationary measurements of the induced flow velocity: application to airflow control. *Experiments in Fluids*, 43(6):917 – 928, 2007.
- [21] S. Grundmann and C. Tropea. Experimental transition delay using glow-discharge plasma actuators. *Experiments in Fluids*, 42(4):653 – 657, 2007.
- [22] S. Grundmann and C. Tropea. Experimental damping of boundary-layer oscillations using DBD plasma actuators. *International Journal of Heat and Fluid Flow*, 30(3):394 – 402, 2009.
- [23] C. He. *Plasma slats and flaps: an application of plasma actuators for hingeless aerodynamic control*. Ph.D. Thesis, University of Notre Dame, Notre Dame, Indiana, 2008.
- [24] A.R. Hoskinson, N. Hershkowitz, and D.E. Ashpis. Force measurements of single and double barrier DBD plasma actuators in quiescent air. *Journal of Physics D: Applied Physics*, 41(24):1 – 11, 2008.
- [25] M. Jahanmiri. Particle image velocimetry: fundamentals and its applications. Technical Report Report 2011:03, ISSN 1652-8549, Div. of Fluid Dynamics, Dep. of Applied Mechanics, Chalmers University of Technology, March 2011.
- [26] B. Jayaraman and W. Shyy. Modeling of dielectric barrier discharge-induced fluid dynamics and heat transfer. *Progress in Aerospace Sciences*, 44(3):139 – 191, 2008.
- [27] J. Johnson, C.P. van Dam, and D.E. Berg. Active load control techniques for wind turbines. Sandia Report No. SAND2008-4809, Sandia National Laboratories, August 2008.
- [28] J. Jolibois, M. Forte, and E. Moreau. Application of an AC barrier discharge actuator to control airflow separation above a NACA 0015 airfoil: Optimization of the actuator location along the chord. *Journal of Electrostatics*, 66(9):496 – 503, 2008.

- [29] J.Pons, E. Moreau, and G. Touchard. Asymmetric surface dielectric barrier discharge in air at atmospheric pressure: electrical properties and induced airflow characteristics. *Journal of Physics D: Applied Physics*, 38(19):3635 – 3642, 2005.
- [30] T. Jukes and K.S. Choi. Active control of a cylinder wake using surface plasma. In *IUTAM Symposium on Unsteady Separated Flows and their Control*, pages 539 – 550. Springer Science, Corfu, Greece, June 2009.
- [31] T.N. Jukes and K.S. Choi. Dielectric-barrier-discharge vortex generators: characterisation and optimisation for flow separation control. *Experiments in Fluids*, 52(2):329 – 345, 2012.
- [32] W. Kim, H. Do, M.G. Mungal, and M.A. Cappalli. On the role of oxygen in dielectric barrier discharge actuation of aerodynamic flows. *Applied Physics Letters*, 91(181501):1 – 3, 2007.
- [33] U. Kogelschatz, B. Eliasson, and W. Egli. Dielectric-barrier discharges. Principle and applications. *Journal de Physique IV*, 7(C4):47 – 66, 1997.
- [34] S. Kota, J. Hetrick, R. Osborn, D. Paul, E. Pendleton, P. Flick, and C. Carlman. Design and application of compliant mechanisms for morphing aircraft structures. In *Proceedings of SPIE Vol 5054 - Smart Structures and Materials: Industrial and Commercial Applications of Smart Structures Technologies*, pages 24–33, San Diego, California, March 2003.
- [35] M. Kotsonis. *Dielectric barrier discharge actuators for flow control: diagnostics, modeling, application*. Ph.D. Thesis, Delft University of Technology, Delft, Netherlands, 2012.
- [36] M. Kotsonis and S. Ghaemi. Performance improvement of plasma actuators using asymmetric high voltage waveforms. *Journal of Physics D: Applied Physics*, 45(4):1 – 12, 2012.
- [37] I. Langmuir. Oscillations in ionized gases. *Proceedings of the National Academy of Sciences*, 14(8):627 – 637, 1928.
- [38] P. Magnier, V. Boucinha, B. Dong, R. Weber, A. Leroy-Chesnau, and D. Hong. Experimental study of the flow induced by a sinusoidal dielectric barrier discharge actuator and its effects on a flat plate natural boundary layer. *Journal of Fluids Engineering*, 131(011203):1 – 11, 2009.
- [39] T.E. McLaughlin, B. Felker, J.C. Avery, and C.L. Enloe. Further experiments in cylinder wake modification with dielectric barrier discharge forcing. In *44th AIAA Aerospace Sciences Meeting and Exhibit*, Reno, Nevada, January 2006.
- [40] A. Melling. Tracer particles and seeding for particle image velocimetry. *Measurement Science Technology*, 8(12):1406 – 1416, 1997.
- [41] E. Moreau. Airflow control by non-thermal plasma actuators. *Journal of Physics D: Applied Physics*, 40(3): 605 – 636, 2007.
- [42] D.T. Nakafuji, C.P. van Dam, R.L. Smith, and S.D. Collins. Active load control airfoils using microtabs: technical papers. *Journal of Solar Energy Engineering*, 123(4):282 – 289, 2001.
- [43] V. Nehra, A. Kumar, and H.K. Dwivedi. Atmospheric non-thermal plasma sources. *International Journal of Engineering*, 2(1):53 – 68, 2008.
- [44] D.F. Opaits, D.V. Roupasov, S.M. Starikovskaia, A.Y. Starikovskii, I.N. Zavyalov, and S.G. Saddoughi. Plasma control of boundary layer using low-temperature non-equilibrium plasma of gas discharge. In *43th AIAA Aerospace Sciences Meeting and Exhibit*, Reno, Nevada, January 2005.
- [45] D.M. Orlov. *Modelling and simulation of single dielectric barrier discharge plasma actuators*. Ph.D. Thesis, University of Notre Dame, Notre Dame, Indiana, 2006.

- [46] D.M. Orlov, T.C. Corke, and M.P. Patel. Electric circuit model for aerodynamic plasma actuator. In *44th AIAA Aerospace Sciences Meeting and Exhibit*, Reno, Nevada, January 2006.
- [47] M.L. Post and T.C. Corke. Separation control on high angle of attack airfoil using plasma actuators. *AIAA Journal*, 42(11):2177 – 2184, 2004.
- [48] M. Raffel, C.E. Willert, S.T. Wereley, and J. Kompenhans. *Particle image velocimetry - a practical guide*. 2nd edition. Springer, Berlin, 2007.
- [49] M. Robinson. Movement of air in the electric wind of the corona discharge. *American Institute of Electrical Engineers, Part I: Communication and Electronics, Transactions of the*, 80(2):143 – 150, 1961.
- [50] J.R. Roth. Aerodynamic flow acceleration using para-electric and peristaltic electrohydrodynamic effects of an one atmosphere uniform glow discharge plasma. *Physics of Plasmas*, 10(5):2117 – 2126, 2003.
- [51] J.R. Roth and X. Dai. Optimization of the aerodynamic plasma actuator as an electrohydrodynamic (EHD) electrical device. In *44th AIAA Aerospace Sciences Meeting and Exhibit*, Reno, Nevada, January 2006.
- [52] D.V. Roupasov, I.N. Zavyalov, and A.Y. Starikovskii. Boundary layer separation plasma control using low-temperature non-equilibrium plasma of gas discharge. In *44th AIAA Aerospace Sciences Meeting and Exhibit*, Reno, Nevada, January 2006.
- [53] A. Savitzky and M.J.E. Golay. Smoothing and differentiation of data by simplified least squares procedures. *Analytical Chemistry*, 36(8):1627 – 1639, 1964.
- [54] F. Scarano. *Experimental Methods*. Notes, Delft University of Technology, Delft, Netherlands, 2006.
- [55] F. Scarano and M.L. Riethmuller. Iterative multigrid approach in PIV image processing with discrete window offset. *Experiments in Fluids*, 26(6):513 – 523, 1999.
- [56] D.M. Schatzmann and F.O. Thomas. Turbulent boundary-layer separation control with single dielectric barrier discharge plasma actuators. *AIAA Journal*, 48(8):1620 – 1634, 2010.
- [57] A. Séraudie, E. Aubert, N. Naudé, and J.P. Cambonne. Effect of plasma actuators on a flat plate laminar boundary layer in subsonic conditions. In *3rd Flow Control Conference*, San Francisco, California, June 2006.
- [58] E. Stephen, A. Campbell, J. Nygard, M. Selby, C. Hennig, and T. McLaughlin. Assessment of a corner plasma actuator for flow control using periodic jets. In *29th Applied Aerodynamics Conference*, Honolulu, Hawaii, June 2011.
- [59] F.O. Thomas, T.C. Corke, M. Iqbal, A. Kozlov, and D. Schatzman. Optimization of dielectric barrier discharge plasma actuators for active aerodynamic flow control. *AIAA Journal*, 47(9):2169 – 2178, 2009.
- [60] F.O. Thomas, A. Kozlov, and T.C. Corke. Plasma actuators for bluff body flow control. In *3rd Flow Control Conference*, San Francisco, California, June 2006.
- [61] C. Tongchitpakdee, S. Benjanirat, and L.N. Sankar. Numerical studies of the effects of active and passive circulation enhancement concepts on wind turbine performance. *Journal of Solar Energy Engineering*, 128(4):432 – 444, 2006.
- [62] R. VanDyken, T.E. McLaughlin, and C.L. Enloe. Parametric investigations of a single dielectric barrier plasma actuator. In *42th AIAA Aerospace Sciences Meeting and Exhibit*, Reno, Nevada, January 2004.

- [63] J. Westerweel. Fundamentals of digital particle image velocimetry. *Measurement Science Technology*, 8(12):1379 – 1392, 1997.
- [64] R.M. Wood. A discussion of aerodynamic control effectors (ACEs) for unmanned aerial vehicles (UAVs). In *AIAA's 1st Technical Conference and Workshop on Unmanned Aerospace Vehicles*, Portsmouth, Virginia, May 2002.
- [65] I.N. Zavyalov, D.F. Opaitis, D.V. Roupasov, A.Y. Starikovskii, and S.G. Saddoughi. Boundary layer control for NACA-0015 airfoil in subsonic regime. In *15th International Conference on MHD (ICMHD) Electrical Power Generation*, Moscow, Russia, May 2005.
- [66] P.F. Zhang, B. Yan, A.B. Liu, and J.J. Wang. Numerical simulation on plasma circulation control airfoil. *AIAA Journal*, 48(10):2213 – 2226, 2010.
- [67] J. Zito, R. Durscher, J. Soni, S. Roy, and D. P. Arnold. Flow and force inducement using micron size dielectric barrier discharge actuators. *Applied Physics Letters*, 100(193502):1 – 4, 2012.



---

# Appendix A

---

## Electric field study

Section 3.2.2 described a model for the tracer particle motion in a fluid. The presence of the plasma region near the electrode edges introduces a additional term to the used Hinze model. In this appendix the method used for the determination of the electric field is presented. From the local electric field strength the electrostatic force on the tracer particles can be estimated. The electric field is obtained by solving the electrostatic Poisson equation for the potential  $\phi$ :

$$-\nabla(\epsilon\nabla\phi) = \rho \tag{A.1}$$

where  $\epsilon$  is the coefficient of dielectricity and  $\rho$  is the space charge density. Setting  $\rho$  to zero allows for a approximation of the electric field, by solving the resulting Laplace's equation. The problem definition, design and boundary conditions are set as indicated in figure A.1.

The problem is solved with the MATLAB Partial Differential Equation Toolbox (function `pdetool`), by defining the different domains (dielectric and air) based on the plasma actuator geometry (position C), the coefficients in the partial differential equation and applying the boundary conditions. For the electrodes a Dirichlet boundary condition is set and the outer boundaries of the domains are covered by Neumann boundary conditions. The electric potential of the exposed electrode is set to the maximum voltage amplitude used during the experiments, i.e.  $17.5kV$ . Note that this is the maximum value occurring during one actuation cycle and not an average value. The covered electrode is grounded. The resulting electric potential and electric field are shown in figures A.2 and A.3.

Contour lines are plotted for the electric potential varying from 0.5 to 17.5kV in steps of 0.5kV. For the electric field strength contour lines are plotted varying from  $5\cdot 10^5$  to  $2\cdot 10^7V/m$  in steps of  $5\cdot 10^5V/m$ . The strongest electric fields are found on the electrode edges facing each other, where the distance between the electrodes reaches a minimum. The electric field strength decays quickly when moving away from these edges. According to the method presented by Artana et al.[2] the electrostatic forces can be neglected for electric fields below approximately  $1\cdot 10^6V/m$  for particles diameters of  $1\mu m$ , see also section 3.2.2 for more details. The second contour line from the right in figure A.3 corresponds to this value. This indicates that within the region 2.5mm to the right and 5mm below the exposed electrode edge this limit is achieved.

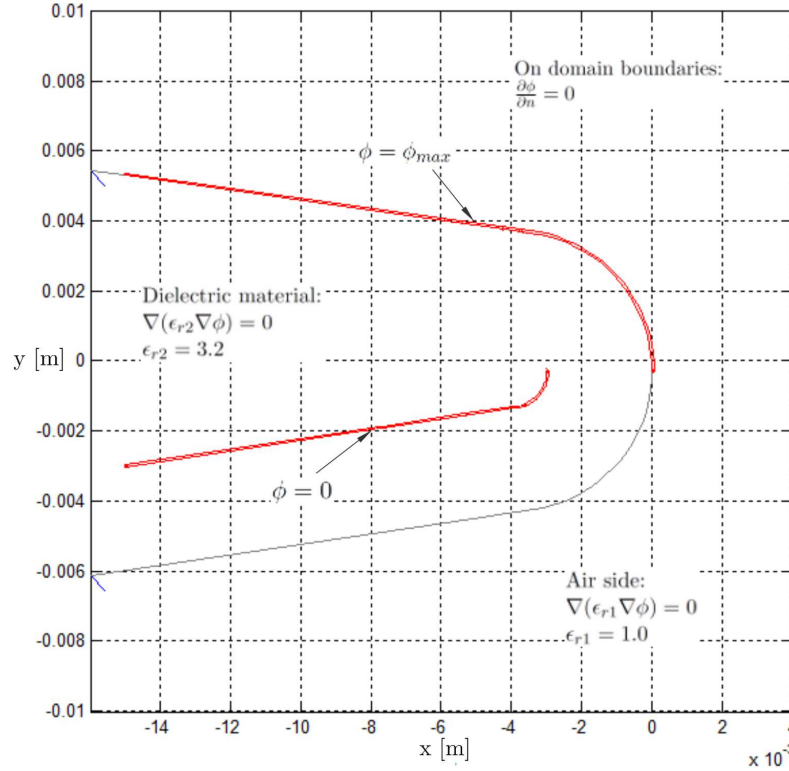


**Figure A.1:** Plasma actuator configuration, domain and boundary conditions for determination of the electric field.

Between 1-2.5mm in x-direction and 2-5mm in y-direction, measured from the exposed electrode edge, the electric field strength lies between  $1 \cdot 10^6 \text{V/m}$  and  $2 \cdot 10^6 \text{V/m}$ , which according to equation 3.8 results in a ratio between the viscous and electrostatic force equal to the slipping velocity. For typical plasma actuator induced velocities of several m/s this means that the viscous force is only several times ( $O(1)$ ) larger than the electrostatic force on the traces particles.

From the method introduced by Artana et al. it can be concluded that close to the rounded trailing edge, in a region of 1 by 2mm, the particle motion is dominated by the electrostatic force. Outside of this region the electrostatic force is quickly decaying and the viscous drag force becomes several times larger. It should also be addressed that the used potential of the exposed electrode is the maximum potential used in all experiments. This value is only reached twice during a single cycle. Used a lower (average) potential will result in a considerably higher ratio between the viscous drag force and the electrostatic force.

For the current research where the flow development around the rounded trailing edge is of interest it is clear that care should be taken when interpreting the results. The PIV results obtained in the immediate vicinity of the trailing edge can be influenced by the effect of the electrostatic force on the tracer particles, caused by the strong electric field around the exposed electrode edge. Moving a few millimetre away from this region the strength of the electric field is quickly decaying and the viscous drag force starts to dominate the particle motion.

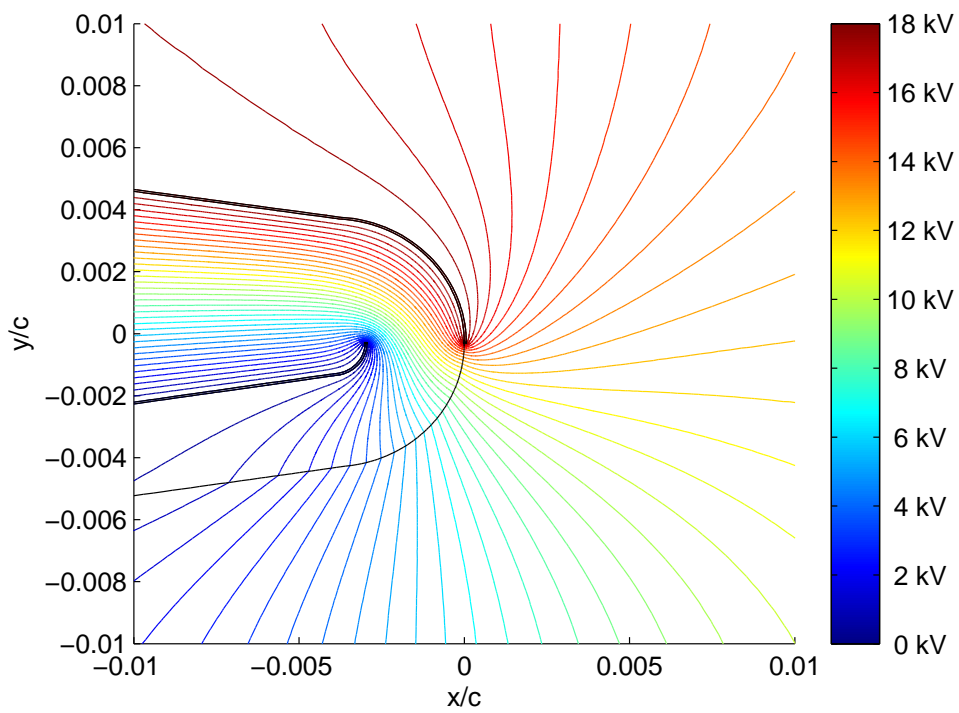


**Figure A.2:** Electric potential distribution of the plasma actuator with gap at position C for maximum applied peak-to-peak voltage of 35kV. Contour lines show constant electric potential lines.

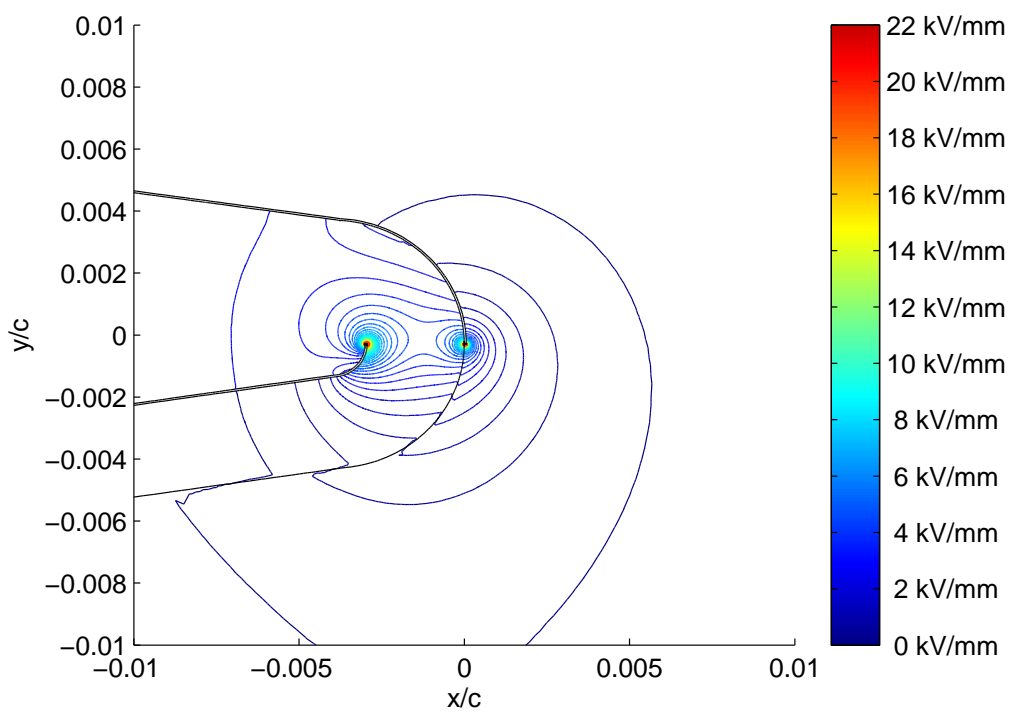


**Figure A.3:** Electric field strength of the plasma actuator with gap at position C for the maximum applied peak-to-peak voltage of 35kV. Contour lines show electric field strength varying from  $5 \cdot 10^5$  to  $2 \cdot 10^7$  V/m in steps of  $5 \cdot 10^5$  V/m

---

## Appendix B

---

### PIV data: more results

During the second experimental campaign particle image velocimetry was applied in order to characterize the flow field around the trailing edge. Selected actuator configurations, angles of attack and Reynolds numbers were tested as indicated in table 4.7. By the use of Davis 8.1.3 (Lavisio GmbH) the mean velocity field, mean turbulent kinetic energy and mean Reynolds shear stress are calculated. This appendix shows the PIV field data for a Reynolds number of  $2.19 \cdot 10^5$ . See section 4.5 for more information on the experimental set-up, selected actuator configurations and parameters used in this experiment. For a more elaborated discussion on the PIV field data one is referred to section 5.3, where the data for Reynolds number of  $1.46 \cdot 10^5$  is analysed.

#### Mean velocity field

The flow fields around the rounded trailing edge were also obtained at a higher Reynolds number. For Reynolds number of  $2.19 \cdot 10^5$  the mean velocity fields are plotted in figures B.1 and B.2, for  $0^\circ$  and  $7^\circ$ .

#### Turbulent kinetic energy

Additionally to the mean velocity fields also the mean turbulent kinetic energy distributions in the wake are calculated. The resulting distributions are shown in figures B.3 and B.4 for angles of attack of  $0^\circ$  and  $7^\circ$ , respectively.

#### Reynolds stress

Finally, the mean Reynolds shear stress distributions in the wake of the rounded trailing edge model are shown in figures B.5 and B.6 for angles of attack of  $0^\circ$  and  $7^\circ$ , respectively.

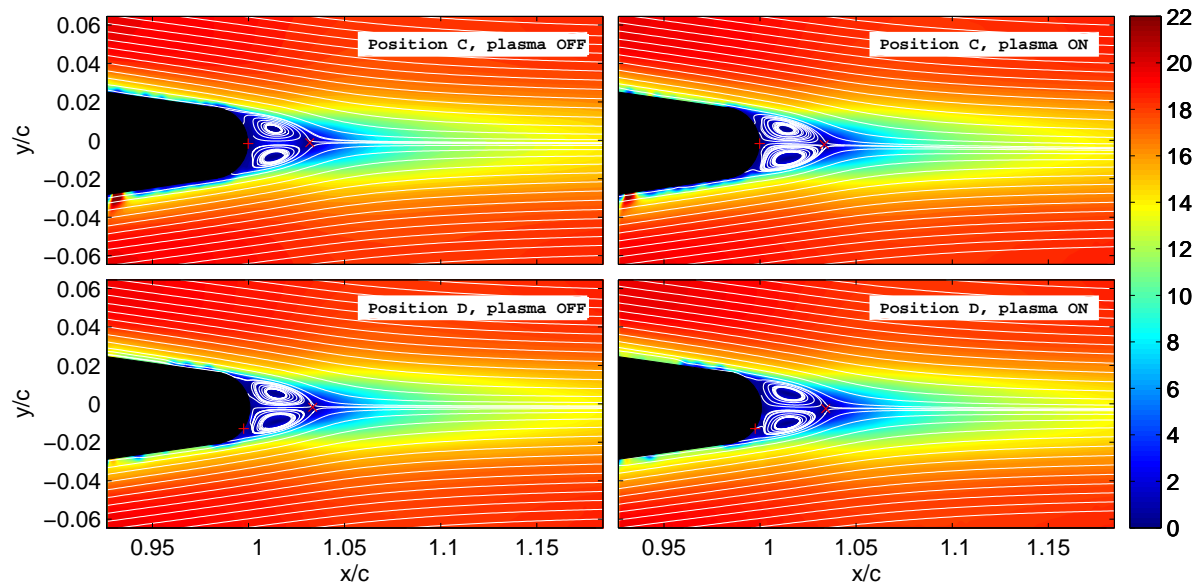


**Figure B.1:** Mean velocity fields produced by plasma actuators C and D (on and off) at an angle of attack of  $0^\circ$  and Reynolds number  $2.19 \cdot 10^5$ . The + indicates the actuator gap position, the x indicates the location of the saddle point. The velocity is in m/s.

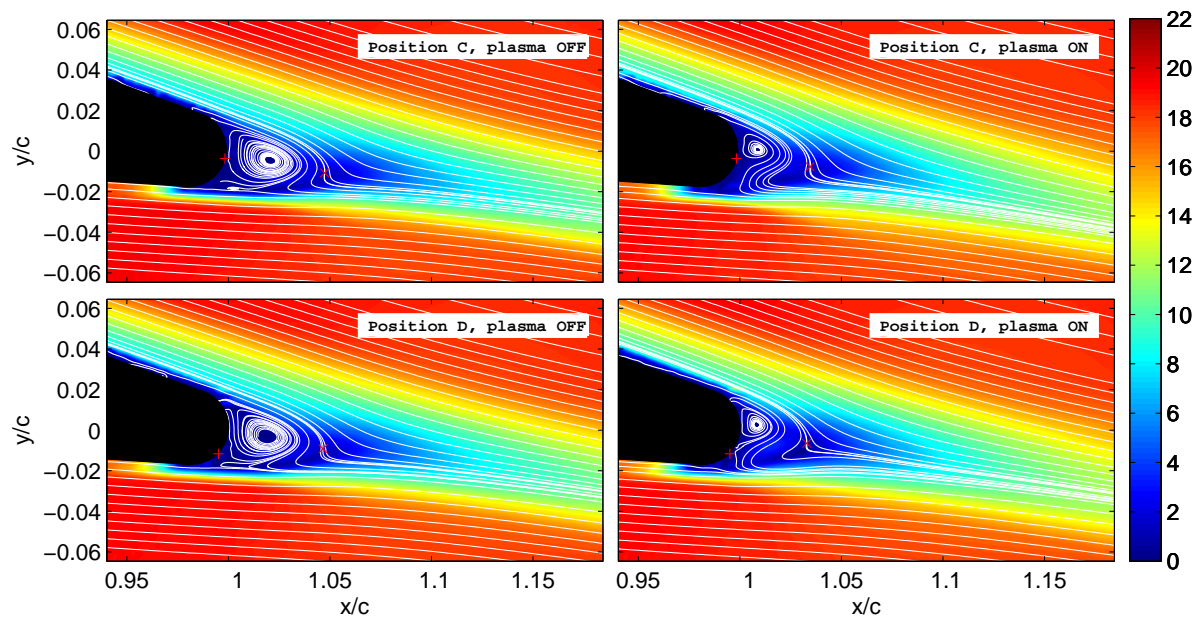


**Figure B.2:** Mean velocity fields produced by plasma actuators C and D (on and off) at an angle of attack of  $7^\circ$  and Reynolds number  $2.19 \cdot 10^5$ . The + indicates the actuator gap position, the x indicates the location of the saddle point. The velocity is in m/s.

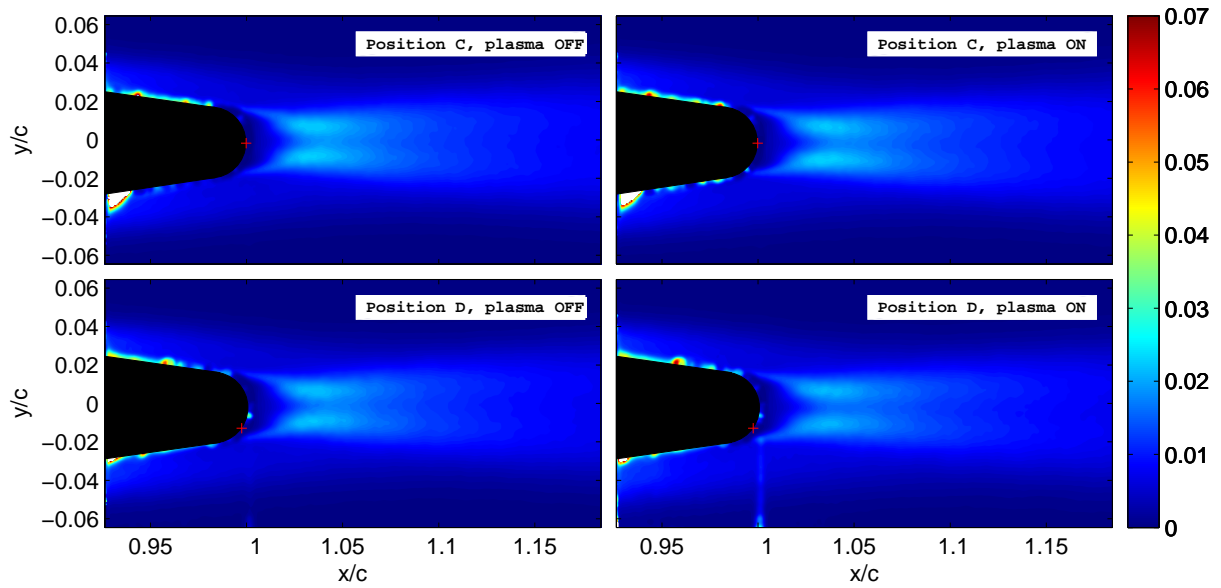


**Figure B.3:** Turbulent kinetic energy fields produced by plasma actuators C and D (on and off) at an angle of attack of  $0^\circ$  and Reynolds number  $2.19 \cdot 10^5$ . The + indicates the actuator gap position. Turbulent kinetic energy in  $0.5(\overline{u'_x u'_x} + \overline{u'_y u'_y})/U_\infty^2$

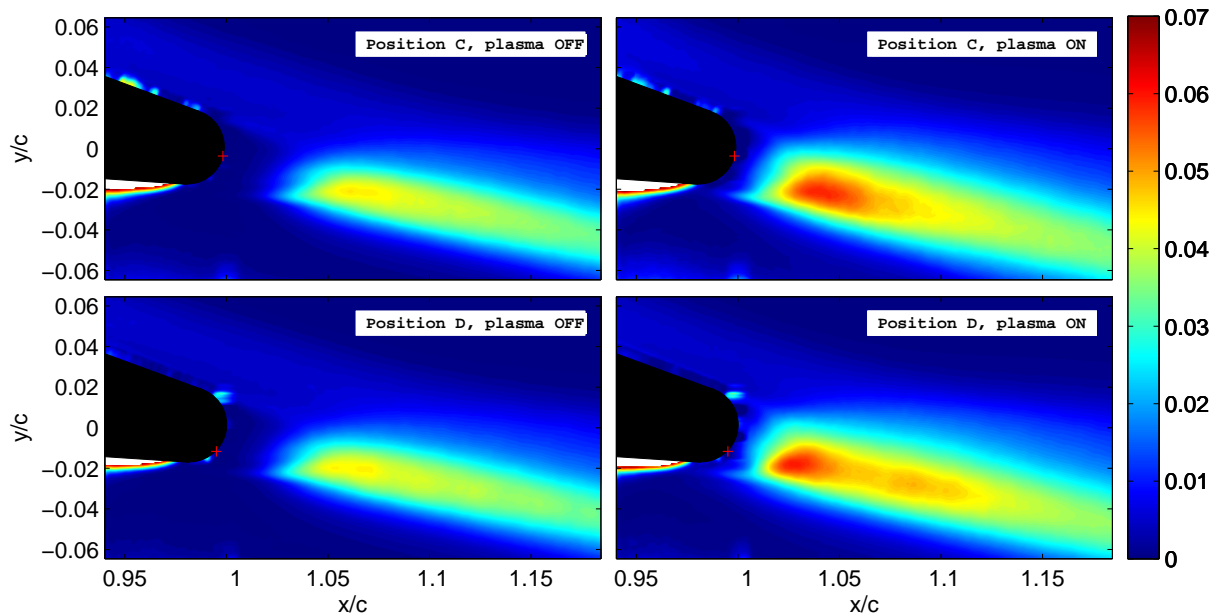


**Figure B.4:** Turbulent kinetic energy fields produced by plasma actuators C and D (on and off) at an angle of attack of  $7^\circ$  and Reynolds number  $2.19 \cdot 10^5$ . The + indicates the actuator gap position. Turbulent kinetic energy in  $0.5(\overline{u'_x u'_x} + \overline{u'_y u'_y})/U_\infty^2$

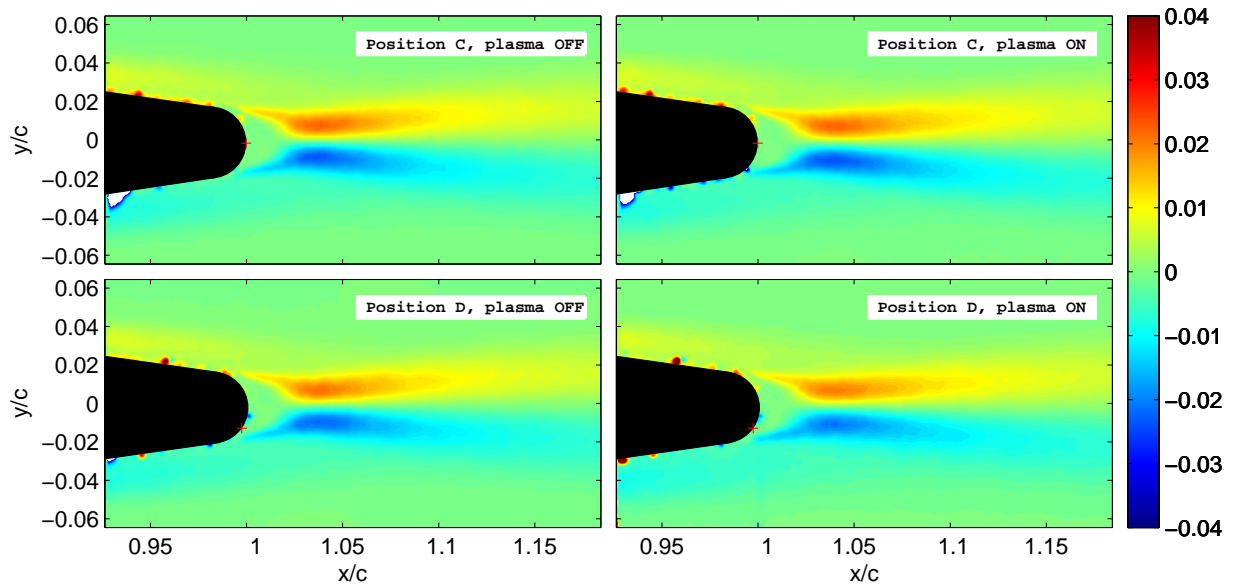


**Figure B.5:** Average Reynolds stress fields produced by plasma actuators C and D (on and off) at an angle of attack of  $0^\circ$  and Reynolds number  $2.19 \cdot 10^5$ . The + indicates the actuator gap position. Average Reynolds shear stress fields in  $\rho \overline{u'_x u'_y} / U_\infty^2$

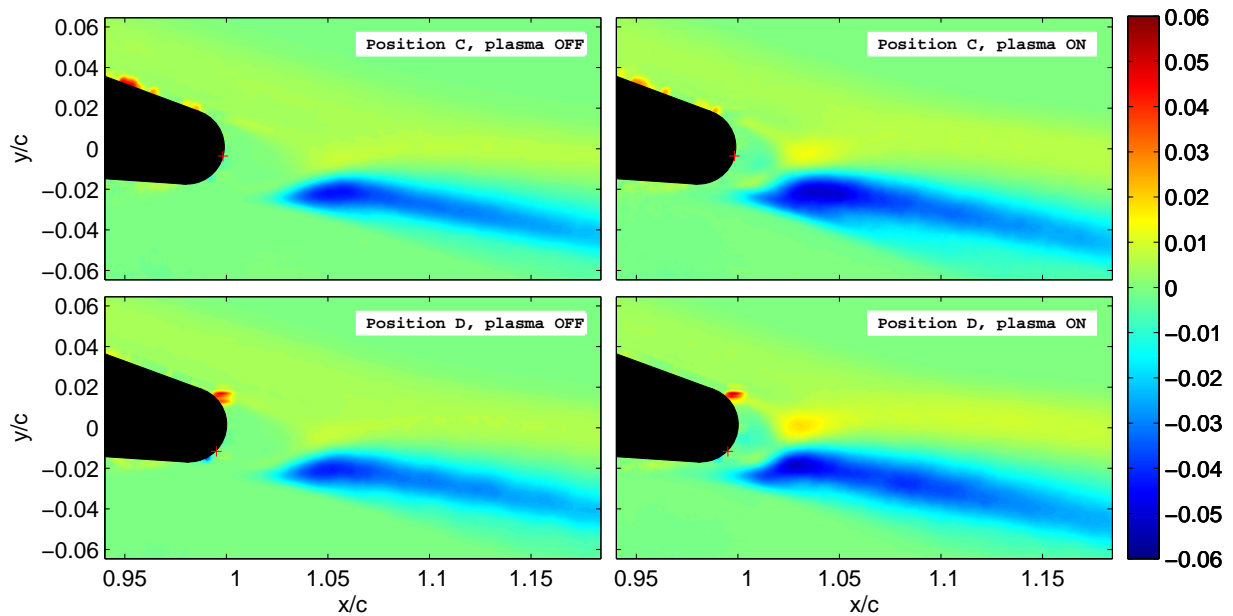


**Figure B.6:** Average Reynolds stress fields produced by plasma actuators C and D (on and off) at an angle of attack of  $7^\circ$  and Reynolds number  $2.19 \cdot 10^5$ . The + indicates the actuator gap position. Average Reynolds shear stress fields in  $\rho \overline{u'_x u'_y} / U_\infty^2$

# Wake details: more results

During the second experimental campaign particle image velocimetry was applied in order to characterize the flow field around the trailing edge. Selected actuator configurations, angles of attack and Reynolds numbers were tested as indicated in table 4.7. By the use of Davis 8.1.3 (Lavisio GmbH) the mean velocity field is calculated. The mean velocity data in the wake is analysed and an attempt is made to characterize the effectiveness of the plasma actuators from the obtained results. This appendix shows the PIV wake data for a Reynolds number of  $2.19 \cdot 10^5$  by plotting some typical wake characteristics that are derived from the mean velocity data in figures B.1 and B.2. The velocity distribution in the wake (wake shape), the streamwise location of the maximum velocity deficit (wake location) and the streamwise distribution of the wake half-width (wake width) are presented in subsequent sections. See section 4.5 for more information on the experimental set-up, selected actuator configurations and parameters used in this experiment. For a more elaborated discussion on the PIV wake data one is referred to section 5.3, where the data for Reynolds number of  $1.46 \cdot 10^5$  is analysed.

## Wake shape

Figures C.1 and C.2 show the streamwise velocity component distribution at four different streamwise stations in the wake at an angle of attack of  $0^\circ$  and  $7^\circ$ , respectively. The selected stations are located at approximately  $x/c=0.03$ ,  $0.08$ ,  $0.13$  and  $0.18$  behind the trailing edge of airfoil.

## Wake location

Figures C.3 and C.4 show the locations of the wake in streamwise direction for all actuator on and off cases and at angles of attack of  $0^\circ$  and  $7^\circ$ , respectively.

## Wake width

Finally, the streamwise distribution of the wake half-width is shown in figures C.5 and C.6 for angles of attack  $0^\circ$  and  $7^\circ$ , respectively.

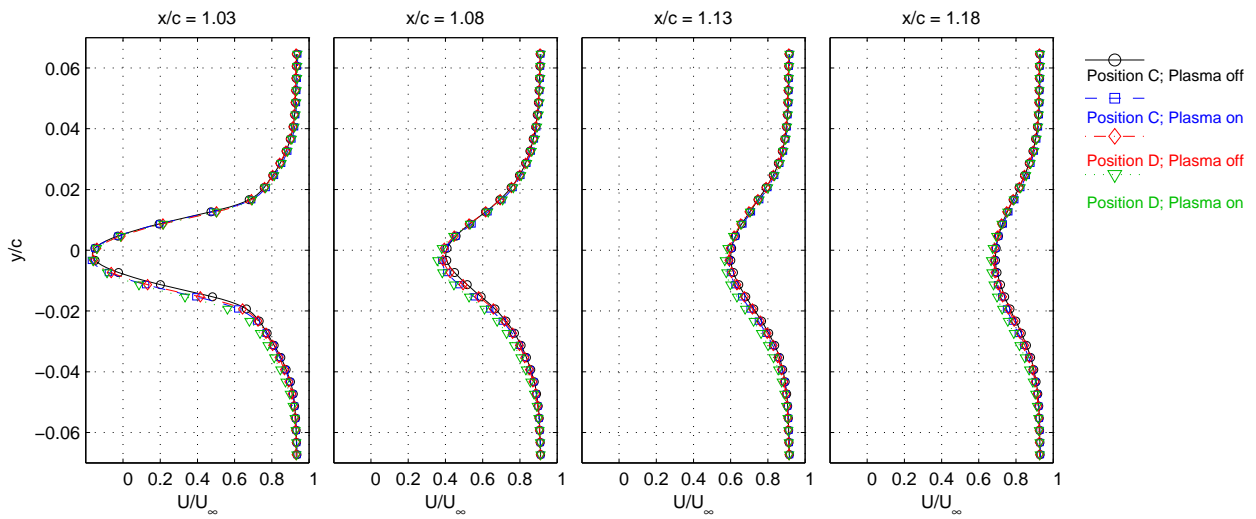


**Figure C.1:** Vertical distribution of the time-averaged streamwise velocity component ( $u_x$ ) produced by plasma actuators C and D (on and off) at an angle of attack of  $0^\circ$  and Reynolds number  $2.19 \cdot 10^5$

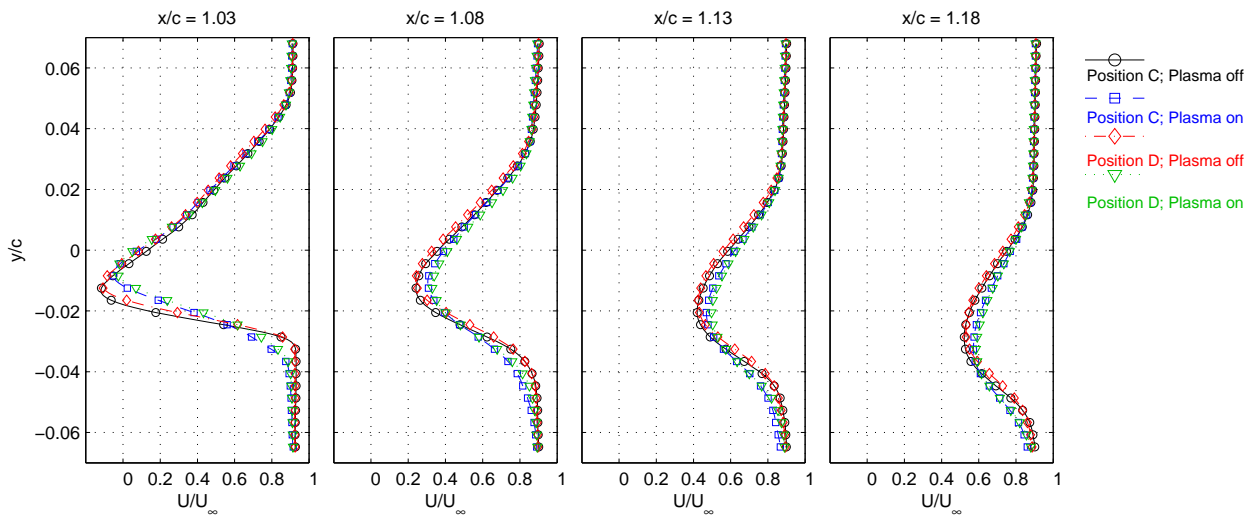


**Figure C.2:** Vertical distribution of the time-averaged streamwise velocity component ( $u_x$ ) produced by plasma actuators C and D (on and off) at an angle of attack of  $7^\circ$  and Reynolds number  $2.19 \cdot 10^5$

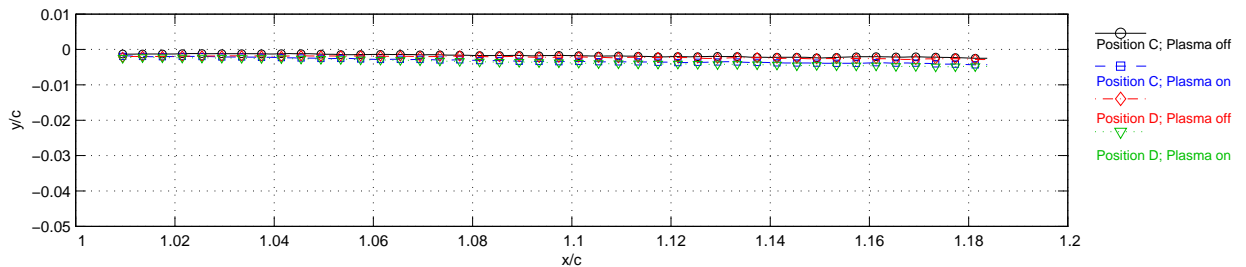


**Figure C.3:** Location of the maximum streamwise velocity deficit in the wake as produced by plasma actuators C and D (on and off) at an angle of attack of  $0^\circ$  and Reynolds number  $2.19 \cdot 10^5$

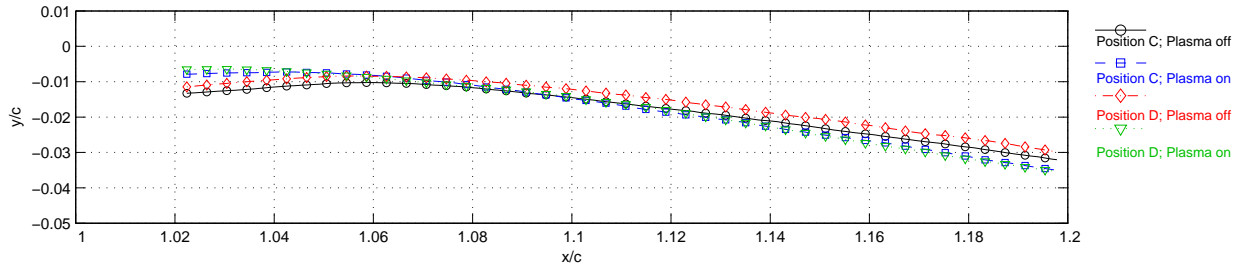


**Figure C.4:** Location of the maximum streamwise velocity deficit in the wake as produced by plasma actuators C and D (on and off) at an angle of attack of  $7^\circ$  and Reynolds number  $2.19 \cdot 10^5$

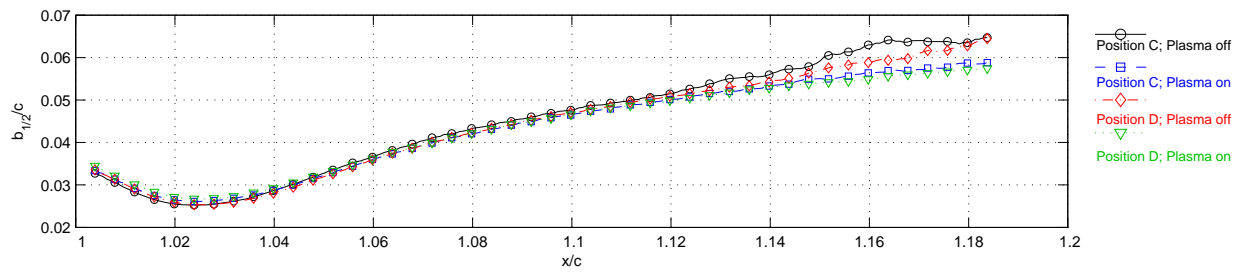


**Figure C.5:** Streamwise distribution of the wake half-width as produced by plasma actuators C and D (on and off) at an angle of attack of  $0^\circ$  and Reynolds number  $2.19 \cdot 10^5$

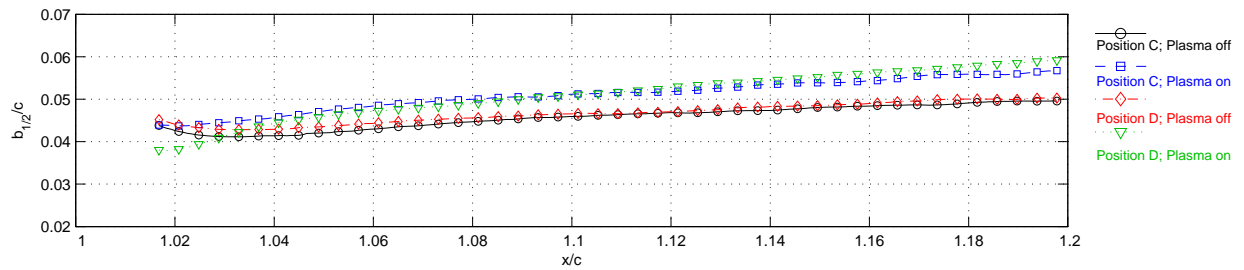


**Figure C.6:** Streamwise distribution of the wake half-width as produced by plasma actuators C and D (on and off) at an angle of attack of  $7^\circ$  and Reynolds number  $2.19 \cdot 10^5$

